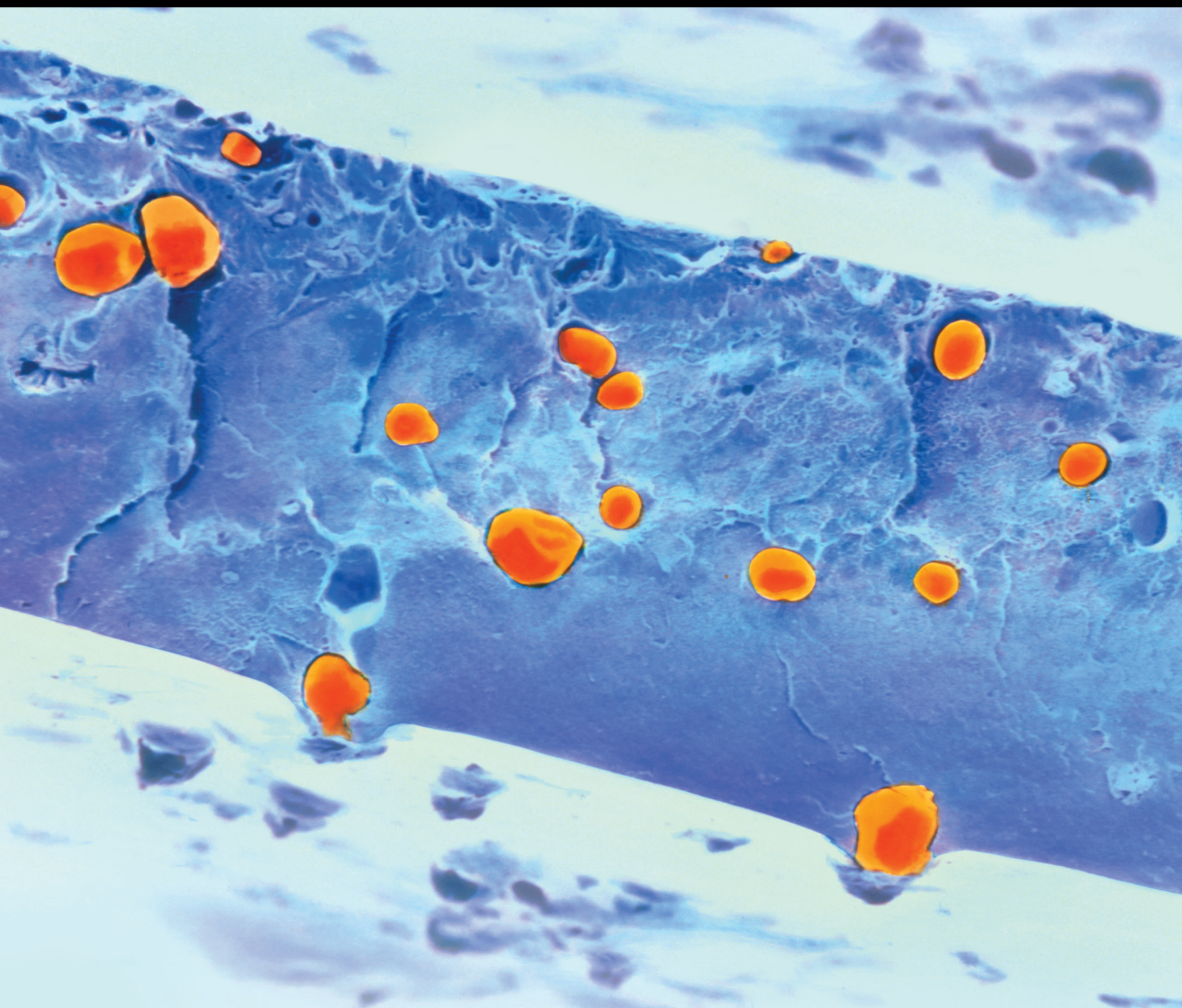


International Journal of Polymer Science

# Hierarchical Structured Polymeric Materials in Nanotechnology

Guest Editors: Xiao Gong, Tairong Kuang, Yiwen Li, Xiaohong Hu,  
and Ming Zhang





---

# **Hierarchical Structured Polymeric Materials in Nanotechnology**

International Journal of Polymer Science

---

## **Hierarchical Structured Polymeric Materials in Nanotechnology**

Guest Editors: Xiao Gong, Tairong Kuang, Yiwen Li,  
Xiaohong Hu, and Ming Zhang



---

Copyright © 2016 Hindawi Publishing Corporation. All rights reserved.

This is a special issue published in "International Journal of Polymer Science." All articles are open access articles distributed under the Creative Commons Attribution License, which permits unrestricted use, distribution, and reproduction in any medium, provided the original work is properly cited.

## Editorial Board

Domenico Acierno, Italy  
Sharif Ahmad, India  
Mats R. Andersson, Australia  
Luc Averous, France  
M. Barletta, Italy  
Christopher Batich, USA  
Giuseppe Battaglia, UK  
Marc Behl, Germany  
Laurent Billon, France  
David G. Bucknall, USA  
Andrea Camposeo, Italy  
Wen Shyang Chow, Malaysia  
J. deClaville Christiansen, Denmark  
Yoshiki Chujo, Japan  
Angel Concheiro, Spain  
Marek Cypryk, Poland  
Li Ming Dai, USA  
Yulin Deng, USA  
Maria Laura Di Lorenzo, Italy  
Eliane Espuche, France  
Antonio Facchetti, USA  
M. Fernández-García, Spain  
Benny Dean Freeman, USA  
Jean-François Gérard, France  
Peng He, USA  
Jan-Chan Huang, USA  
Wei Huang, China  
Nabil Ibrahim, Egypt  
Tadashi Inoue, Japan  
Avraam I. Isayev, USA  
Koji Ishizu, Japan  
Patric Jannasch, Sweden  
Nobuhiro Kawatsuki, Japan  
J.M. Kenny, Italy  
Mubarak A. Khan, Bangladesh  
Ruhul A. Khan, Canada  
Saad Khan, USA  
Jui-Yang Lai, Taiwan  
Jose Ramon Leiza, Spain  
Guiping Ma, China  
Evangelos Manias, USA  
Ulrich Maschke, France  
Jani Matisons, Australia  
Geoffrey R. Mitchell, UK  
Subrata Mondal, India  
Christian Nielsen, UK  
Toribio F. Otero, Spain  
Qinmin Pan, Canada  
Alessandro Pegoretti, Italy  
Önder Pekcan, Turkey  
Zhonghua Peng, USA  
Antje Potthast, Austria  
Debora Puglia, Italy  
Miriam Rafailovich, USA  
Arthur J. Ragauskas, USA  
Subramaniam Ramesh, Malaysia  
Bernabé L. Rivas, Chile  
J. Rodriguez-Hernandez, Spain  
H. Roghani-Mamaqani, Iran  
Pietro Russo, Italy  
Mehdi Salami-Kalajahi, Iran  
Erol Sancaktar, USA  
A. P. Schenning, Netherlands  
M. Schnabelrauch, Germany  
Shu Seki, Japan  
Vitor Sencadas, Australia  
Robert A. Shanks, Australia  
Mikhail Shtilman, Russia  
B. Siddaramaiah, India  
D. W. Smith Jr., USA  
Atsushi Sudo, Japan  
Kohji Tashiro, Japan  
Hideto Tsuji, Japan  
Masaki Tsuji, Japan  
Stefano Turri, Italy  
Hiroshi Uyama, Japan  
Cornelia Vasile, Romania  
Alenka Vesel, Slovenia  
Yakov S. Vygodskii, Russia  
De-Yi Wang, Spain  
Qinglin Wu, USA  
Frederik Wurm, Germany  
Huining Xiao, Canada  
Yiqi Yang, USA  
Long Yu, Australia  
Philippe Zinck, France

# Contents

---

**Hierarchical Structured Polymeric Materials in Nanotechnology**

Xiao Gong, Tairong Kuang, Yiwen Li, Xiaohong Hu, and Ming Zhang

Volume 2016, Article ID 8457069, 2 pages

**A Photochromic Copolymer Hydrogel Contact Lens: From Synthesis to Application**

Xiaoli Yang, Limin Huang, Lihua Zhou, Hao Xu, and Zihan Yi

Volume 2016, Article ID 4374060, 8 pages

**Poly(lactic Acid) Based Nanocomposites: Promising Safe and Biodegradable Materials in Biomedical Field**

Lili Sha, Zhaofeng Chen, Zhou Chen, Aili Zhang, and Zhaogang Yang

Volume 2016, Article ID 6869154, 11 pages

**Effects of Organomontmorillonite Content on Morphology and Mechanical and Thermal Properties of Poly(2,6-dimethyl-1,4-phenylene oxide)/Polyamide-66 Nanocomposites**

Kunxiao Yang, Chunling Xin, Ying Huang, Lilong Jiang, and Yadong He

Volume 2016, Article ID 9104395, 9 pages

**Phospholipid Adsorption Polymeric Materials for Detection of Xylazine and Metabolite in Blood and Urine**

Xue Gao, Hao Guo, and Chaokang Gu

Volume 2016, Article ID 3682167, 8 pages

**Nanodeserts: A Conjecture in Nanotechnology to Enhance Quasi-Photosynthetic CO<sub>2</sub> Absorption**

Wenfeng Wang, Xi Chen, Yifan Zhang, Jianjun Yu, Tianyi Ma, Zhihan Lv, Jing Zhang, Fanyu Zeng, and Hui Zou

Volume 2016, Article ID 5027879, 10 pages

**Attapulgit Nanofiber-Cellulose Nanocomposite with Core-Shell Structure for Dye Adsorption**

Xiaoyu Chen, Xiaoxue Song, and Yihe Sun

Volume 2016, Article ID 2081734, 9 pages

## Editorial

# Hierarchical Structured Polymeric Materials in Nanotechnology

**Xiao Gong,<sup>1</sup> Tairong Kuang,<sup>2</sup> Yiwen Li,<sup>3</sup> Xiaohong Hu,<sup>4</sup> and Ming Zhang<sup>5</sup>**

<sup>1</sup>State Key Laboratory of Silicate Materials for Architectures, Wuhan University of Technology, Wuhan 430070, China

<sup>2</sup>Ohio State University, Columbus, OH, USA

<sup>3</sup>Sichuan University, Chengdu, China

<sup>4</sup>Jinling Institute of Technology, Nanjing, China

<sup>5</sup>University of Akron, Akron, OH, USA

Correspondence should be addressed to Xiao Gong; [gongxiaopattern@gmail.com](mailto:gongxiaopattern@gmail.com)

Received 11 October 2016; Accepted 12 October 2016

Copyright © 2016 Xiao Gong et al. This is an open access article distributed under the Creative Commons Attribution License, which permits unrestricted use, distribution, and reproduction in any medium, provided the original work is properly cited.

Contemporarily, increasing functional soft materials possessing desirable hierarchical structures and engineered properties have been applied to energy and health care related field under the promotion of nanotechnology development. Providing or creating ideal advanced materials in these burgeoning fields is associated with conceivable structure and chemical composition design including nanocomposite design, multifunctional monomer synthesis and addition, surface engineering strategies, and structure and property analysis. This special issue focuses on the recent advance in polymeric soft matters with different hierarchical structures, including hydrogels, films, and their applications. Although the issue could not include all progress in the related fields, it strives to provide comprehensive and timely information for polymers-based nanotechnology with diverse applications. We hope this issue will not only present new original researches contributed by experienced scientists, but also offer the general reviews to highlight the development of this research field.

Firstly, the hierarchical structured polymeric materials in health care related field as a form of nanoparticle, film, or solution were prepared by new synthetic strategies and surface design concepts and discussed in this special issue. Z. He et al. effectively labeled K237/FA-PEG-PLGA nanoparticles with Technetium-99m (<sup>99m</sup>Tc), evaluated its optimal stability in different aqueous environment, investigated performance including affinity and biodistribution through in vitro cell experiment or in vivo animal experiment, and demonstrated from their result that K237/FA-PEG-PLGA nanoparticles

have great potential as biodegradable drug carriers. H. Gao et al. reported an efficient and effective method to use phospholipid adsorption polymeric materials to determine xylazine in blood and urine samples, which could be applied by academic groups and commercial organizations. X. Yang et al. designed and synthesized photochromic hydrogel contact lens for drug delivery and investigated its properties and performance. Beside these original researches, L. Sha et al. highlighted recent researches of PLA based nanocomposites and their application in biomedical fields including bone substitute and repair, tissue engineering, and drug delivery system.

Secondly, nanocomposite materials were designed to endow materials of the special structure and functionality. For example, W. Wang et al. developed hierarchical structured polymeric nanomaterials (nanodeserts) for enhancing abiotic CO<sub>2</sub> fixation in the soil-groundwater system beneath deserts. K. Yang et al. prepared nanocomposites consisting of polymer matrix (PPO-g-MA or PPO/PA66) and nanofiller (organomontmorillonite) and investigated the properties including morphology, the mechanical properties, and thermal stability. X. Chen et al. prepared nanocomposite particle with cellulose core and attapulgite nanofibers shell, characterized core size and thickness of nanofibers shell, and investigated the absorbance behavior and mechanism.

In summary, we would like to thank all of the authors, reviewers, and the journal editorial staff members for their kind contributions to this special issue. We sincerely hope you enjoy reading those original research work and interesting

review papers, get inspirations, and find it beneficial to your future research and teaching activities.

*Xiao Gong*  
*Tairong Kuang*  
*Yiwen Li*  
*Xiaohong Hu*  
*Ming Zhang*

## Research Article

# A Photochromic Copolymer Hydrogel Contact Lens: From Synthesis to Application

**Xiaoli Yang, Limin Huang, Lihua Zhou, Hao Xu, and Zihan Yi**

*School of Material Engineering, Jinling Institute of Technology, Nanjing 211169, China*

Correspondence should be addressed to Xiaoli Yang; yangxl@jit.edu.cn

Received 27 June 2016; Revised 8 September 2016; Accepted 22 September 2016

Academic Editor: Xiao Gong

Copyright © 2016 Xiaoli Yang et al. This is an open access article distributed under the Creative Commons Attribution License, which permits unrestricted use, distribution, and reproduction in any medium, provided the original work is properly cited.

A photochromic poly(2-hydroxyl-ethyl methacrylate-*N*-vinylpyrrolidone-spiro-naphthoxazine) hydrogel (p(HEMA-NVP-SPO)) has been designed and synthesized by free radical polymerization in this work. The chemical and structural information of hydrogels was investigated by IR spectra, equilibrium water content (EWC), and SEM. The IR spectra confirmed successful synthesis of copolymer. The domain of NVP contributed to not only EWC but also inner structure of hydrogel, while SPO had little influence on these properties of hydrogel. The photochromic behaviors of hydrogel including photochromic properties and thermal fading kinetics were systematically studied and compared with hydrogel made by immersing method. Results showed that when SPO was incorporated in hydrogel by polymerization, maximum absorbance wavelength got shorter, and the relaxation half-life became longer. In addition, salicylic acid as a drug model could be loaded into hydrogel by immersing method, and its sustained drug release in a given period was dependent on the characteristics of solution and loading time.

## 1. Introduction

Photochromic materials can change their color after being triggered by certain light due to a reversible structural transformation of chemical [1–3]. Spiro-naphthoxazine (SPO) based materials have attracted increasing interest due to their remarkable photochromic properties, such as excellent photostability, compatibility in various matrices, and high fatigue resistance [4–7]. These advantages enhance the practical applicability of SPO in optical systems for registration and storage [8], molecular switches [9], and UV sensors [10]. The photoresponsive site of the SPO comes from the center  $sp^3$  spiro carbon. Upon UV irradiation, the carbon-oxygen bond cleaves and achieves  $sp^2$  hybridization, yielding an open planar merocyanine (MC), which is metastable and readily isomerizes [11, 12]. So it can revert back to the spiro form via ring closing when irradiated with visible light or thermal radiation. We have previously synthesized a series of SPO derivatives and investigated their photochromic behaviors and thermal stability in different films [13]. All the compounds exhibited excellent photochromic properties upon UV irradiation. And their relaxation time was in a

broad range (from 129 to 1724 s). On account of these merits, SPO was introduced into hydrogel contact lens in this work, aiming at endow contact lens with photochromic properties.

As far as contact lens was concerned, hydrogel is a leading material of contact lens due to its good transparency, which satisfied the optic requirement of contact lens [14]. Moreover, hydrogel had a water swollen structure, which can mimetic nature biological environment. Thus, generally, hydrogel possesses good biocompatibility [15, 16]. Traditional hydrogel contact lens is polymerized by 2-hydroxyl-ethyl methacrylate (HEMA), but a number of problems restricted its application like low oxygen permeability, limited hydrophilicity, and poor antibacterial properties. Recently, some measures had been taken to improve these problems including copolymerizing with hydrophilic monomer [17], introducing chitosan to hydrogel network [18], and modifying surface via layer-by-layer assembly [19–21]. Further, in order to realize certain functions like drug delivery function, other functional monomers such as cyclodextrin (CD) had been introduced into contact lens by copolymerization [22, 23], by surface functionalization [24], or by nanocomposite technology [25]. Although the

abovementioned researches had made considerable progress, they did not refer to photochromic contact lens.

In this work, we attempted to introduce SPO into hydrogel contact lens by polymerization, investigate their properties, and explore their application. In order to improve the hydrophilicity, vinylpyrrolidone (NVP) has also been added. As a control, SPO blended hydrogel contact lens was also prepared.

## 2. Experimental

**2.1. Materials.** Hydroxyethyl methacrylate (HEMA) and N-vinylpyrrolidone (NVP) were obtained from Shanghai Jingchun Industries Co. Ltd., China, and distilled under vacuum before use. 2,2-Azobis(isobutyronitrile) (AIBN) was recrystallized from methanol. All other chemicals were analytically pure and were employed without any further drying or purification.

Phosphate buffered saline (PBS) (pH 7.2) solution is as follows: 137 mmol L<sup>-1</sup> NaCl, 2.7 mmol L<sup>-1</sup> KCl, 10 mmol L<sup>-1</sup> Na<sub>2</sub>HPO<sub>4</sub>, and 2 mmol L<sup>-1</sup> KH<sub>2</sub>PO<sub>4</sub>. Artificial tear solution (ATS) is as follows: 2.18 g L<sup>-1</sup> NaHCO<sub>3</sub>, 6.78 g L<sup>-1</sup> NaCl, 0.084 g L<sup>-1</sup> CaCl<sub>2</sub>, and 1.38 g L<sup>-1</sup> KCl.

**2.2. Synthesis of Spironaphthoxazine (SPO) Monomer.** The synthetic methods for the photochromic SPO monomer of 1,3,3-trimethyl-9'-methacryloyloxy-spiro[indoline-2,3'(3H)naphtho[2,1-b][1,4]oxazine] were adopted and modified from previously published procedure [26]. Grey solid, yield: 97.4%, m.p. 151–153°C (melting point apparatus, Taike, China). IR (IS10, KBr, cm<sup>-1</sup>): 3048, 2972, 1730, 1628, 1480, 1440, 1360, 1257, 1080, 1170, 1118, 978, 902, 823, 745. <sup>1</sup>H NMR (CDCl<sub>3</sub>, AV-500): δ 8.26 (1H, d, J = 2.3 Hz, ArH), 7.77 (1H, d, J = 8.9 Hz, ArH), 7.73 (1H, s, 2'-H), 7.66 (1H, d, J = 8.9 Hz, ArH), 7.24–7.17 (2H, m, ArH), 7.08 (1H, d, J = 7.1 Hz, ArH), 6.98 (1H, d, J = 8.9 Hz, ArH), 6.90 (1H, t, J = 7.4 Hz, ArH), 6.56 (1H, d, J = 7.7 Hz, ArH), 6.39 (1H, s, CH), 5.77 (1H, s, CH), 2.74 (3H, s, CH<sub>3</sub>), 2.10 (3H, s, CH<sub>3</sub>), 1.36 (6H, s, CH<sub>3</sub>). Anal. calcd. for C<sub>26</sub>H<sub>24</sub>N<sub>2</sub>O<sub>3</sub>: C, 75.71; H, 5.86; N, 6.79. Found C, 75.58; H, 5.84; N, 6.80%.

### 2.3. Synthesis of Photochromic Hydrogels

**Polymerization Method.** Monomers (5 mL) of HEMA, NVP, and SPO were mixed by stirring, in which certain amount of AIBN was added into the mixture. This mixture was injected into the model (150 μm thickness), which then was put into the oven for 3 hours at 70°C; the reaction mixture was brought to room temperature, filtered, and rinsed with ethanol five times to remove all chemicals and nonconjugated monomer. The product was dried in vacuum. In addition, the feed composition and the samples code of the hydrogels are listed in Table 1.

**Immersing Method.** The p(HEMA-NVP) hydrogels were obtained by using the polymerization method above and then were immersed in ethanol solution (5 mL), in which the concentration of SPO was 3%. The samples were kept

TABLE 1: Composition of initial reaction mixtures used for the preparation of polymer hydrogels.

Hydrogels	Mass ratio (%)
	HEMA : NVP : SPO
Hydrogel 1	100 : 0 : 0
Hydrogel 2	75 : 25 : 0
Hydrogel 3	60 : 40 : 0
Hydrogel 4	60 : 40 : 3

undisturbed at room temperature for a week; the resulting films were kept in dark before measurement.

**2.4. Characterization of Photochromic Hydrogels.** The formed hydrogels were characterized by IR spectrum (IS10). Each hydrogel was freeze-dried at -50°C and then characterized by scanning electron microscopy (SEM, SU8010).

The hydrogels were dried and weighed ( $W_0$ ). The hydrogels were weighed ( $W_1$ ) after dry hydrogels had been submerged in distilled water at 37°C for 24 h. Equilibrium water content of the hydrogels was defined as EWC (%) =  $(W_1 - W_0)/W_1 \times 100\%$ .

Optical absorption spectra were recorded using UV spectrum (CARY 50). The sample was first irradiated with a 40 W ultraviolet lamp (365 nm) and then reverse irradiated with visible light. The process was repeated for 20 cycles. The intervals were 10 min.

The kinetics of the thermal discoloration were recorded following the color bleaching of the irradiated sample at  $\lambda_{\max}$ , immediately after switching off the ultraviolet lamp. The discoloration dynamic at  $\lambda_{\max}$  was fitted by the following equation [27]:

$$\ln\left(\frac{A_t - A_\infty}{A_0 - A_\infty}\right) = -k \cdot t, \quad (1)$$

where  $A_0$ ,  $A_t$ , and  $A_\infty$  are the absorbencies at zero, times, and infinity respectively.

For salicylic acid release experiment, an amount of 5 mg of salicylic acid model drug was dissolved in 100 mL water or buffered solution (PBS, ATS); then, 20 mg hydrogels were submerged into the solution to load drug. After 24 h at 37°C, the absorbance of salicylic acid was measured by UV-Vis spectrophotometer (Varian, Vary 50) at  $\lambda_{\max} = 279$  nm and compared with a standard curve. The salicylic acid concentration after loading was obtained by the difference of concentration and volume before and after immersing. The cumulative release rate in hydrogel was calculated by the difference of salicylic acid concentration before and after loading.

## 3. Results and Discussion

**3.1. Synthesis and Fundamental Characterization of Hydrogels.** The FTIR spectra of hydrogels were shown in Figure 1. In case of PHEMA (hydrogel 1), a broad band that appeared at 3440 cm<sup>-1</sup> was attributed to hydrogen-bonded OH group. The strong peak at 1720 cm<sup>-1</sup> showed ester carbonyl group

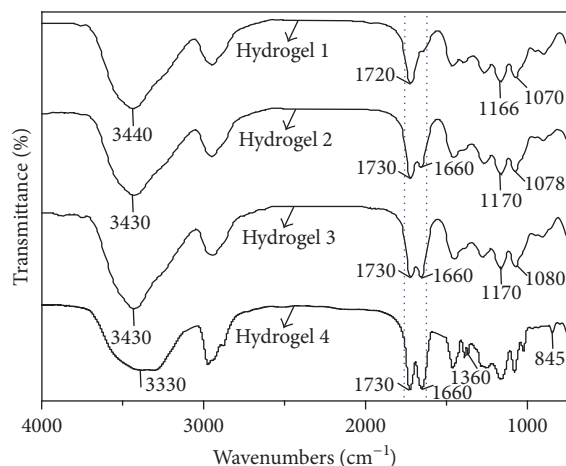


FIGURE 1: The IR spectra of hydrogels.

(C=O). The peaks at 1166 and 1070  $\text{cm}^{-1}$  were associated with the stretching vibrations of C-O [28]. Compared to the IR spectrum of pHEMA, p(HEMA-NVP) (hydrogel 2 and hydrogel 3) showed a new peak at around 1665  $\text{cm}^{-1}$ , corresponding to the carbonyl stretching banding of NVP [29]. With increasing NVP content, this characteristic absorption band was strengthened, which further confirmed the presence of NVP in the hydrogels. In the spectrum of p(HEMA-NVP-SPO) (hydrogel 4), the new absorption bands at 1360  $\text{cm}^{-1}$  and 845  $\text{cm}^{-1}$  were attributed to the stretching vibration of Ar-N and the stretching vibration outside surface of =C-H in SPO, respectively. Furthermore, characteristic bands at around 900  $\text{cm}^{-1}$  and 3100  $\text{cm}^{-1}$  corresponding to the vinyl groups of monomers disappeared completely, which indicated nonexistence of unreacted monomers. These well supported the successful entry of SPO moieties into the network formation of hydrogels [30].

The equilibrium water content (EWC) of the hydrogels was also studied (Figure 2). As it can be seen, all hydrogels exhibited EWC values greater than 30% in distilled water, which belong to the soft contact lens materials. In the case of the p(HEMA-NVP) hydrogels (hydrogel 2 and hydrogel 3), EWC values were observed to increase from about 47% to 61% with the increase of the NVP content. In contrast, the pure pHEMA hydrogel (hydrogel 1) showed a minimum EWC value about 34%. NVP was more hydrophilic than HEMA; hence, when increasing NVP content, the hydrogel networks became more hydrophilic and then absorbed more water. Moreover, the adding of a small amount of SPO had nearly no influence upon EWC of hydrogels. It is noted that the hydrogels showed a lower EWC in the presence of PBS than in distilled water. This might be attributed to the change of osmotic pressure [31]. Compared with water, the higher salt concentration in PBS decreased the osmotic pressure difference between hydrogel network and external solution, which prevented water molecules from penetrating into the hydrogels.

The interior morphologies of the freeze-dried hydrogels were shown in Figure 3. The pure pHEMA hydrogel

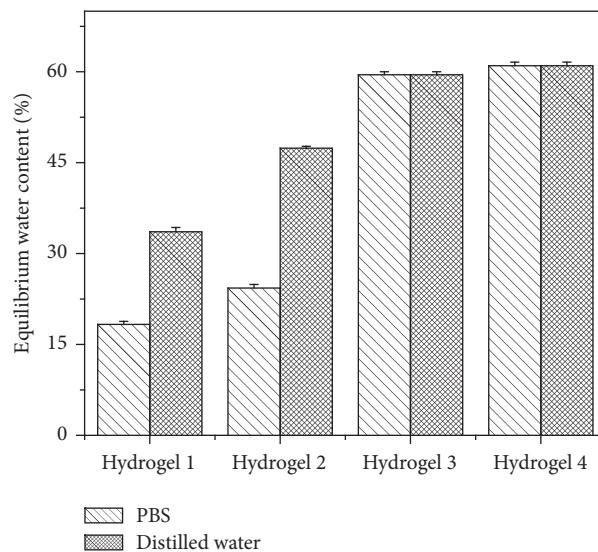


FIGURE 2: The equilibrium water content of hydrogels.

presented a continuous and even morphology without pores (hydrogel 1). In contrast, the pHEMA-NVP hydrogel exhibited a highly interconnected porous structure (hydrogel 2 and hydrogel 3). It was observed that hydrogel 3 had larger average pore size ( $24 \pm 10 \mu\text{m}$ ) than hydrogel 2 ( $16 \pm 3 \mu\text{m}$ ) due to the increasing of NVP content. This trend might be related to relative larger free volume of NVP owing to the existence of five-membered ring, which prevented the collapse of linear chain in the freeze-drying process, resulting in larger pore size. p(HEMA-NVP-SPO) hydrogel (hydrogel 4) was similar to that of hydrogel 3, indicating little influence of SPO on the morphology. This might be attributed to very small content of SPO in hydrogel.

### 3.2. Photochromic Performance and Thermal Fading Kinetics.

Electronic absorption spectral changes of two hydrogels made by immersing method and by polymerization method are depicted in Figure 4, insets of which show the color changes of photochromic hydrogel before and after UV light; nearly colorless hydrogels turned to blue after being irradiated with UV light and then converted back to that of the initial color under visible light irradiation. The absorption spectrums were broad in both hydrogels; this was mainly related to the coloring mechanism. After UV illumination, bond breakage in the excited spiro form on SPO occurred; the intermediate X was produced first, which then decayed into zwitterionic merocyanines, because the merocyanines were mixture of at least four isomers and their optical spectrums were broad absorption bands [32]. We observed that UV irradiation of the hydrogel made by immersing method at 365 nm led to the maximum absorbance ( $\lambda_{\text{max}}$ ) at 620 nm (Figure 4(a)), while in the hydrogel made by polymerization method there was a shift in  $\lambda_{\text{max}}$  to a shorter wavelength, which was 610 nm (Figure 4(b)). This blue shift presumably indicated that the interaction modes of SPO and HEME-NVP affected the UV absorption of hydrogel. When SPO took part in polymerization reaction, main chain of copolymer

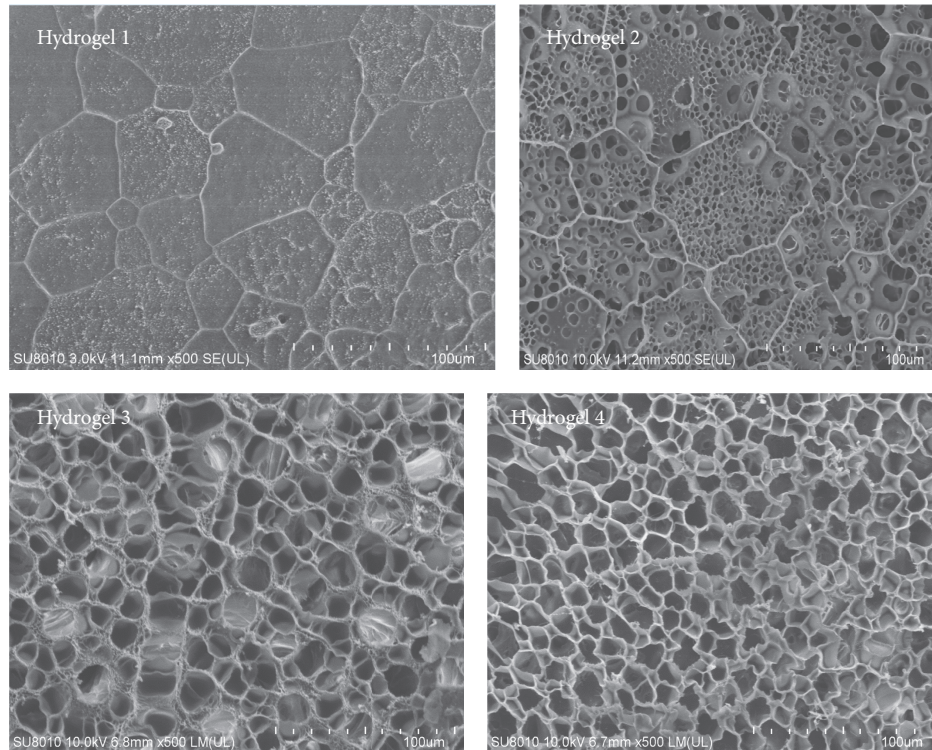


FIGURE 3: SEM images of hydrogels.

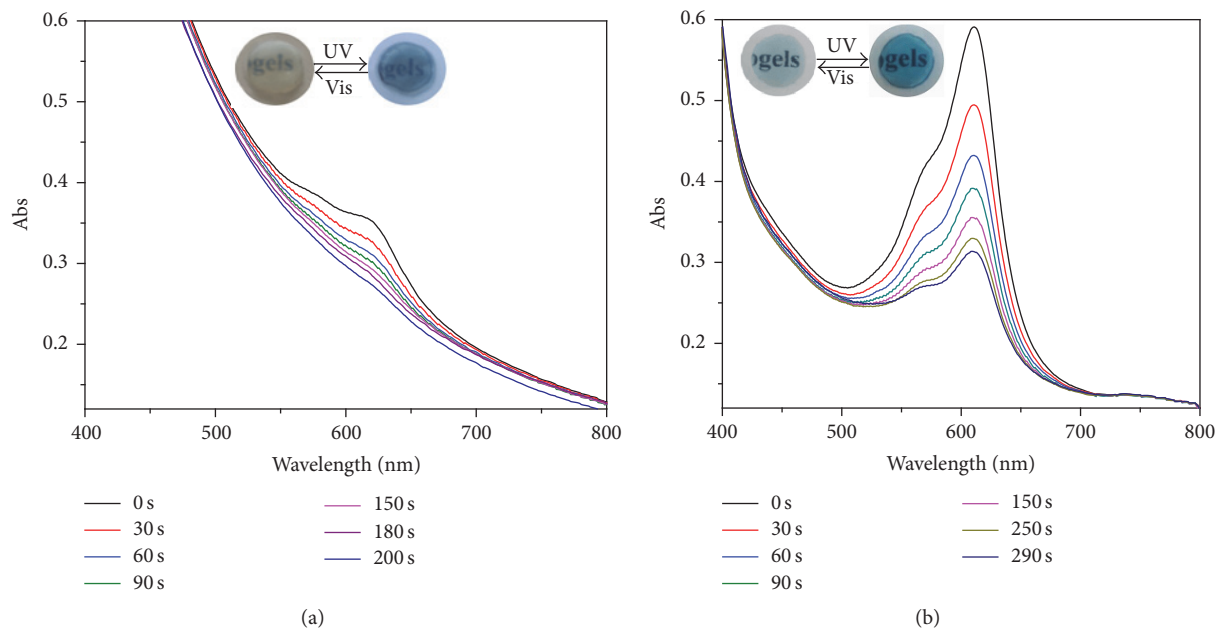


FIGURE 4: Absorption spectra with irradiation time for (a) immersing method and (b) polymerization method.

became the modified group of 9'-C on SPO, increasing the steric hindrance around it, which led to the blue shift of the absorption [33].

Figure 5 shows the thermal fading of photochromic hydrogels in which the MC absorbance at  $\lambda_{\max}$  (620 nm, immersing method; 610 nm, polymerization method) was

recorded immediately after termination of the UV irradiation. The overall thermal closing in both hydrogels was evaluated to obey the first-order kinetics as the plots of  $\ln(A_t - A_\infty)/(A_0 - A_\infty)$  were linear. The corresponding relaxation time of the MC isomer ( $\tau_{\text{MC-SPO}}$ ) was obtained  $t$  using the expression  $\tau = 1/k$ . The relaxation life of hydrogel

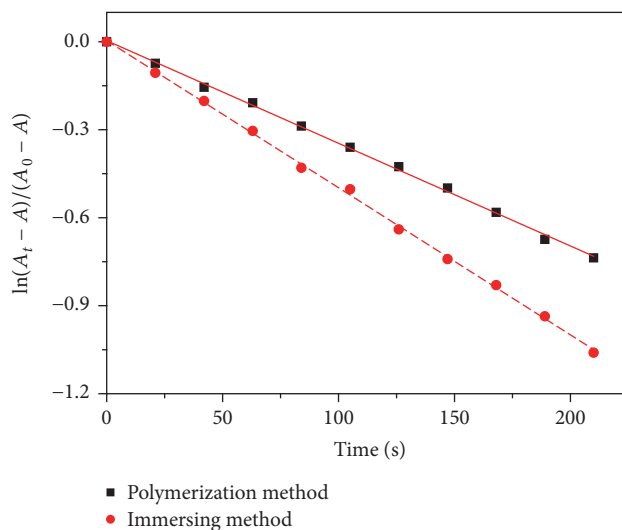


FIGURE 5: The thermal relaxation of the MC at  $\lambda_{\max}$  (620 nm, immersing method; 610 nm, polymerization method) after irradiation with a 40 W UV lamp.

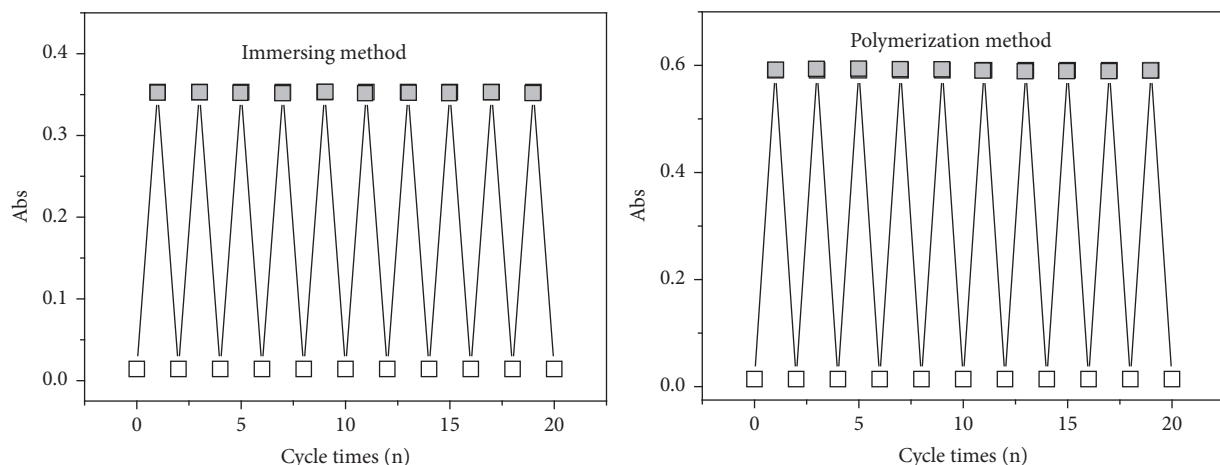


FIGURE 6: Fatigue resistance cycles of photochromic hydrogel by alternative irradiation: gray box at  $\lambda = 365$  nm, and white box  $\lambda = 632$  nm.

made by polymerization method was 289 s which was longer than that made by immersing method (199 s); this could be assigned to the participation of SPO in polymerization reaction. As had been reported by earlier work [34], in solid resins, the bulky substituent in the vicinity of the spirooxazine moiety was benefit to the thermal fading stability of MC. For SPO in hydrogel made by polymerization method, the volume of substituent group on 9'-C is bigger than that made by immersing method, which depressed the large conformational change more effectively in the photochromic reaction. As a result, the thermal fading of hydrogel made by polymerization method was slower than that made by immersing method.

In further step, in order to evaluate the long-term application of photochromic properties for hydrogel, the photoinduced fatigue resistance property might be investigated by multiple irradiation cycles with UV and visible light in Figure 6. The maximum absorbances of the two

photochromic hydrogels were plotted while being irradiated alternately with 365 nm light and 632 nm light. In each cycle, two photochromic hydrogels were converted to their ring-closed forms, respectively, to reach the photostationary states by irradiation with UV light (365 nm), and all the closed-ring forms were bleached by irradiation with visible light (632 nm). It showed that the absorbance of both hydrogels remained almost constant after 20 cycles, indicating that the main chain of copolymer as a pendant of 9'-C on SPO had almost no effect on the fatigue resistance. This might be because the polymer chain caused little change of  $\pi$ -electrons of the photomerocyanine part and the heteroaromatic part, which led to little change in ground state energy of the closed-ring isomers and the energy gap between the open and closed ring isomers [35].

**3.3. In Vitro Drug Release Behavior.** The drug loading was achieved by immersing method using different media

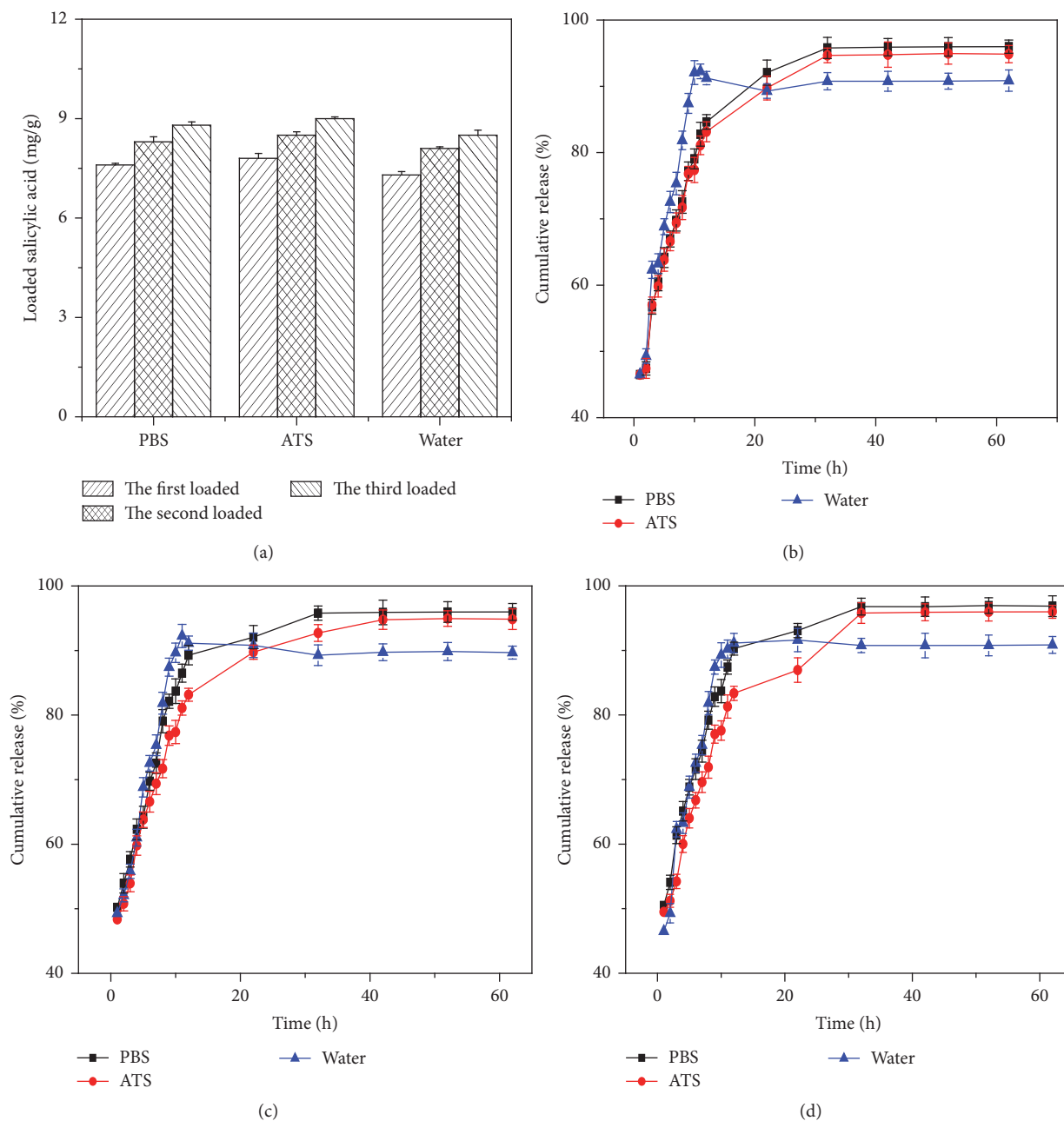


FIGURE 7: (a) Loaded salicylic acid amount in hydrogels for three times in different media, (b) salicylic acid release behavior in different media for first drug-loading, (c) salicylic acid release behavior in different media for second drug-loading, and (d) salicylic acid release behavior in different media for third drug-loading.

(Figure 7(a)). The equilibrium drug-loading amount in hydrogel was about  $9 \text{ mg g}^{-1}$ . From Figure 7(a), the amount of drug incorporated in hydrogel showed slight increase with times of loading, which might be ascribed to higher drug concentration of loading solution, coming from solvent evaporation. This phenomenon indicated the hydrogel could load drugs repeatedly. Moreover, the ions in loading solution showed little influence on drug-loading amount. Theoretically, Figures 7(b)–7(d) showed the drug-releasing behavior of salicylic acid in different media. For the first

time, the cumulative release rate of salicylic acid from the hydrogel was fast during 12 h in water, which was slow in PBS or in ATS until the release equilibrium was reached (Figure 7(b)). This difference in the cumulative release rate was reasonably attributed to salicylic acid charge screening brought by the ions in the salt solution; it caused the salicylic acid to be released slowly in PBS and ATS. For the second time, the cumulative release rate of salicylic acid was also fast in water or PBS until the release equilibrium was reached, while it was a little slower in ATS than in water (Figure 7(c)).

For the third time, salicylic acid was released along with time in each medium (Figure 7(d)). It was also found that all cumulative released drug rate reached above 89% no matter the characteristics of the medium and the release time of salicylic acid. By comparing Figures 7(b)–7(d), the drug release profile showed the drug-releasing behavior of hydrogel in water had little difference among the used time, and it also showed faster release in PBS or ATS than the last time. One of the main reasons affecting this drug-releasing behavior was the increase of the time hydrogel submerged in the salt solution that led to increase of ions of inner hydrogel, which decreased the charge screening brought by the ions.

#### 4. Conclusions

In this work, photochromic p(HEMA-NVP-SPO) hydrogel was successfully synthesized by radical polymerization, which was verified by IR spectra. Compared with pHEMA hydrogel, p(HEMA-NVP) copolymer hydrogel had larger equilibrium water content (EWC) and more homogenous porous structure. The formed p(HEMA-NVP-SPO) hydrogel possessed similar EWC and morphology to p(HEMA-NVP) hydrogel. The colorless p(HEMA-NVP-SPO) hydrogel could turn to blue after being irradiated at 365 nm and then recover back under visible light irradiation in 289 s. Theoretically, the thermal fading of hydrogel made by polymerization method was slower than that made by immersing method. Additionally, the photochromic hydrogel made by polymerization method exhibited a good fatigue resistance. The drug loading is realized by immersing method. The equilibrium drug-loading amount in hydrogel increased slightly with times of loading regardless of ions in solution. The sustained drug release in a given period was dependent on the characteristics of solution and loading time. The drug release profile in water showed little dependence on loading time, whereas faster release in PBS or ATS than that of the last time was detected.

#### Competing Interests

The authors declare that they have no potential conflict of interests regarding the publication of this article.

#### Acknowledgments

This work was financially supported by Research Fund for the Doctoral Program of Jinling Institute of Technology (jit-2012-27).

#### References

- [1] M. Irie, T. Lifka, S. Kobatake, and N. Kato, "Photochromism of 1,2-Bis(2-methyl-5-phenyl-3-thienyl)perfluorocyclopentene in a Single-Crystalline Phase," *Journal of the American Chemical Society*, vol. 122, no. 20, pp. 4871–4876, 2000.
- [2] Q.-L. Zhu, T.-L. Sheng, R.-B. Fu et al., "Redox-responsive photochromism and fluorescence modulation of two 3D metal-organic hybrids derived from a triamine-based polycarboxylate ligand," *Chemistry—A European Journal*, vol. 17, no. 12, pp. 3358–3362, 2011.
- [3] Q. Zhang, J. M. Li, L. H. Niu et al., "A rapid response photochromic diarylethene material for rewritable holographic data storage," *Chinese Science Bulletin*, vol. 58, no. 1, pp. 74–78, 2013.
- [4] D. L. Watkins and T. Fujiwara, "Bis-spiroanthoxazine based photochromic polymer materials," *Journal of Materials Chemistry C*, vol. 1, no. 3, pp. 506–514, 2013.
- [5] E. B. Gaeva, V. Pimienta, S. Delbaere et al., "Spectral and kinetic properties of a red-blue pH-sensitive photochromic spirooxazine," *Journal of Photochemistry and Photobiology A: Chemistry*, vol. 191, no. 2-3, pp. 114–121, 2007.
- [6] W. Yuan, L. Sun, H. Tang et al., "A novel thermally stable spiroanthoxazine and its application in rewritable high density optical data storage," *Advanced Materials*, vol. 17, no. 2, pp. 156–160, 2005.
- [7] D. L. Watkins and T. Fujiwara, "Synthesis, characterization, and solvent-independent photochromism of spiroanthoxazine dimers," *Journal of Photochemistry and Photobiology A: Chemistry*, vol. 228, no. 1, pp. 51–59, 2012.
- [8] G. Berkovic, V. Krongauz, and V. Weiss, "Spiropyrans and spirooxazines for memories and switches," *Chemical Reviews*, vol. 100, no. 5, pp. 1741–1753, 2000.
- [9] S. Kumar, D. L. Watkins, and T. Fujiwara, "A tailored spirooxazine dimer as a photoswitchable binding tool," *Chemical Communications*, no. 29, pp. 4369–4371, 2009.
- [10] E. Herrero, N. Carmona, J. Llopis, and M. A. Villegas, "Sensitive glasslike sol-gel materials suitable for environmental light sensors," *Journal of the European Ceramic Society*, vol. 27, no. 16, pp. 4589–4594, 2007.
- [11] A. K. Chibisov and H. Görner, "Photoprocesses in spirooxazines and their merocyanines," *The Journal of Physical Chemistry A*, vol. 103, no. 26, pp. 5211–5216, 1999.
- [12] V. S. Marevtsev and N. L. Zaichenko, "Peculiarities of photochromic behaviour of spiropyran and spirooxazines," *Journal of Photochemistry and Photobiology A: Chemistry*, vol. 104, no. 1-3, pp. 197–202, 1997.
- [13] X. L. Yang, B. J. Yang, Y. Y. Liu, and H. J. Zhu, "Microwave-assisted synthesis of novel spirooxazines and their photochromic behaviors in polymer matrices," *Optoelectronics and Advanced Materials-Rapid Communications*, vol. 6, no. 11, pp. 1146–1152, 2012.
- [14] X. Hu, L. Hao, H. Wang et al., "Hydrogel contact lens for extended delivery of ophthalmic drugs," *International Journal of Polymer Science*, vol. 2011, Article ID 814163, 9 pages, 2011.
- [15] K. T. Nguyen and J. L. West, "Photopolymerizable hydrogels for tissue engineering applications," *Biomaterials*, vol. 23, no. 22, pp. 4307–4314, 2002.
- [16] W. J. Seeto, Y. Tian, and E. A. Lipke, "Peptide-grafted poly(ethylene glycol) hydrogels support dynamic adhesion of endothelial progenitor cells," *Acta Biomaterialia*, vol. 9, no. 9, pp. 8279–8289, 2013.
- [17] X. H. Hu and D. Li, "Facile way to synthesise hydrogel contact lenses with good performance for ophthalmic drug delivery," *Materials Technology*, vol. 28, no. 4, pp. 192–198, 2013.
- [18] X. Hu, J. Qiu, H. Tan, D. Li, and X. Ma, "Synthesis and characterization of cyclodextrin-containing hydrogel for ophthalmic drugs delivery," *Journal of Macromolecular Science, Part A: Pure and Applied Chemistry*, vol. 50, no. 9, pp. 983–990, 2013.
- [19] X. H. Hu, H. P. Tan, D. Li, and M. Y. Gu, "Surface functionalisation of contact lenses by CS/HA multilayer film to improve its properties and deliver drugs," *Materials Technology*, vol. 29, no. 1, pp. 8–13, 2014.

- [20] X. Gong, "Controlling surface properties of polyelectrolyte multilayers by assembly pH," *Physical Chemistry Chemical Physics*, vol. 15, no. 25, pp. 10459–10465, 2013.
- [21] L. Zhang, X. Gong, Y. Bao et al., "Electrospun nanofibrous membranes surface-decorated with silver nanoparticles as flexible and active/sensitive substrates for surface-enhanced Raman scattering," *Langmuir*, vol. 28, no. 40, pp. 14433–14440, 2012.
- [22] X. Hu and X. Gong, "A new route to fabricate biocompatible hydrogels with controlled drug delivery behavior," *Journal of Colloid & Interface Science*, vol. 470, pp. 62–70, 2016.
- [23] X. Hu, H. Tan, and L. Hao, "Functional hydrogel contact lens for drug delivery in the application of ophthalmology therapy," *Journal of the Mechanical Behavior of Biomedical Materials*, vol. 64, pp. 43–52, 2016.
- [24] X. Hu, H. Tan, X. Wang, and P. Chen, "Surface functionalization of hydrogel by thiol-yne click chemistry for drug delivery," *Colloids and Surfaces A: Physicochemical and Engineering Aspects*, vol. 489, pp. 297–304, 2016.
- [25] X. Hu, H. Tan, P. Chen, X. Wang, and J. Pang, "Polymer micelles laden hydrogel contact lenses for ophthalmic drug delivery," *Journal of Nanoscience & Nanotechnology*, vol. 16, no. 6, pp. 5480–5488, 2016.
- [26] S. Wang, M.-S. Choi, and S.-H. Kim, "Bistable photoswitching in poly(N-isopropylacrylamide) with spironaphthoxazine hydrogel for optical data storage," *Journal of Photochemistry & Photobiology A: Chemistry*, vol. 198, no. 2-3, pp. 150–155, 2008.
- [27] T. Kardinahl and H. Franke, "Photoinduced refractive-index changes in fulgide-doped PMMA films," *Applied Physics A Materials Science & Processing*, vol. 61, no. 1, pp. 23–27, 1995.
- [28] P. S. Gils, D. Ray, and P. K. Sahoo, "Designing of silver nanoparticles in gum arabic based semi-IPN hydrogel," *International Journal of Biological Macromolecules*, vol. 46, no. 2, pp. 237–244, 2010.
- [29] M. M. Fares, S. M. Assaf, and A. A. Jaber, "Biodegradable amphiphiles of grafted poly(lactide) onto 2-hydroxyethyl methacrylate-co-N-vinylpyrrolidone copolymers as drug carriers," *Journal of Applied Polymer Science*, vol. 122, no. 2, pp. 840–848, 2011.
- [30] H. N. Al-Jallo and M. G. Jalhoom, "Spectral correlations for  $\alpha$ ,  $\beta$ -unsaturated acidhalides," *Spectrochimica Acta A*, vol. 31, no. 3, pp. 265–271, 1975.
- [31] X. Hu, L. Feng, W. Wei et al., "Synthesis and characterization of a novel semi-IPN hydrogel based on Salecan and poly(N,N-dimethylacrylamide-co-2-hydroxyethyl methacrylate)," *Carbohydrate Polymers*, vol. 105, no. 1, pp. 135–144, 2014.
- [32] S. Schneider, "Investigation of the photochromic effect of spiro [indolino-naphthoxazine] derivatives by time-resolved spectroscopy," *Zeitschrift für Physikalische Chemie*, vol. 154, pp. 91–119, 1987.
- [33] C. Shin and H. Lee, "Effect of alkyl side-chain length and solvent on the luminescent characteristics of poly(3-n-alkylthiophene)," *Synthetic Metals*, vol. 140, no. 2-3, pp. 177–181, 2004.
- [34] R. Nakao, F. Noda, T. Horii, and Y. Abe, "Thermal stability of the spironaphthoxazine colored form in polymeric siloxanes," *Polymers for Advanced Technologies*, vol. 13, no. 2, pp. 81–86, 2002.
- [35] T. Feczko, O. Varga, M. Kovács, T. Vidóczy, and B. Voncina, "Preparation and characterization of photochromic poly(methyl methacrylate) and ethyl cellulose nanocapsules containing a spirooxazine dye," *Journal of Photochemistry & Photobiology A: Chemistry*, vol. 222, no. 1, pp. 293–298, 2011.

## Review Article

# Polylactic Acid Based Nanocomposites: Promising Safe and Biodegradable Materials in Biomedical Field

Lili Sha,<sup>1,2</sup> Zhaofeng Chen,<sup>1,2</sup> Zhou Chen,<sup>1,3</sup> Aili Zhang,<sup>3</sup> and Zhaogang Yang<sup>3</sup>

<sup>1</sup>College of Material Science and Technology, Nanjing University of Aeronautics and Astronautics, Nanjing 210016, China

<sup>2</sup>Suqian NUAU Institute of New Materials and New Equipment Manufacturing Co., Ltd., Suqian 223800, China

<sup>3</sup>Nanoscale Science and Engineering Center, The Ohio State University, Columbus, OH 43210, USA

Correspondence should be addressed to Zhaofeng Chen; cz6327725@163.com and Zhaogang Yang; yzhaogang@gmail.com

Received 28 June 2016; Accepted 31 August 2016

Academic Editor: Ming Zhang

Copyright © 2016 Lili Sha et al. This is an open access article distributed under the Creative Commons Attribution License, which permits unrestricted use, distribution, and reproduction in any medium, provided the original work is properly cited.

Poly(lactic acid) (PLA) is widely used in biological areas due to its excellent compatibility, bioabsorbability, and degradation behavior in human bodies. Pure poly(lactic acid) has difficulty in meeting all the requirements that specific field may demand. Therefore, PLA based nanocomposites are extensively investigated over the past few decades. PLA based nanocomposites include PLA based copolymers in nanometer size and nanocomposites with PLA or PLA copolymers as matrix and nanofillers as annexing agent. The small scale effect and surface effect of nanomaterials help improve the properties of PLA and make PLA based nanocomposites more popular compared with pure PLA materials. This review mainly introduces different kinds of PLA based nanocomposites in recent researches that have great potential to be used in biomedical fields including bone substitute and repair, tissue engineering, and drug delivery system.

## 1. Introduction

Biological materials have experienced enormous development in the past 30 years. Even when there was an economic downturn near 2008, the usage of biomaterials maintains an increase of 13% every year, showing strong vitality and wide prospect. Fast development of biomaterials improved living standard of humans to a great extent. In the meantime, biomaterial science, which aims to search for perfect biocompatibility, improved interaction between cells and materials, tailored degradation rate, synthetic materials design, and other particular properties of polymers, metals, and ceramics, has also attracted much attention [1–11]. It is usually these three classes, either single ingredient or in many cases, composite ingredients, that are used as biomaterials [12–15].

Different from metal and ceramic, polymer offers an organic matrix and its molecular is easier to control [16, 17]. It is relatively hard to define and conclude the physical and chemical performance of polymers because the properties of different polymers vary extremely. There are generally two

categories of polymers, biodegradable and nonbiodegradable polymers. Biodegradable polymer is more environmentally friendly and frequently used for medical devices due to its excellent degradation behavior in human body and the purpose of environment protection. Degradation rate can also be controlled after some modification or by designing the proportion of different polymers in order to meet practical demands [13, 18]. Biodegradable polymers then can be further divided into naturally derived materials and synthetically prepared materials. Among synthetically prepared materials, saturated poly- $\alpha$ -hydroxyl esters are more commonly used in biomedical field, especially poly(lactic acid) (PLA) [19]. The degradation products of PLA are usually water and carbon dioxide that do not cause any harm; more importantly, they can be cleared out of human body totally, making PLA the most popular biomedical material in the market.

PLA is a kind of linear aliphatic polyester derived from renewable resources such as corn, sugar, potato, and other agricultural products [20–22], whose properties are determined by many factors, such as the component isomers,

preparing temperature, and molecular weight. Generally, there are three kinds of PLA, poly(D-lactic acid) (PDLA), poly(L-lactic acid) (PLLA), and the racemic blend D,L-PLA (PDLLA), based on different microstructures. PLLA and the racemic blend PDLLA are semicrystalline with slightly different glass transition temperatures, while D-PLA (PDLA) is always amorphous [23]. Degree of crystallization as well as the reactivity of polymer is sensitive to the ratio of D to L enantiomers used. Different structures of these three PLA materials decide that each kind of PLA has its applicable field. For example, PDLLA is often used in drug delivery system owing to its monophasic structure, but PLLA is more likely to be used where good mechanical behavior is essential. However, pure PLA materials inevitably present much restriction when put into use, such as brittle behavior, poor osteoinduction, and uncontrolled degradation rate. For a long time, many types of chemicals, such as citrate esters [24], and some low-molecular-weight plasticizers such as sorbitol and glycerol have been widely used in this area to plasticize PLA. Plasticizers such as glucose monoesters, poly(ethylene glycol) (PEG), and partial fatty acid esters [25] were also tried to improve the impact resistance and the flexibility of PLA, but the biocompatibility of PLA materials is not that easy to improve so that PLA based nanocomposites appear.

PLA based nanocomposites, which include PLA based copolymers in nanometer size and nanocomposites with PLA or PLA copolymers as matrix and nanofillers as annexing agent, have shown great potential in biomedical field [26]. The small scale effect and surface effect nanomaterials have particularly helped improve the properties of PLA and make PLA based nanocomposites more popular compared with pure PLA materials when it comes to synthetic bone substitute and repair, tissue engineering, and drug delivery system.

Among all the PLA based copolymers, poly(lactic-glycolic acid) (PLGA) has attracted the most public attention and has been approved by FDA for clinical uses. It can be obtained from lactide monomer and polyglycolic acid (PGA) by ring-opening polymerization, which nowadays turns out to be the most efficient way to prepare high-molecular-weight polylactic acid as well as PLA based copolymers. Compared with conventional polycondensation, the polymerization efficiency of ring-opening polymerization can be guaranteed and some intended properties of polymers can also be obtained [27]. Other diversified polymers, such as polyethylene oxide [28], polyvinyl acetate [29], and polyethylene glycol [30], can also be polymerized with PLA for specific applications.

Nanocomposites with PLA or PLA copolymers as matrix significantly help improve PLA's properties and overcome its shortcomings. Several studies have been performed using some fillers such as clay minerals, carbon nanotubes, and graphene and its precursor to obtain nanocomposite materials [31–34]. Polymer nanocomposites exhibit apparently improved properties when compared with pure polymers or their traditional composites [35–38]. Pinto et al. [39] discussed the effect of small amounts (0.2 to 1 mass%) of graphene oxide and graphene nanosheets on functional properties of polylactic acid films. Their results showed

that yield strength, Young's modulus, and impermeability of resulting nanocomposites were higher than those of pristine PLA. Beside these three nanomaterials, organomontmorillonite and natural nanofibers are also typical annexing agents. Synergy usually exists between different fillers when they are added together into PLA matrix [40]. Fillers mentioned above such as clay minerals, carbon nanotubes, and nanofibers are more frequently used to improve the mechanical properties of PLA materials. In the case of biomaterials, biocompatibility and bioactivity should be paid more attention. In the field of bone substitute and repair, calcium phosphate ceramics such as hydroxyapatite and  $\beta$ -tricalcium phosphate play important roles owing to their higher biological compatibility. When it comes to tissue engineering, additives such as collagen, graphene oxide, and demineralized bone particle are diffusely investigated in many researches. As for drug delivery system, PLGA nanoparticles attract extensive concern and montmorillonite is also reported to be beneficial in prolonging the drug releasing time (see later in this review).

With the development of manufacturing technology, the shape of PLA based nanocomposites is also tending to be various. Different shapes of foams, meshes, films, fibers, or microspheres are all available. This review will be dedicated to introducing some update research progresses with an eye to the applications of PLA based nanocomposites as biomaterials.

## 2. Synthetic Bone Substitute and Repair

Over the past few decades, the incidence of various bone diseases has been increasing and traffic accidents happen more frequently with the development of human's living standard, inducing a growing need for synthetic bone substitute materials or bone repair materials. Bone of human body has a high chance of being damaged or lost in injuries or just due to pathologic changes. Now the reconstruction of bone has been a major focus point in preclinical research and clinical application, giving rise to the development of materials that help to regenerate bone and repair bone defects [41–43]. Bone defect repair is really common in orthopedic surgeon [44], where synthetic bone substitutes must be used and implanted in human bodies and it is of great importance to find suitable substitutes.

An ideal and suitable bone substitute should possess outstanding biocompatibility and osteoinductive and osteoconductive properties [45]. In previous studies, bioabsorbable polymer devices with nontoxicity have been widely used in orthopedic surgery including fractures repair and bone replacement. Pins, plates, and screws are those frequently used forms of polymer devices in oral, orthopedic, and craniofacial surgeries [46–49]. PLA and PLGA are two promising materials which are widely studied and used to prepare porous scaffolds and repair damaged bones [19, 50, 51]. The superior degradation of PLA materials makes no necessity for second operation and prevents implant removal so that the pain of patients can be alleviated. Plus, using PLA materials helps avoid stress block and reduce the risk of operation failure. However, pure PLA materials lack bone-bonding

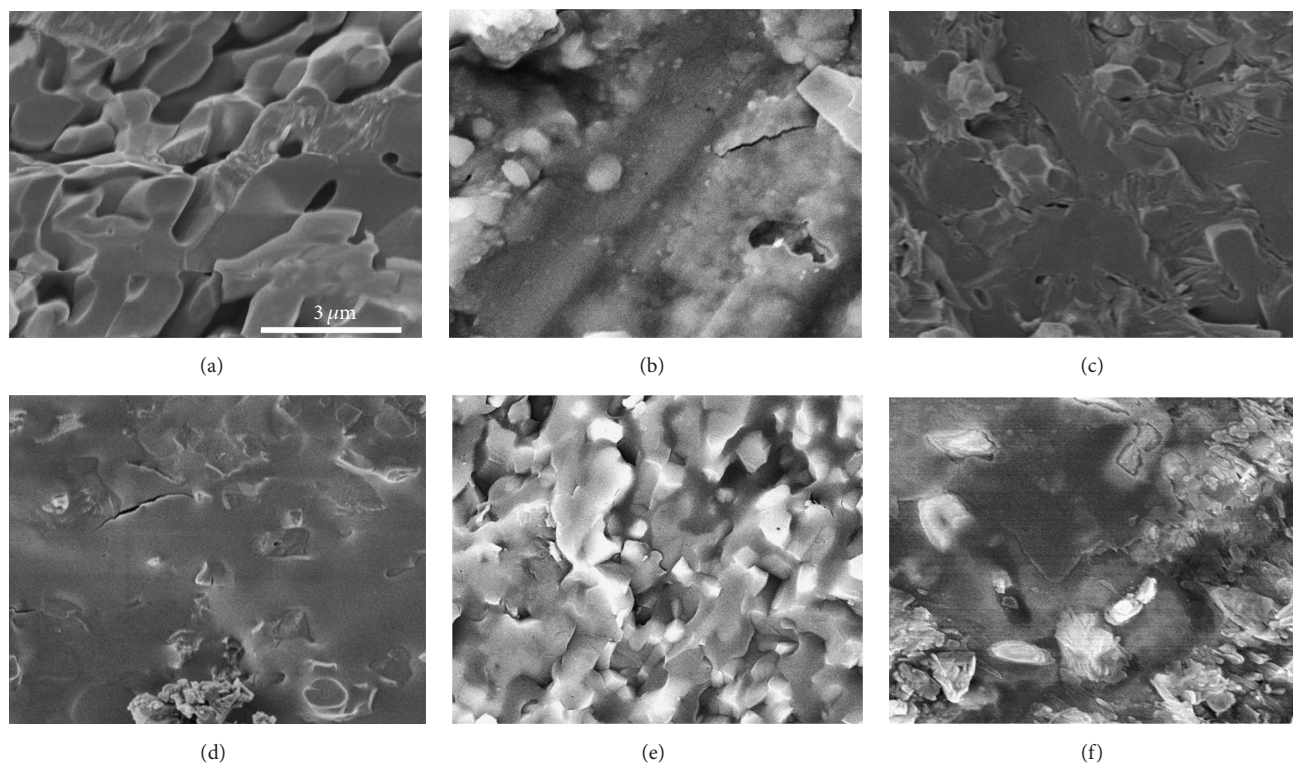


FIGURE 1: Cross-sectional scanning electron microscopy images of (a) HAp, (b) PGA/HAp, (c) PLGA20/HAp, (d) PLGA50/HAp, (e) PLGA80/HAp, and (f) PLLA/HAp composites polymerized at 100°C for 9 days (originally adapted from [63]).

force and the regeneration efficacy and degradation behavior of PLA are not as good as PLA based nanocomposites.

Schneider et al. [52–54] successfully prepared a flexible nanocomposite with a cotton wool-like appearance through an electrospinning process. Amorphous tricalcium phosphate nanoparticles (TCP) were added to the biodegradable copolymer PLGA (PLGA/TCP60:40). This characteristic of the material with a typical cotton wool-like shape can be adapted in any bone defect due to its superior moldability. Compared with PLGA-treated defects, the closure behavior of PLGA/TCP-treated defects improved a lot in almost all nine New Zealand white rabbits. Moreover, resorption of graft material four weeks after implantation was also reported later [54].

Hydroxyapatite (HAp) is one of the calcium phosphate ceramics that have been largely used as artificial bone materials. The similarity to human bone elements and excellent biocompatibility enable hydroxyapatite to be used as suitable implant in many surgical operations [55–57]. HAp has also been widely added to PLA matrix and HAp-PLLA composites obtained exhibit superior biological performance [58–62]. Takeoka et al. [63] managed to polymerize L-lactide and glycolide in situ and several PLGA/HAp composites with different ratio of L-lactide and glycolide in porous HAp disks were successfully obtained. Scanning electron microscopy result (Figure 1) indicated that porous HAp was completely full of PLGA after polymerization at 100°C for 9 days while PLLA/HAp composites were found containing continuous open pores. After 5 h cultivation of MC3T3-E1 cells,

PLGA20/HAp presented the most adhesion ratio of  $38.8 \pm 3.7$ , almost twice of PGA/HAp composites, suggesting that these PLGA/HAp composites had suitably bioactive surfaces. After immersion in PBS, the pH value of PLGA80/HAp was even over 7.0, which was beneficial to relieve the inflammatory reaction that plants may cause after degradation.

Beside hydroxyapatite, bioactive glass particles such as Bioglass 45S5 [64] also have attracted much attention due to the great importance of controlling degradation rate of PLA composites used as bone fixation devices, which can be affected by crystallinity, molecular weight, size, and shape of the specimens. Many researches ascertain that the existence of bioactive glass facilitates the degradation of polymers and there will be an initial sharp weight loss due to the dissolution of the bioglass [65, 66]. When the bioglass comes into contact with human body fluids, the local environment turns alkaline gradually along with the salting-out of bioglass, just to be able to neutralize lactic acid and slow down the degradation rate of polymers. In general, almost all the studies show a close relationship between bioglass and the degradation of polymer matrix; that is to say, the loss of molecular weight is related not only to autocatalytic degradation, but also to bioglass dissolution itself. Vergnol et al. [67] combined PLLA with Bioglass 45S5 particles and in vitro cell viability testing together with in vivo experiment on rabbits was conducted. Results suggested that the existence of bioglass in composites really accelerated the degradation of polymer and a bioglass proportion of 30 wt% seemed to be able to promote bone osseointegration especially during the first month of

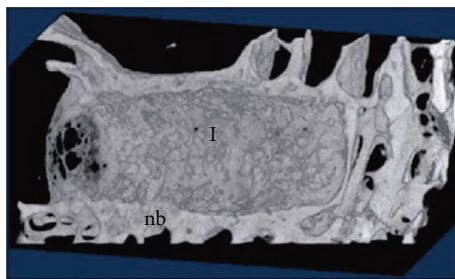


FIGURE 2: The 3D reconstruction of the bone around a composite C30 implant after 6 months of implantation (with ImageJ software) (I = implant; nb = newly formed bone) (originally adapted from [67]).

implantation. A white line representing the formation of new bone surrounding the implants can be clearly observed on X-ray tomography and 3D picture after one month (Figure 2). All these results indicated that this composite with 30 wt% of bioglass particles had thus strong potential for health applications.

Bone allograft owns good osteoconduction and osteoinduction, whose chemical components resemble bone autograft, but its clinic application has been limited because of its difficulty of shaping, poor porosity, and bad degradation behavior. Demineralized bone matrix (DBM) emerges in this situation; the collagen and osteoinductive growth factors which it contains really do good for bone regeneration. DBM formulations are various in market, such as granules, powder, gel, putty, and paste, only depending on the manufacturing method. However, the mechanical properties and porosity of DMB are relatively poor, no matter which formulation [68]. Zhang et al. [45] prepared porous PLA/DBM composite biomaterials by supercritical CO<sub>2</sub> technique, which is a new preparation method, especially suitable for the processing of bioactive materials containing growth factors. Results showed that the mechanical properties of composites are significantly improved. Compared with pure PLA and bone autograft, the repairing effect of PLA/DBM composite to bone is better than PLA and is almost the same as bone autograft, reflected from the X-ray result and histological analysis. Finally the feasibility for PLA/DBM to repair bone defects was put forward by the author.

In the field of bone substitute and repair, the degradation rate, degradation products, mechanical property, and bioactivity of the implant materials must be taken into consideration. These properties of PLA or PLGA will be improved with tricalcium phosphate nanoparticles, hydroxyapatite, bioglass, or demineralized bone matrix added to it. The proportion of these fillers also have sensitive influence on the properties of PLA based nanocomposites.

### 3. Tissue Engineering

Tissue engineering, which focuses on the formation and regeneration of tissues and organs, is now an emerging area in human healthcare area. It has facilitated numerous humans due to the long-term dedication to the structure, function,

and growth mechanism of biological tissues against the background of cellular biology and bioengineering development. Scaffolds, as the carriers of cell adhesion and growth, play a decisive role in tissue engineering and have been used in many branches, such as bone regeneration [69], blood vessel [70], and neural system [71]. Ideal scaffolds should not only have suitable construction beneficial to cells growing but also have excellent biofunctionality because the behavior of cells can be easily influenced by the local environment, including some biochemical and mechanical cues [72].

PLA materials are widely used as scaffolds due to its good biocompatibility. The different efficacy aligned and random PLLA nano/microfibrous scaffolds have for neural tissue engineering has been compared [71]. Results showed that neural stem cells (NSC) and its neurite outgrowth had tendency to elongate in the direction parallel to PLLA fibers for aligned scaffolds and there seemed to be no relation between cell differentiation rate and fiber arrangement, while nanofibers exhibited better differentiation performance compared with microfibers, indicating the great potential aligned nanofibrous PLLA scaffold has for neural tissue engineering. Many other biomaterials such as collagen and graphene oxide are gradually introduced to polymerize with PLA or PLGA in order to obtain optimized scaffold structures. Qiao et al. [69] blended type I collagen with PDLA and finally found that when type I collagen occupied a proportion of 40% in the scaffolds, PDLA/collagen scaffolds showed greatest stability, cell proliferation, and osteogenic differentiation after five-week cultivation. As is shown in Figures 3(a) and 3(b), PDL60/Col and PDL60/Gel scaffolds have the same size of 500–1000 nm in diameter. However, in Figures 3(c), 3(d), and 3(e), the number of cells attached to PDL60/Col scaffolds is obviously greater than those attached to PDL60/Gel scaffolds. Moreover, cells on PDL60/Gel scaffolds are spherical in shape while cells on PDL60/Col scaffolds are flat, which also indicates better cell adhesion property of PDL60/Col scaffolds compared with PDL60/Gel scaffolds.

Shin et al. [72] successfully fabricated hybrid fiber matrices GO-PLGA-Col composed of PLGA and collagen (Col) impregnated with GO via an electrospinning technique. Component analysis suggested a well-proportioned distribution of GO all over the GO-PLGA-Col matrices. The hydrophilicity of the matrices was extensively increased only even though a small amount of Col and GO was added. Results also showed that these hybrid matrices helped induce spontaneous myogenesis which made it the appropriate candidate for skeletal tissue engineering.

Electrospinning process was well utilized in the researches mentioned above [69, 71, 72] and electrospinning is indeed an effective way to prepare scaffolds due to its numerous superiorities such as mass production capability and high surface areas of scaffolds. However, there are many other methods including solvent casting/particulate leaching [73], phase separation [74], emulsion freeze-drying [75], gas formation [76], and fiber bonding [77]. Ziabari et al. [77] successfully fabricated PLGA scaffolds with demineralized bone particle (DBP) via the solvent casting/salt leaching method. Cell growth and gene expression of smooth muscle cells (SMCs) were upregulated with DBP in PLGA scaffold.

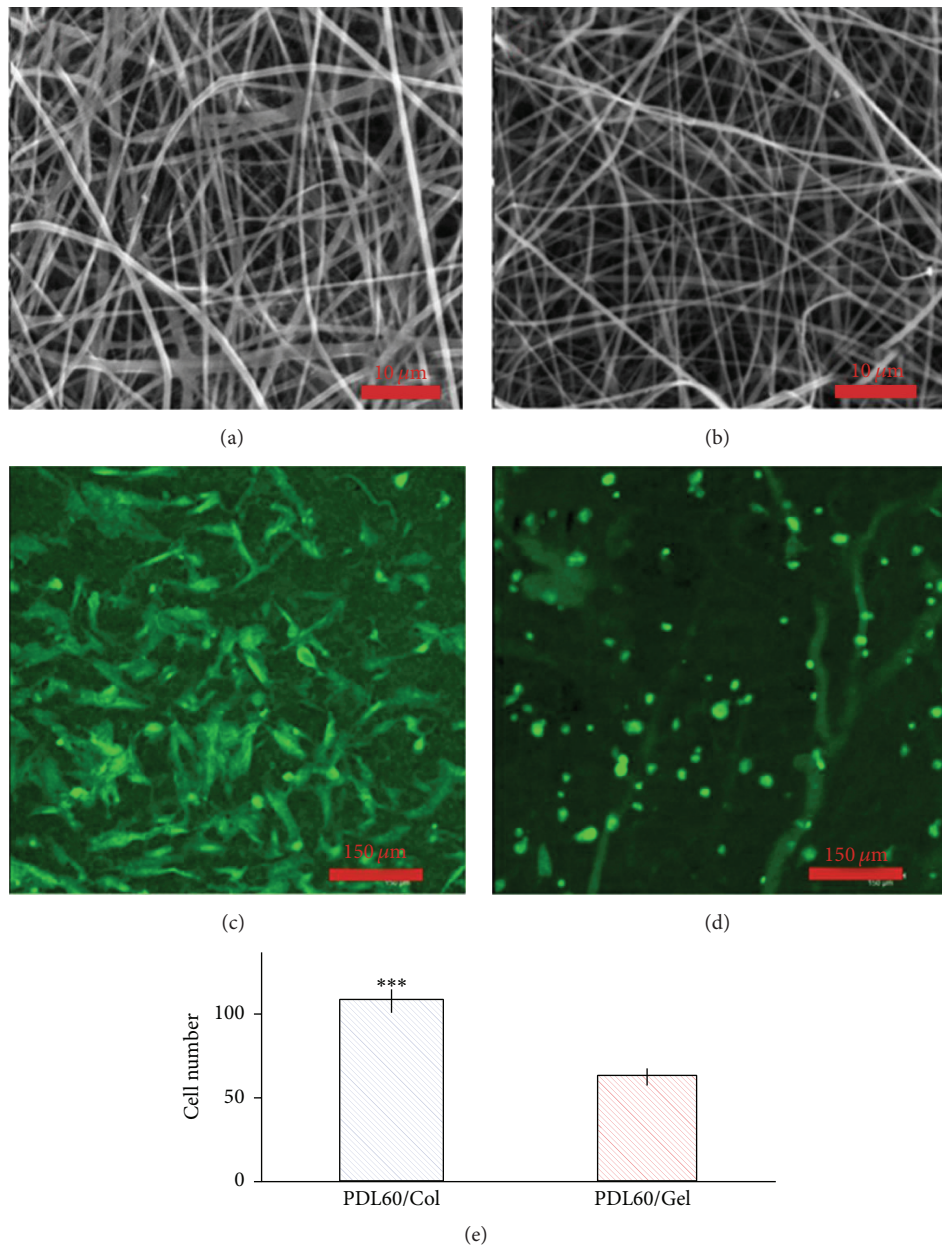


FIGURE 3: HBMSCs attachment on the PDL60/Col and PDL60/Gel electrospun scaffolds. (a, b) are SEM images of PDL60/Col scaffolds and PDL60/Gel scaffolds, respectively. (c, d) are maximum projection fluorescence images of PDL60/Col and PDL60/Gel cell-scaffold constructs, respectively. (e) Cell numbers were counted based on the confocal images (originally adapted from [69]). \*\*\*PDL60.

Ardjomandi et al. [78] prepared a series of coatings of  $\beta$ -tricalcium phosphate scaffolds through dip-and-dry coating and then angularity and topography of the developed scaffolds were analyzed. In the long term, it is really difficult to control and design the pore size and interconnectivity of scaffold [79, 80]. What is worse, the organic solvents used may cause some damage to cells or tissues [79]. The appearance of a new method called 3D printing based on computer-aided design (CAD) can perfectly solve this intractable problem and it has led to a revolution in manufacturing industry. Shim et al. [81] recently creatively

prepared a resorbable semi-dome-shaped polycaprolactone (PCL)/PLGA/ $\beta$ -TCP membrane through a 3D printing system (Figure 4), with both rapid degradation rate of PLGA and high elasticity of PCL taken into consideration. In vitro mechanical and cytology test, in vivo preclinical implanting experiment, and a comparison with a titanium membrane were all conducted. When bone regeneration experiment was performed on oral bone defects, results showed the PCL/PLGA/ $\beta$ -TCP membrane had almost similar properties to those nonresorbable and commonly used titanium mesh membrane, such as osseointegration and the ability to form



FIGURE 4: A PCL/PLGA/ $\beta$ -TCP membrane produced using 3D printing technology. Pores were triangularly structured and completely interconnected (originally adapted from [81]).

new bone around the implants. This 3D printing technique coordinating with this biomaterial provided a new choice for tissue engineering field.

Novel ideas and structures of scaffolds are emerging endlessly and have achieved considerable research achievements. Davachi et al. [82] melt-mixed a high-molecular-weight PLLA and 30% encapsulated triclosan with a low-molecular-weight PLLA (LATC30) in different proportions. Results showed that PLA3 (with 5% LATC30) was opted to be the most suitable candidate for bone tissue engineering, which was mainly because the encapsulation of triclosan had reduced its negative effect near the tissue environment. Besides, P(LA-co-CL) copolymer with a star shape has attracted public attention. Shafiq et al. [83] recently mixed P(LA-co-CL) and substance P(SP-) conjugated star-shaped P(LA-co-CL) copolymers in appropriate ratios and then fabricated nonwoven meshes via electrospinning. Meshes containing P(LA-co-CL) and SP were then set subcutaneously in Sprague-Dawley rats. Cellularization of P(LA-co-CL) as well as SP-containing meshes was revealed when proceeding hematoxylin and eosin staining test. A large amount of mature blood vessels was later observed in SP-containing meshes compared with their control counterparts, further proving the possibility that these novel scaffolds have to be applied in tissue regeneration of soft tissues.

In general, great efforts have been made to increase cell adhesion and cell proliferation on the surface of scaffolds in the field of tissue engineering. Different kinds of collagen and other additives have also been added to increase the surfactivity of PLA or PLGA. In this field, technologies of tissue regeneration turn out to be mature while the feasibility of PLA based nanocomposites being used in blood vessel and neural system needs to be further demonstrated through plentiful experiments, which might be the new future direction of PLA based nanocomposites as well.

#### 4. Drug Delivery System

Conventional drug formulations usually suffer the drawback of uncontrollable therapeutic drug level in human body so that good curative effect cannot be guaranteed. Patients have to take medicine several times a day in order to maintain a certain drug level, which has undesirable side effects and is also a burden mentally. Drug delivery system is therefore a

pivotal link in drug therapy [84–86], which aims to maintain a sustained blood drug concentration by delivering the drug to the microenvironment in a good time and at a certain rate gradually, meanwhile avoiding the decomposition of drugs [87, 88]. More importantly, it can be acted on a targeted area of human body. The primary characteristics of this system include biodegradability, biocompatibility, nontoxicity, prolonged circulation, and a wide payload spectrum of a therapeutic agent [89]. Nowadays, nanoparticles of biodegradable polymers are extensively used to improve the therapeutic effect of various water soluble or water insoluble drugs. The presence of those nanoparticles helps to improve bioavailability, solubility, and retention time of the drugs in human bodies and further bioactive molecules are also expected [90, 91]. All the biodegradable polymer nanoparticles can be approximately divided into two categories, one is nanocapsule and the other is nanosphere [92]. The drug molecules exist inside the polymer or absorbed on the surface.

Poly(lactic acid) (PLA) has been mostly exploited to prepare biodegradable nanoparticles by solvent evaporation, solvent displacement [93], salting-out [94], and solvent diffusion. As a result, these drug carriers represent a marvelous efficacy in the encapsulation of psychotic drugs (savoxepine) [95], restenosis drugs (tyrphostins) [96], hormones (progesterone) [97], oridonin [98], and protein (BSA) [99] as well as enhance the used ratio of drugs and alleviate the damage to liver and kidney. Extra drug delivery may occur due to the looser structure when PLA degrades gradually with the extension of retention time, perfectly compensating the less drug delivery arising from the decrease of total drug dose so that a sustained drug delivery system forms.

Besides single poly(lactic acid) carrier, abundant copolymers of PLA have also been put into research. Sánchez et al. [100] found that polymerized PLA/TCP carrier can release 60% of the gentamicin in the first week and the retention time can reach 4 weeks. As for developing nanoparticles encapsulating therapeutic drugs in controlled releasing field, PLGA and its various derivatives stand out among all the copolymers and have been the center focus [101–103]. Ueng et al. [104, 105] concluded that polymerized poly(DL-lactide co-glycolide) nanosphere is an ideal drug-loaded material. Govender et al. [101] incorporated procaine hydrochloride into PLGA nanoparticles by nanoprecipitation and found that drug incorporation efficiency can be adjusted by changing pH value of aqueous phase, replacing procaine hydrochloride with procaine dihydrate or adding excipients without size to further influence the drug delivery efficiency.

Numerous block copolymers consisting of PLGA alternating with hydrophilic moieties like poly(ethylene oxide) (PEO) or poly(ethyleneglycol) (PEG) [106–108] also have been synthesized. Recently, Khodaverdi et al. [109] managed to prepare thermosensitive PLGA-PEG-PLGA triblock copolymers as in situ gelling matrices and in vitro drug release studies showed that it was molecular weight that decided drug release rate, copolymers concentration, and their microstructures in formulations. The authors also highlighted that PLGA-PEG-PLGA with a lactide-to-glycolide

ratio of 5:1 is the optimal system for long-acting controlled release of naltrexone hydrochloride and vitamin B12.

Other biomedical materials, such as fibrin [110], collagen sponge [111], chitosan [112], and bone matrix gelatin (BMG) [113], are also applied to drug carriers due to their excellent bioabsorbability and degradation behavior. Lal and Datta [114] recently developed montmorillonite- (Mt-) PLGA nanocomposites by w/o/w double emulsion solvent evaporation method as sustained release oral delivery vehicle for atenolol (ATN). For Mt-ATN-PLGA nanocomposites (ATN-03 and ATN-05), the release of the drug in simulated gastric fluid in the initial 0.5 h was 1.6% and 4%, respectively, far less than 32% of ATN-PLGA nanoparticles. In addition, cumulative release of Mt-ATN-PLGA nanocomposites reached only 70.4% and 72.4%, respectively, in 24 h while cumulative release of ATN-PLGA nanoparticles approached to 100% over a period of 12 h. Experiments conducted in simulated intestinal fluid also showed the same advantage that Mt-ATN-PLGA nanocomposites had in prolonging the gastric residence time of ATN, further indicating possibility of designing the sustained release formulations with improved bioavailability and patient compliance.

However, it still remains a challenge to prepare and store the drug and when PLGA degrades, the surrounding acid environment has a negative effect on protein stability [115]. Constant degradation results in accumulation of acidic monomers; lactic and glycolic acids may occur inside the drug delivery device after constant degradation; then the pH value of the microenvironment surrounded may reduce and the encapsulated proteins may get easy to denature [116]. To overcome these drawbacks of PLGA, great efforts and large investigations have to be conducted further.

## 5. Conclusion

Poly(lactic acid) is a degradable and nontoxic polymer, which has been widely used as bone substitute and repair material or used in tissue engineering and drug releasing field. However, the application of pure PLA materials is greatly limited due to the accurate and high requirements for material properties. When evaluating PLA materials used in bone regeneration, degradation rate, degradation products, mechanical property, and bioactivity of the implant materials are decisive. As for tissue engineering, researchers paid more attention to how to increase cell adhesion and proliferation ratio of cells on material surfaces. PLA materials are usually prepared porous when applied in drug delivery system, where it is of great importance to control releasing rate, releasing time, and pH value of the microenvironment surrounded. Common nanoparticles, such as hydroxyapatite, bioactive glass particles, collagen, and graphene oxide, usually own excellent biocompatibility and other functional properties. Once recombined with PLA or the copolymer of PLA, the nanocomposites are expected to greatly expand the application areas of PLA materials.

## Competing Interests

The authors declare that they have no competing interests.

## Acknowledgments

This work was supported by the Priority Academic Program Development of Jiangsu Higher Education Institutions.

## References

- [1] R. Langer and D. A. Tirrell, "Designing materials for biology and medicine," *Nature*, vol. 428, no. 6982, pp. 487–492, 2004.
- [2] L. J. Lee, Z. Yang, M. Rahman et al., "Extracellular mRNA detected by tethered lipoplex nanoparticle biochip for lung adenocarcinoma detection," *American Journal of Respiratory & Critical Care Medicine*, vol. 193, no. 12, pp. 1431–1433, 2016.
- [3] J. Xie, Z. Yang, C. Zhou, J. Zhu, R. J. Lee, and L. Teng, "Nanotechnology for the delivery of phytochemicals in cancer therapy," *Biotechnology Advances*, vol. 34, no. 4, pp. 343–353, 2016.
- [4] Z. Chen, A. Zhang, J. Hu, X. Wang, and Z. Yang, "Electrospun nanofibers for cancer diagnosis and therapy," *Biomaterials Science*, vol. 4, no. 6, pp. 922–932, 2016.
- [5] Z. Yang, L. Chang, C.-L. Chiang, and L. J. Lee, "Micro-/nanoelectroporation for active gene delivery," *Current Pharmaceutical Design*, vol. 21, no. 42, pp. 6081–6088, 2015.
- [6] C. Zhou, Z. Yang, and L. Teng, "Nanomedicine based on nucleic acids: pharmacokinetic and pharmacodynamic perspectives," *Current Pharmaceutical Biotechnology*, vol. 15, no. 9, pp. 829–838, 2015.
- [7] Z. Yang, B. Yu, J. Zhu et al., "A microfluidic method to synthesize transferrin-lipid nanoparticles loaded with siRNA LOR-1284 for therapy of acute myeloid leukemia," *Nanoscale*, vol. 6, no. 16, pp. 9742–9751, 2014.
- [8] Y. Wen, W. Liu, C. Bagia et al., "Antibody-functionalized peptidic membranes for neutralization of allogeneic skin antigen-presenting cells," *Acta Biomaterialia*, vol. 10, no. 11, pp. 4759–4767, 2014.
- [9] Y. Wen, H. R. Kolonich, K. M. Kruszewski, N. Giannoukakis, E. S. Gwalt, and W. S. Meng, "Retaining antibodies in tumors with a self-assembling injectable system," *Molecular Pharmaceutics*, vol. 10, no. 3, pp. 1035–1044, 2013.
- [10] W. Liu, M. J. Saunders, C. Bagia et al., "Local retention of antibodies in vivo with an injectable film embedded with a fluorogen-activating protein," *Journal of Controlled Release*, vol. 230, pp. 1–12, 2016.
- [11] L. Zhang, X. Gong, Y. Bao et al., "Electrospun nanofibrous membranes surface-decorated with silver nanoparticles as flexible and active/sensitive substrates for surface-enhanced Raman scattering," *Langmuir*, vol. 28, no. 40, pp. 14433–14440, 2012.
- [12] C. Holderegger, P. R. Schmidlin, F. E. Weber, and D. Mohn, "Preclinical in vivo performance of novel biodegradable, electrospun poly(lactic acid) and poly(lactic-co-glycolic acid) nanocomposites: a review," *Materials*, vol. 8, no. 8, pp. 4912–4931, 2015.
- [13] J. Xie, L. Teng, Z. Yang et al., "A polyethylenimine-linoleic acid conjugate for antisense oligonucleotide delivery," *BioMed Research International*, vol. 2013, Article ID 710502, 7 pages, 2013.
- [14] B. Yu, X. Wang, C. Zhou et al., "Insight into mechanisms of cellular uptake of lipid nanoparticles and intracellular release of small RNAs," *Pharmaceutical Research*, vol. 31, no. 10, pp. 2685–2695, 2014.

- [15] Z. Chen, M. Cong, J. Hu, Z. Yang, and Z. Chen, "Preparation of functionalized TiO<sub>2</sub> nanotube arrays and their applications," *Science of Advanced Materials*, vol. 8, no. 6, pp. 1231–1241, 2016.
- [16] X. Gong, "Controlling surface properties of polyelectrolyte multilayers by assembly pH," *Physical Chemistry Chemical Physics*, vol. 15, no. 25, pp. 10459–10465, 2013.
- [17] X. Gong, "Facile formation of nanoparticle patterns by water induced flow of a polymer thin film," *RSC Advances*, vol. 4, no. 97, pp. 54494–54499, 2014.
- [18] N. A. Peppas and R. Langer, "New challenges in biomaterials," *Science*, vol. 263, no. 5154, pp. 1715–1720, 1994.
- [19] K. Rezwani, Q. Z. Chen, J. J. Blaker, and A. R. Boccaccini, "Biodegradable and bioactive porous polymer/inorganic composite scaffolds for bone tissue engineering," *Biomaterials*, vol. 27, no. 18, pp. 3413–3431, 2006.
- [20] A. Araújo, G. Botelho, M. Oliveira, and A. V. Machado, "Influence of clay organic modifier on the thermal-stability of PLA based nanocomposites," *Applied Clay Science*, vol. 88–89, pp. 144–150, 2014.
- [21] T. Kuang, L. Chang, F. Chen, Y. Sheng, D. Fu, and X. Peng, "Facile preparation of lightweight high-strength biodegradable polymer/multi-walled carbon nanotubes nanocomposite foams for electromagnetic interference shielding," *Carbon*, vol. 105, pp. 305–313, 2016.
- [22] T. R. Kuang, H. Y. Mi, D. J. Fu et al., "Fabrication of poly(lactic acid)/graphene oxide foams with highly oriented and elongated cell structure via unidirectional foaming using supercritical carbon dioxide," *Industrial & Engineering Chemistry Research*, vol. 54, no. 2, pp. 758–768, 2015.
- [23] M. Treiser, S. Abramson, R. Langer, and J. Kohn, "Degradable and resorbable biomaterials," in *Biomaterials Science*, B. D. Ratner, A. S. Hoffman, F. J. Schoen, and J. E. Lemons, Eds., chapter I.2.6, pp. 179–195, 3rd edition, 2013.
- [24] O. Martin and L. Averous, "Poly(lactic acid): plasticization and properties of biodegradable multiphase systems," *Polymer*, vol. 42, no. 14, pp. 6209–6219, 2001.
- [25] P. Gupta, K. Vermani, and S. Garg, "Hydrogels: from controlled release to pH-responsive drug delivery," *Drug Discovery Today*, vol. 7, no. 10, pp. 569–579, 2002.
- [26] B. Y. Chen, Y. S. Wang, H. Y. Mi et al., "Effect of poly(ethylene glycol) on the properties and foaming behavior of macroporous poly(lactic acid)/sodium chloride scaffold," *Journal of Applied Polymer Science*, vol. 131, no. 23, pp. 205–212, 2014.
- [27] K. M. Nampoothiri, N. R. Nair, and R. P. John, "An overview of the recent developments in polylactide (PLA) research," *Bioresource Technology*, vol. 101, no. 22, pp. 8493–8501, 2010.
- [28] A. J. Nijenhuis, E. Colstee, D. W. Grijpma, and A. J. Pennings, "High molecular weight poly(L-lactide) and poly(ethylene oxide) blends: thermal characterization and physical properties," *Polymer*, vol. 37, no. 26, pp. 5849–5857, 1996.
- [29] A. M. Gajria, V. Davé, R. A. Gross, and S. P. McCarthy, "Miscibility and biodegradability of blends of poly(lactic acid) and poly(vinyl acetate)," *Polymer*, vol. 37, no. 3, pp. 437–444, 1996.
- [30] M. Sheth, R. A. Kumar, V. Davé, R. A. Gross, and S. P. McCarthy, "Biodegradable polymer blends of poly(lactic acid) and poly(ethylene glycol)," *Journal of Applied Polymer Science*, vol. 66, no. 8, pp. 1495–1505, 1997.
- [31] M. Keshtkar, M. Nofar, C. B. Park, and P. J. Carreau, "Extruded PLA/clay nanocomposite foams blown with supercritical CO<sub>2</sub>," *Polymer*, vol. 55, no. 16, pp. 4077–4090, 2014.
- [32] F. Mai, Y. Habibi, J.-M. Raquez et al., "Poly(lactic acid)/carbon nanotube nanocomposites with integrated degradation sensing," *Polymer*, vol. 54, no. 25, pp. 6818–6823, 2013.
- [33] E. Narimissa, R. K. Gupta, N. Kao, H. J. Choi, M. Jollands, and S. N. Bhattacharya, "Melt rheological investigation of polylactide-nanographite platelets biopolymer composites," *Polymer Engineering & Science*, vol. 54, no. 1, pp. 175–188, 2014.
- [34] B. Wang, T. Wan, and W. Zeng, "Rheological and thermal properties of polylactide/organic montmorillonite nanocomposites," *Journal of Applied Polymer Science*, vol. 125, no. 2, pp. E364–E371, 2012.
- [35] C. Miao and W. Y. Hamad, "Cellulose reinforced polymer composites and nanocomposites: a critical review," *Cellulose*, vol. 20, no. 5, pp. 2221–2262, 2013.
- [36] M. Luddee, S. Pivsa-Art, S. Sirisansaneeyakul, and C. Pechyen, "Particle size of ground bacterial cellulose affecting mechanical, thermal, and moisture barrier properties of PLA/BC biocomposites," *Energy Procedia*, vol. 56, pp. 211–218, 2014.
- [37] K. Issaadi, A. Habi, Y. Grohens, and I. Pillin, "Effect of the montmorillonite intercalant and anhydride maleic grafting on polylactic acid structure and properties," *Applied Clay Science*, vol. 107, pp. 62–69, 2015.
- [38] L. Zhang, Y. Li, H. Wang, Y. Qiao, J. Chen, and S. Cao, "Strong and ductile poly(lactic acid) nanocomposite films reinforced with alkylated graphene nanosheets," *Chemical Engineering Journal*, vol. 264, pp. 538–546, 2015.
- [39] A. M. Pinto, J. Cabral, D. A. P. Tanaka, A. M. Mendes, and F. D. Magalhães, "Effect of incorporation of graphene oxide and graphene nanoplatelets on mechanical and gas permeability properties of poly(lactic acid) films," *Polymer International*, vol. 62, no. 1, pp. 33–40, 2013.
- [40] B. S. Bouakaz, I. Pillin, A. Habi, and Y. Grohens, "Synergy between fillers in organomontmorillonite/graphene-PLA nanocomposites," *Applied Clay Science*, vol. 116–117, pp. 69–77, 2015.
- [41] R. Dimitriou, E. Jones, D. McGonagle, and P. V. Giannoudis, "Bone regeneration: current concepts and future directions," *BMC Medicine*, vol. 9, article 66, 2011.
- [42] M. L. Ferrone and C. P. Raut, "Modern surgical therapy: limb salvage and the role of amputation for extremity soft-tissue sarcomas," *Surgical Oncology Clinics of North America*, vol. 21, no. 2, pp. 201–213, 2012.
- [43] G. Martou and O. M. Antonyshyn, "Advances in surgical approaches to the upper facial skeleton," *Current Opinion in Otolaryngology & Head and Neck Surgery*, vol. 19, no. 4, pp. 242–247, 2011.
- [44] D. R. Sidell, T. Aghaloo, S. Tetradis et al., "Composite mandibulectomy: a novel animal model," *Otolaryngology—Head and Neck Surgery*, vol. 146, no. 6, pp. 932–937, 2012.
- [45] Y. Zhang, J. Wang, J. Wang et al., "Preparation of porous PLA/DBM composite biomaterials and experimental research of repair rabbit radius segmental bone defect," *Cell and Tissue Banking*, vol. 16, no. 4, pp. 615–622, 2015.
- [46] L. E. Claes, A. A. Ignatius, K. E. Rehm, and C. Scholz, "New bioresorbable pin for the reduction of small bony fragments: design, mechanical properties and in vitro degradation," *Biomaterials*, vol. 17, no. 16, pp. 1621–1626, 1996.
- [47] G. Schwach and M. Vert, "In vitro and in vivo degradation of lactic acid-based interference screws used in cruciate ligament reconstruction," *International Journal of Biological Macromolecules*, vol. 25, no. 1–3, pp. 283–291, 1999.

- [48] R. Suuronen, "Comparison of absorbable self-reinforced poly-L-lactide screws and metallic screws in the fixation of mandibular condyle osteotomies: an experimental study in sheep," *Journal of Oral and Maxillofacial Surgery*, vol. 49, no. 9, pp. 989–995, 1991.
- [49] A. R. Santos Jr., *Bioresorbable Polymers for Tissue Engineering*, INTECH Open Access Publisher, 2010.
- [50] R. P. F. Lanao, A. M. Jonker, J. G. C. Wolke, J. A. Jansen, J. C. M. van Hest, and S. C. G. Leeuwenburgh, "Physicochemical properties and applications of poly(lactic-co-glycolic acid) for use in bone regeneration," *Tissue Engineering Part B: Reviews*, vol. 19, no. 4, pp. 380–390, 2013.
- [51] J. Song, J. Xie, C. Li et al., "Near infrared spectroscopic (NIRS) analysis of drug-loading rate and particle size of risperidone microspheres by improved chemometric model," *International Journal of Pharmaceutics*, vol. 472, no. 1-2, pp. 296–303, 2014.
- [52] O. D. Schneider, S. Loher, T. J. Brunner et al., "Cotton wool-like nanocomposite biomaterials prepared by electrospinning: in vitro bioactivity and osteogenic differentiation of human mesenchymal stem cells," *Journal of Biomedical Materials Research Part B: Applied Biomaterials*, vol. 84, no. 2, pp. 350–362, 2008.
- [53] O. D. Schneider, D. Mohn, R. Fuhrer et al., "Biocompatibility and bone formation of flexible, cotton wool-like PLGA/calcium phosphate nanocomposites in sheep," *The Open Orthopaedics Journal*, vol. 5, pp. 63–71, 2011.
- [54] O. D. Schneider, F. Weber, T. J. Brunner et al., "In vivo and in vitro evaluation of flexible, cottonwool-like nanocomposites as bone substitute material for complex defects," *Acta Biomaterialia*, vol. 5, no. 5, pp. 1775–1784, 2009.
- [55] R. W. Bucholz, A. Carlton, and R. E. Holmes, "Hydroxyapatite and tricalcium phosphate bone graft substitutes," *The Orthopedic Clinics of North America*, vol. 18, no. 2, pp. 323–334, 1987.
- [56] C. A. Van Blitterswijk, J. J. Grote, W. Kuijpers, W. T. Daems, and K. De Groot, "Macropore tissue ingrowth: a quantitative and qualitative study on hydroxyapatite ceramic," *Biomaterials*, vol. 7, no. 2, pp. 137–143, 1986.
- [57] W. Suchanek and M. Yoshimura, "Processing and properties of hydroxyapatite-based biomaterials for use as hard tissue replacement implants," *Journal of Materials Research*, vol. 13, no. 1, pp. 94–117, 1998.
- [58] S. Hasegawa, S. Ishii, J. Tamura et al., "A 5-7 year in vivo study of high-strength hydroxyapatite/poly(L-lactide) composite rods for the internal fixation of bone fractures," *Biomaterials*, vol. 27, no. 8, pp. 1327–1332, 2006.
- [59] C. C. P. M. Verheyen, C. P. A. T. Klein, J. M. A. De Blicke-Hogervorst, J. G. C. Wolke, C. A. Van Blitterswijk, and K. De Groot, "Evaluation of hydroxyapatite/poly(L-lactide) composites: physico-chemical properties," *Journal of Materials Science: Materials in Medicine*, vol. 4, no. 1, pp. 58–65, 1993.
- [60] T. Furukawa, Y. Matsusue, T. Yasunaga et al., "Histomorphometric study on high-strength hydroxyapatite/poly(L-lactide) composite rods for internal fixation of bone fractures," *Journal of Biomedical Materials Research*, vol. 50, no. 3, pp. 410–419, 2000.
- [61] T. Yasunaga, Y. Matsusue, T. Furukawa, Y. Shikinami, M. Okuno, and T. Nakamura, "Bonding behavior of ultrahigh strength unsintered hydroxyapatite particles/poly(L-lactide) composites to surface of tibial cortex in rabbits," *Journal of Biomedical Materials Research*, vol. 47, no. 3, pp. 412–419, 1999.
- [62] S. Ishii, J. Tamura, T. Furukawa et al., "Long-term study of high-strength hydroxyapatite/poly(L-lactide) composite rods for the internal fixation of bone fractures: a 2–4-year follow-up study in rabbits," *Journal of Biomedical Materials Research Part B: Applied Biomaterials*, vol. 66, no. 2, pp. 539–547, 2003.
- [63] Y. Takeoka, M. Hayashi, N. Sugiyama, M. Yoshizawa-Fujita, M. Aizawa, and M. Rikukawa, "In situ preparation of poly(L-lactic acid-co-glycolic acid)/hydroxyapatite composites as artificial bone materials," *Polymer Journal*, vol. 47, no. 2, pp. 164–170, 2015.
- [64] W. Lu, K. Ji, J. Kirkham et al., "Bone tissue engineering by using a combination of polymer/Bioglass composites with human adipose-derived stem cells," *Cell and Tissue Research*, vol. 356, no. 1, pp. 97–107, 2014.
- [65] H. Li and J. Chang, "pH-compensation effect of bioactive inorganic fillers on the degradation of PLGA," *Composites Science and Technology*, vol. 65, no. 14, pp. 2226–2232, 2005.
- [66] V. Maquet, A. R. Boccaccini, L. Pravata, I. Notingher, and R. Jérôme, "Preparation, characterization, and in vitro degradation of bioresorbable and bioactive composites based on Bioglass-filled polylactide foams," *Journal of Biomedical Materials Research—Part A*, vol. 66, no. 2, pp. 335–346, 2003.
- [67] G. Vergnol, N. Ginsac, P. Rivory et al., "In vitro and in vivo evaluation of a polylactic acid-bioactive glass composite for bone fixation devices," *Journal of Biomedical Materials Research Part B: Applied Biomaterials*, vol. 104, no. 1, pp. 180–191, 2016.
- [68] N. Bakhshalian, H. Nowzari, K. M. Ahn, and B. H. Arjmandi, "Demineralized dentin matrix and bone graft: a review of literature," *The Journal of the Western Society of Periodontology/Periodontal Abstracts*, vol. 62, no. 2, pp. 35–38, 2014.
- [69] X. Qiao, S. J. Russell, X. Yang, G. Tronci, and D. J. Wood, "Compositional and in vitro evaluation of nonwoven type I collagen/poly-dl-lactic acid scaffolds for bone regeneration," *Journal of Functional Biomaterials*, vol. 6, no. 3, pp. 667–686, 2015.
- [70] H. Jo, M. Hong, J. B. Shim et al., "The role of demineralized bone particle in a PLGA scaffold designed to create a media equivalent for a tissue engineered blood vessel," *Macromolecular Research*, vol. 23, no. 11, pp. 986–993, 2015.
- [71] F. Yang, R. Murugan, S. Wang, and S. Ramakrishna, "Electrospinning of nano/micro scale poly(L-lactic acid) aligned fibers and their potential in neural tissue engineering," *Biomaterials*, vol. 26, no. 15, pp. 2603–2610, 2005.
- [72] Y. C. Shin, J. H. Lee, L. Jin et al., "Stimulated myoblast differentiation on graphene oxide-impregnated PLGA-collagen hybrid fibre matrices," *Journal of Nanobiotechnology*, vol. 13, article 21, 2015.
- [73] A. G. Mikos, A. J. Thorsen, L. A. Czerwonka et al., "Preparation and characterization of poly(L-lactic acid) foams," *Polymer*, vol. 35, no. 5, pp. 1068–1077, 1994.
- [74] M. Shin, H. Abukawa, M. J. Troulis, and J. P. Vacanti, "Development of a biodegradable scaffold with interconnected pores by heat fusion and its application to bone tissue engineering," *Journal of Biomedical Materials Research—Part A*, vol. 84, no. 3, pp. 702–709, 2008.
- [75] Y.-Y. Hsu, J. D. Gresser, D. J. Trantolo, C. M. Lyons, P. R. J. Gangadharam, and D. L. Wise, "Effect of polymer foam morphology and density on kinetics of in vitro controlled release of isoniazid from compressed foam matrices," *Journal of Biomedical Materials Research*, vol. 35, no. 1, pp. 107–116, 1997.
- [76] D. J. Mooney, D. F. Baldwin, N. P. Suh, J. P. Vacanti, and R. Langer, "Novel approach to fabricate porous sponges of poly(D,L-lactic-co-glycolic acid) without the use of organic solvents," *Biomaterials*, vol. 17, no. 14, pp. 1417–1422, 1996.

- [77] M. Ziabari, V. Mottaghitlab, and A. K. Haghi, "A new approach for optimization of electrospun nanofiber formation process," *Korean Journal of Chemical Engineering*, vol. 27, no. 1, pp. 340–354, 2010.
- [78] N. Ardjomandi, A. Henrich, J. Huth et al., "Coating of  $\beta$ -tricalcium phosphate scaffolds—a comparison between graphene oxide and poly-lactic-co-glycolic acid," *Biomedical Materials*, vol. 10, no. 4, Article ID 45018, 2015.
- [79] H. Haugen, J. Will, W. Fuchs, and E. Wintermantel, "A novel processing method for injection-molded polyether-urethane scaffolds. Part I: processing," *Journal of Biomedical Materials Research Part B: Applied Biomaterials*, vol. 77, no. 1, pp. 65–72, 2006.
- [80] J. Y. Kim, E. K. Park, S.-Y. Kim, J.-W. Shin, and D.-W. Cho, "Fabrication of a SFF-based three-dimensional scaffold using a precision deposition system in tissue engineering," *Journal of Micromechanics and Microengineering*, vol. 18, no. 5, Article ID 055027, 2008.
- [81] J.-H. Shim, J.-Y. Won, S.-J. Sung et al., "Comparative efficacies of a 3D-printed PCL/PLGA/ $\beta$ -TCP membrane and a titanium membrane for guided bone regeneration in beagle dogs," *Polymers*, vol. 7, no. 10, pp. 2061–2077, 2015.
- [82] S. M. Davachi, B. Kaffashi, A. Zamanian, B. Torabinejad, and Z. Ziaieirad, "Investigating composite systems based on poly l-lactide and poly l-lactide/triclosan nanoparticles for tissue engineering and medical applications," *Materials Science and Engineering C*, vol. 58, pp. 294–309, 2016.
- [83] M. Shafiq, Y. Jung, and S. H. Kim, "Stem cell recruitment, angiogenesis, and tissue regeneration in substance P-conjugated poly(l-lactide-co- $\epsilon$ -caprolactone) nonwoven meshes," *Journal of Biomedical Materials Research Part A*, vol. 103, no. 8, pp. 2673–2688, 2015.
- [84] Z. Yu, B. Yan, L. Gao et al., "Targeted delivery of bleomycin: a comprehensive anticancer review," *Current Cancer Drug Targets*, vol. 16, no. 6, pp. 509–521, 2016.
- [85] Z. Yu, Z. Cai, Q. Chen et al., "Engineering  $\beta$ -sheet peptide assemblies for biomedical applications," *Biomaterials Science*, vol. 4, no. 3, pp. 365–374, 2015.
- [86] Z. Yu, Q. Xu, C. Dong et al., "Self-assembling peptide nanofibrous hydrogel as a versatile drug delivery platform," *Current Pharmaceutical Design*, vol. 21, no. 29, pp. 4342–4354, 2015.
- [87] L. Cai, X. Wang, W. Wang et al., "Peptide ligand and PEG-mediated long-circulating liposome targeted to FGFR overexpressing tumor in vivo," *International Journal of Nanomedicine*, vol. 7, pp. 4499–4510, 2012.
- [88] H. Gao, Q. Zhang, Z. Yu, and Q. He, "Cell-penetrating peptide-based intelligent liposomal systems for enhanced drug delivery," *Current Pharmaceutical Biotechnology*, vol. 15, no. 3, pp. 210–219, 2014.
- [89] F. Masood, "Polymeric nanoparticles for targeted drug delivery system for cancer therapy," *Materials Science and Engineering C*, vol. 60, pp. 569–578, 2016.
- [90] H. Devalpally, D. Shenoy, S. Little, R. Langer, and M. Amiji, "Poly(ethylene oxide)-modified poly(beta-amino ester) nanoparticles as a pH-sensitive system for tumor-targeted delivery of hydrophobic drugs: part 3. Therapeutic efficacy and safety studies in ovarian cancer xenograft model," *Cancer Chemotherapy and Pharmacology*, vol. 59, no. 4, pp. 477–484, 2007.
- [91] L. L. Cai, N. Qiu, M. L. Xiang et al., "Improving aqueous solubility and antitumor effects by nanosized gambogic acid-mPEG<sub>2000</sub> micelles," *International Journal of Nanomedicine*, vol. 9, no. 1, pp. 243–255, 2013.
- [92] A. Kumari, S. K. Yadav, and S. C. Yadav, "Biodegradable polymeric nanoparticles based drug delivery systems," *Colloids and Surfaces B: Biointerfaces*, vol. 75, no. 1, pp. 1–18, 2010.
- [93] H. Fessi, F. Puisieux, J. P. Devissaguet, N. Ammoury, and S. Benita, "Nanocapsule formation by interfacial polymer deposition following solvent displacement," *International Journal of Pharmaceutics*, vol. 55, no. 1, pp. R1–R4, 1989.
- [94] C. P. Reis, R. J. Neufeld, A. J. Ribeiro, and F. Veiga, "Nanoencapsulation I. Methods for preparation of drug-loaded polymeric nanoparticles," *Nanomedicine: Nanotechnology, Biology, and Medicine*, vol. 2, no. 1, pp. 8–21, 2006.
- [95] J.-C. Leroux, E. Allémann, F. De Jaeghere, E. Doelker, and R. Gurny, "Biodegradable nanoparticles—from sustained release formulations to improved site specific drug delivery," *Journal of Controlled Release*, vol. 39, no. 2–3, pp. 339–350, 1996.
- [96] I. Fishbein, M. Chorny, L. Rabinovich, S. Banai, I. Gati, and G. Golomb, "Nanoparticulate delivery system of a tyroprostin for the treatment of restenosis," *Journal of Controlled Release*, vol. 65, no. 1–2, pp. 221–229, 2000.
- [97] J. Matsumoto, Y. Nakada, K. Sakurai, T. Nakamura, and Y. Takahashi, "Preparation of nanoparticles consisted of poly(L-lactide)-poly(ethylene glycol)-poly(L-lactide) and their evaluation in vitro," *International Journal of Pharmaceutics*, vol. 185, no. 1, pp. 93–101, 1999.
- [98] J. Xing, D. Zhang, and T. Tan, "Studies on the oridonin-loaded poly(D,L-lactic acid) nanoparticles in vitro and in vivo," *International Journal of Biological Macromolecules*, vol. 40, no. 2, pp. 153–158, 2007.
- [99] H. Gao, Y. N. Wang, Y. G. Fan, and J. B. Ma, "Synthesis of a biodegradable tadpole-shaped polymer via the coupling reaction of polylactide onto mono(6-(2-aminoethyl)amino-6-deoxy)- $\beta$ -cyclodextrin and its properties as the new carrier of protein delivery system," *Journal of Controlled Release*, vol. 107, no. 1, pp. 158–173, 2005.
- [100] E. Sánchez, M. Baro, I. Soriano, A. Perera, and C. Évora, "In vivo-in vitro study of biodegradable and osteointegrable gentamicin bone implants," *European Journal of Pharmaceutics and Biopharmaceutics*, vol. 52, no. 2, pp. 151–158, 2001.
- [101] T. Govender, S. Stolnik, M. C. Garnett, L. Illum, and S. S. Davis, "PLGA nanoparticles prepared by nanoprecipitation: drug loading and release studies of a water soluble drug," *Journal of Controlled Release*, vol. 57, no. 2, pp. 171–185, 1999.
- [102] D.-H. Kim and D. C. Martin, "Sustained release of dexamethasone from hydrophilic matrices using PLGA nanoparticles for neural drug delivery," *Biomaterials*, vol. 27, no. 15, pp. 3031–3037, 2006.
- [103] U. Bilati, E. Allémann, and E. Doelker, "Poly(D,L-lactide-co-glycolide) protein-loaded nanoparticles prepared by the double emulsion method—processing and formulation issues for enhanced entrapment efficiency," *Journal of Microencapsulation*, vol. 22, no. 2, pp. 205–214, 2005.
- [104] S. W. N. Ueng, L.-J. Yuan, N. Lee et al., "In vivo study of hot compressing molded 50:50 poly (DL-lactide-co-glycolide) antibiotic beads in rabbits," *Journal of Orthopaedic Research*, vol. 20, no. 4, pp. 654–661, 2002.
- [105] H. Song, W. Li, R. Qi et al., "Delivering a photosensitive transplatin prodrug to overcome cisplatin drug resistance," *Chemical Communications*, vol. 51, no. 57, pp. 11493–11495, 2015.

- [106] H. Otsuka, Y. Nagasaki, and K. Kataoka, "PEGylated nanoparticles for biological and pharmaceutical applications," *Advanced Drug Delivery Reviews*, vol. 55, no. 3, pp. 403–419, 2003.
- [107] T. Kissel, Y. Li, and F. Unger, "ABA-triblock copolymers from biodegradable polyester A-blocks and hydrophilic poly(ethylene oxide) B-blocks as a candidate for in situ forming hydrogel delivery systems for proteins," *Advanced Drug Delivery Reviews*, vol. 54, no. 1, pp. 99–134, 2002.
- [108] S. Fischer, E. Uetz-von Allmen, Y. Waeckerle-Men, M. Groettrup, H. P. Merkle, and B. Gander, "The preservation of phenotype and functionality of dendritic cells upon phagocytosis of polyelectrolyte-coated PLGA microparticles," *Biomaterials*, vol. 28, no. 6, pp. 994–1004, 2007.
- [109] E. Khodaverdi, F. S. M. Tekie, S. A. Mohajeri, F. Ganji, G. Zohuri, and F. Hadizadeh, "Preparation and investigation of sustained drug delivery systems using an injectable, thermosensitive, in situ forming hydrogel composed of PLGA-PEG-PLGA," *AAPS PharmSciTech*, vol. 13, no. 2, pp. 590–600, 2012.
- [110] S. Meyenburg, H. Lilie, S. Panzner, and R. Rudolph, "Fibrin encapsulated liposomes as protein delivery system: studies on the in vitro release behavior," *Journal of Controlled Release*, vol. 69, no. 1, pp. 159–168, 2000.
- [111] C. Yao, P. Yao, H. Wu, and Z. Zha, "Acceleration of wound healing in traumatic ulcers by absorbable collagen sponge containing recombinant basic fibroblast growth factor," *Biomedical Materials*, vol. 1, no. 1, pp. 33–37, 2006.
- [112] J. J. Wang, W. Z. Zhao, Z. X. Ren et al., "Recent advances of chitosan nanoparticles as drug carriers," *International Journal of Nanomedicine*, vol. 6, pp. 765–774, 2011.
- [113] V. K. Vishvakarma, K. Kumari, R. Patel, P. Singh, G. K. Mehrotra, and R. Chandra, "Gelatin Nanocomposites (GNCs): an efficient drug delivery system," in *Biomedical Applications of Natural Proteins*, D. Kumar and R. R. Kundapur, Eds., SpringerBriefs in Biochemistry and Molecular Biology, pp. 129–148, Springer, Berlin, Germany, 2015.
- [114] S. Lal and M. Datta, "In vitro prolonged gastric residence and sustained release of atenolol using novel clay polymer nanocomposite," *Applied Clay Science*, vol. 114, pp. 412–421, 2015.
- [115] R. C. Mundargi, V. R. Babu, V. Rangaswamy, P. Patel, and T. M. Aminabhavi, "Nano/micro technologies for delivering macromolecular therapeutics using poly(D,L-lactide-co-glycolide) and its derivatives," *Journal of Controlled Release*, vol. 125, no. 3, pp. 193–209, 2008.
- [116] B. Bittner, B. Ronneberger, R. Zange, C. Volland, J. M. Anderson, and T. Kissel, "Bovine serum albumin loaded poly(lactide-co-glycolide) microspheres: The influence of polymer purity on particle characteristics," *Journal of Microencapsulation*, vol. 15, no. 4, pp. 495–514, 1998.

## Research Article

# Effects of Organomontmorillonite Content on Morphology and Mechanical and Thermal Properties of Poly(2,6-dimethyl-1,4-phenylene oxide)/Polyamide-66 Nanocomposites

Kunxiao Yang,<sup>1</sup> Chunling Xin,<sup>1</sup> Ying Huang,<sup>1</sup> Lilong Jiang,<sup>1</sup> and Yadong He<sup>1,2</sup>

<sup>1</sup>College of Mechanical and Electrical Engineering, Beijing University of Chemical Technology, Beijing 100029, China

<sup>2</sup>The Engineering Research Center of Polymer Processing Equipment, Ministry of Education, Beijing 100029, China

Correspondence should be addressed to Yadong He; heyd@mail.buct.edu.cn

Received 9 August 2016; Accepted 18 September 2016

Academic Editor: Xiao Gong

Copyright © 2016 Kunxiao Yang et al. This is an open access article distributed under the Creative Commons Attribution License, which permits unrestricted use, distribution, and reproduction in any medium, provided the original work is properly cited.

The nanocomposites consisting of polymer matrix and nanofiller have attracted great attention because of the improved physical properties. In this paper, organomontmorillonite (OMMT) was introduced into poly(2,6-dimethyl-1,4-phenylene oxide) grafted maleic anhydride (PPO-g-MA) compatibilized poly(2,6-dimethyl-1,4-phenylene oxide)/polyamide-66 (PPO/PA66) blends by melt extrusion. The morphology of PPO/PA66 nanocomposites with different amounts of OMMT was investigated using transmission electron microscopy (TEM), wide-angle X-ray diffraction (WAXD), and scanning electron microscopy (SEM). The OMMT platelets exhibited an exfoliated structure in the PA66 matrix and an intercalated structure on the surface of PPO domains at low OMMT loading (2 phr). However, the exfoliated platelets in matrix were found to transform into intercalated stacks by adding 6 phr of OMMT. The mechanical properties and thermal stability were significantly improved with the coexistence of exfoliated and intercalated OMMT at low OMMT loading (2–4 phr). The exfoliated OMMT platelets imposed a confinement effect on the macromolecular chains and thereby increased the storage modulus and complex viscosity of nanocomposites.

## 1. Introduction

Polymer/layered silicate nanocomposites have attracted great attention because of their ability to improve thermal stability and mechanical properties [1–5]. Organomontmorillonite (OMMT) is reported to be efficient in modifying the morphology of multiphase blends. Li et al. found that the selective localization of organ clays in the PA6 phase can change the viscosity ratio of multiphase polymer blends and prevent the coalescence of dispersed domains [6–8]. Since OMMT is a layered filler, separating the layer into intercalated or exfoliated structures is vital for property improvement [9, 10]. Moreover, the shape of nanoparticles shows a significant effect on the rheology and strength of nanocomposites [11, 12]. The microstructure of nanocomposites, especially for multiphase blends, depends drastically on the surface modification of filler and presence of compatibilizer. Therefore,

functional groups are utilized to modify the surface of montmorillonite for higher layer spacing [13, 14].

In this study, OMMT is introduced to improve the mechanical and thermal properties of poly(2,6-dimethyl-1,4-phenylene oxide)/polyamide-66 (PPO/PA66) blends. The PPO/PA66 blends inherit the high chemical resistance and processability of PA66 and maintain the dimensional stability and good thermal properties of PPO. However, PPO/PA66 blends are restricted by high immiscibility due to the high interfacial tensions and the large differences in polymer polarities [15–19]. The properties of PPO/PA66 blends are strongly decided by the morphology and interfacial adhesion. However, the high viscosity ratio and incompatibility endow PPO/PA66 blends with poor mechanical properties with the absence of additives. Reactive compatibilization is an efficient way to strengthen interaction between components and to obtain blends or composites with desirable properties [20, 21].

PA66/PPO blends with smaller particle size and better mechanical properties could be prepared with the addition of copolymers containing maleic anhydride (MA) or glycidyl methacrylate (GMA) [22–26]. Moreover, the rigidity of both components necessitates the introduction of elastomers and rubbers into PPO/PA blends, such as styrene-butylstyrene block copolymer (SBS), styrene-ethylene-butylstyrene block copolymer (SEBS), and ethylene-propylene-diene terpolymer (EPDM) [27, 28]. Unfortunately, the toughened blends are restricted by low strength and low thermal stability, which are undesirable for engineering application [29–31].

In this work, PPO/PA66/OMMT nanocomposites were prepared with PPO grafted with MA (PPO-g-MA) serving as a compatibilizer and SEBS as an impact modifier. The relationship between OMMT loading and its microstructure was investigated via wide-angle X-ray diffraction and transmission electron microscope. The effects of compatibilizer on morphological structure of nanocomposites were further discussed. The main objectives of this study were to investigate the effects of OMMT dispersion on phase morphology, mechanical properties, thermal stability, and rheological properties of PPO/PA66/OMMT nanocomposites.

## 2. Experimental

**2.1. Materials.** PPO (LXR45) and PA66 (EPR27) were purchased from Shenma Industrial Co. and China National Bluestar Co., respectively. SEBS (Kraton G1651) was made by Shell Chemical Co., which contains 29 wt% styrene and number-averaged molecular weight of 29,000 in the PS blocks and 116,000 in the EB block. MA and dicumyl peroxide (DCP) (analytical grade reagents) were supplied by Beijing Chemical Industry Group Co. Organomontmorillonite (Nanocor I.34 TCN, density 52.00 g/cm<sup>3</sup>) was modified with methyl dihydroxyethyl hydrogenated tallow ammonium.

**2.2. Sample Preparation.** PPO was grafted with MA as compatibilizer via reactive melt extrusion. Briefly, powders of PPO, MA, and DCP were premixed at a ratio of 100/2/0.1 in a homogenizer at 70 °C for 10 min. The mixture was extruded by a Coperion twin-screw extruder (ZSK 26 Mc) at 180/260/270/290/290/290/290/280 °C and a screw speed of 120 rpm. This graft reaction was studied by Fourier transform infrared spectrometry (FTIR) analysis and titration analysis. The grafted MA content in PPO-g-MA was about 0.5–0.6 wt%.

All the materials were dried at 80 °C for 12 h and premixed for 5 min before extrusion. The melt compounding was carried out on a self-designed triangle with a screw diameter of 35.2 mm and a length-diameter ratio ( $L/D$ ) of 28. The screw speed was maintained at 200 rpm and the barrel temperature was 240–285 °C. Moreover, the compatibilized ternary blend (PPO/PPO-g-MA/PA66/SEBS = 25/25/50/5; marked as T) and nanocomposites with different OMMT contents (PPO/PPO-g-MA/PA66/SEBS/OMMT = 25/25/50/5/ $x$ ; marked as N- $x$ ) were prepared for comparison. The extruded blends or nanocomposites were dried in a vacuum oven at 80 °C for 8 h and then molded into standard specimens by

a HAITIAN SA900/260 injection molding machine, which operated at the barrel temperature of 270/280/285/290/280 °C and injection pressure of 60 MPa.

**2.3. Characterization.** Pure OMMT, N-2, N-4, and N-6 were characterized on an Empyrean wide-angle X-ray diffractometer (WAXD; PANalytical, Netherlands) at  $\lambda = 0.154$  nm, 4 kW,  $2\theta = 1$ –30°. The scanning speed was 5°/min with a step of 0.025°.

The dispersion of OMMT in blends was investigated using a Hitachi H-800 transmission electron microscope (TEM) at an accelerating voltage of 200 kV. The nanocomposites were ultramicrotomed to ~100 nm thick samples using a LECIA EMUC7. The samples were stained by osmium tetroxide (OsO<sub>4</sub>) for 30 min.

The morphology was observed under a Quanta 250 FEG scanning electron microscope (SEM). All the injected samples were kept in liquid nitrogen for some time and brittle-fractured. The surfaces were etched in chloroform over 8 h for selective dissolution of PPO. Moreover, some of the samples were etched with boiled n-hexane for 3 h for removal of SEBS phase. The etched surfaces were kept in vacuum at 80 °C for 8 h and then gold-coated before observation. The number-averaged particle diameter  $\overline{D}_n$  and volume average particle size  $\overline{D}_v$  of the dispersed phase were analyzed with an image analyzer (*Image J 1.41*) and calculated according to the following:

$$\overline{D}_n = \frac{\sum N_i D_i}{\sum N_i}, \quad (1)$$

$$\overline{D}_v = \frac{\sum N_i D_i^4}{\sum N_i D_i^3},$$

where  $N_i$  is the number of particles with diameter  $D_i$ . The number of particles in this study was 300–400 per sample.

Notched impact strengths (ISO-179-2010) were measured using a pendulum impact tester (ZBC 1400-2, Shenzhen Sans Co.) at room temperature, and the impact energy was 4 J. The tensile (ISO-8256-2005) and flexural (ISO-178-2010) properties were measured with a universal testing instrument (XWW, Chengde Jinjian Co.) at a crosshead speed of 50 mm/min and 2 mm/min, respectively.

Dynamic mechanical thermal properties of nanocomposites were investigated using a DMA 242 (Netzsch, Germany), with a specimen dimension of 16 × 12 × 5 mm<sup>3</sup>. The sample was heated from –20 °C to 250 °C at a heating rate of 3 °C/min. A frequency of 1 Hz was used after optimization of the static and dynamic forces.

Thermogravimetric analysis (TGA) was performed under nitrogen flow from 40 to 800 °C with heating rate of 10 °C/min by using a TA TGA Q50 thermal analyzer.

Dynamic rheological properties of nanocomposites were determined with a HAAKE MARS-III rotational rheometer (parallel-plate geometry; diameter = 20 mm; gap = 1 mm) in a nitrogen environment. Frequency sweeping was performed at 280 °C at a frequency range of 0.01–100 s<sup>–1</sup>, with a strain of 1%.

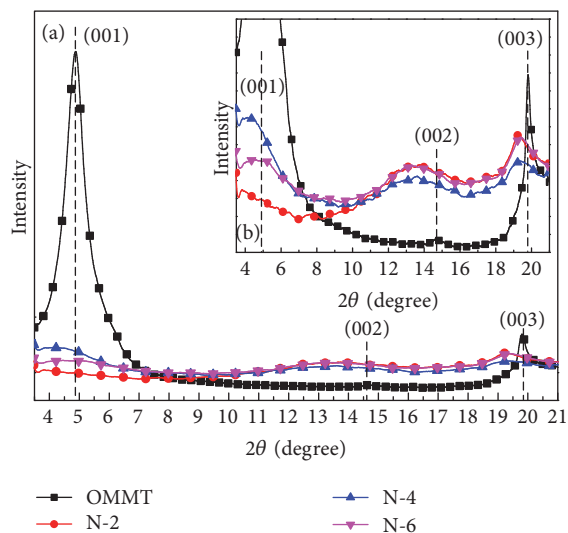


FIGURE 1: WAXD patterns of OMMT and nanocomposites N-2, N-4, and N-6: (a) original patterns; (b) magnified patterns.

### 3. Results and Discussion

**3.1. Dispersion of OMMT in PPO/PA66.** The location and dispersion of OMMT in multiphase blends are vital for property improvement of nanocomposites. The exfoliation and microstructure of OMMT in PPO/PA66 blends were investigated via WAXD and TEM.

WAXD patterns of OMMT and its nanocomposites are shown in Figure 1. The peak (001) and its higher order diffractions, for example, (002) and (003), of pure OMMT (dashed line in Figure 1) are at  $2\theta = 4.91, 14.67, 19.80^\circ$ , respectively, which correspond to basal spacing of 1.80, 0.60 and 0.44 nm, respectively, according to Bragg's law ( $\lambda = 2d \sin \theta$ , where  $d$  is the layer spacing;  $\lambda$  is the X-ray wavelength). Compared with pure OMMT, the (001) peaks of nanocomposites N-2, N-4, and N-6 all shift leftward to a lower angle (about  $4^\circ$ ), while the corresponding  $d$  increases to 2.2 nm. For each nanocomposite,  $d$  of the (002) and (003) peaks increases to 0.65 nm ( $2\theta = 13.73^\circ$ ) and 0.46 nm ( $2\theta = 19.25^\circ$ ), respectively. It is indicated that some molecular chains are intercalated between the stacked OMMT layers, so intercalated composites are obtained. These phenomena are attributed to the strong affinity between the anhydride group and OMMT surface and/or the hydroxyl groups of PPO and the ammonium surfactant [32–34]. Furthermore, this result may be caused by the separation of OMMT galleries under the shear flow of extruder. However, the gallery spacing is reduced with the increase of OMMT concentration. For N-6, a broad (001) peak appears around  $4.5^\circ$ , corresponding to 1.91 nm. The reason is that the polymer-OMMT interactions at high clay concentration are dominated by the van der Waals force, which limits the expansion of OMMT galleries [9]. Meanwhile, the preservation of the three diffraction peaks indicates that a significant amount of OMMT remained in the layered form after melt extrusion.

To further explore the dispersion of OMMT and the microstructure of nanocomposites, we investigated the morphologies of N-2, N-4, and N-6 using TEM (Figure 2). The dark line is the stack of OMMT platelet and the dark part with small domains is the PPO phase, while the matrix is the PA66 phase. At the loading of 2 phr of OMMT, it is noteworthy that silicates are located at both the PA66 matrix and the PPO-PA66 interfaces. In the PA66 matrix, OMMT shows a disruption of platelet with a uniform platelet separation. This indicates an exfoliated structure of OMMT platelets. Moreover, the platelets exhibit an intercalated structure on the surface of PPO/PA66 blends. These results suggest that the intercalated structure and the exfoliated structure coexist and are selectively located in nanocomposites (Figure 3). With PPO-g-MA as the compatibilizer, the strong affinity between MA group and OMMT surface makes the intercalated silicates locate at the PPO-PA66 interfaces [32, 33]. Due to the barrier effect of the interfacial platelets, the OMMT could effectively prevent the coalescence of dispersion.

When the OMMT loading increases to 4 phr, a similar dispersion of OMMT was observed, and a bit of small stacks appeared in the PA66 matrix. This phenomenon indicated that the surface of the PPO droplets was saturated with the OMMT platelets. At high OMMT concentration (N-6), the number of stacks in the matrix increased apparently. The exfoliated OMMT platelets were found to transform into intercalated stacks in PA66 matrix. These agglomerates of OMMT could cause premature fracture in mechanical test which is discussed in Section 3.2.

**3.2. Morphology of the Nanocomposites.** Figure 4 illustrates the morphologies of the etched fracture surfaces of PPO/PA66 blend and its nanocomposites. The black domains indicate the extracted PPO phase. With PPO-g-MA as an effective compatibilizer, the interfaces between PPO and PA66 in blend T are vague and uneven. Nevertheless, the PPO domain has a wide particle size distribution, which is attributed to the high viscosity ratio of PPO/PA66. Compared with blend T ( $D_n = 0.79 \mu\text{m}$ ), the nanocomposites N-2, N-4, and N-6 show smaller PPO domains (0.65, 0.61, and 0.69  $\mu\text{m}$ , resp.). However, the PPO domain size is not significantly affected by the increase of OMMT loading.

These phenomena are attributed to the variation of OMMT distribution and location on the morphology of PPO/PA66 blends. As OMMT exhibited exfoliated structure in the PA66 matrix, the viscosity ratio of PPO/PA66 decreases significantly, which is beneficial for the breakdown of dispersed droplets [32]. Moreover, the interfacial presence of intercalated OMMT exerts a barrier effect (Figure 3), which prevents the coalescence of PPO domains. As for nanocomposite N-6, the thick OMMT stacks play a limiting role in preventing the coalescence of dispersion, so the domain size of PPO increases at high OMMT loading.

**3.3. Mechanical Properties.** The mechanical properties of polymer blends are dominated by their morphological structures. The relationship between notched impact strengths and particle size with increasing OMMT content is shown in Figure 5. The impact strength of nanocomposites is first

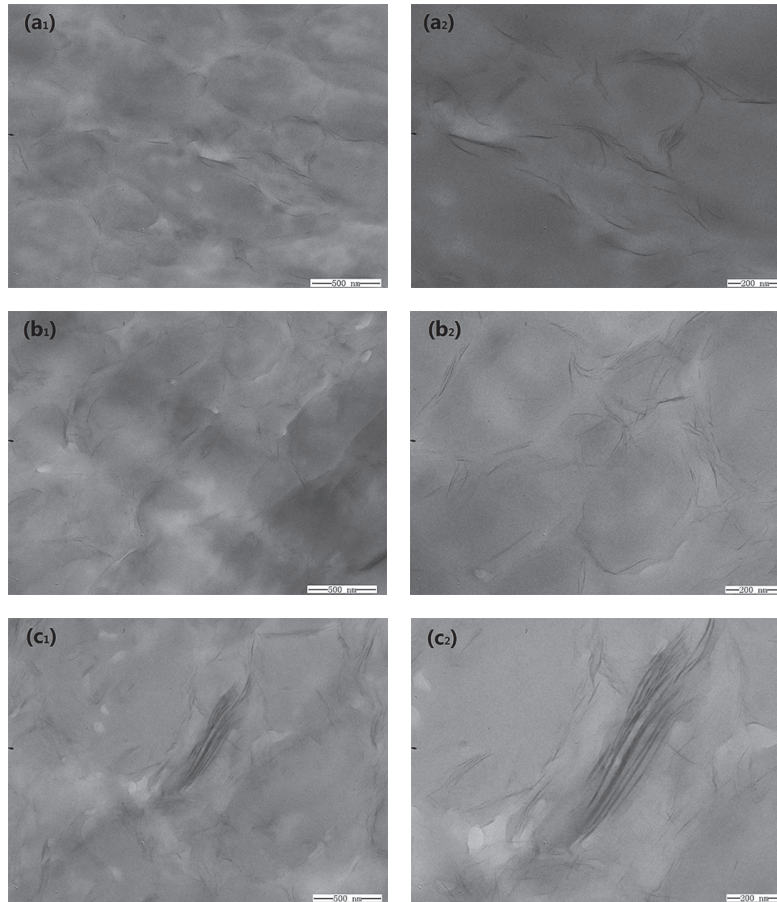


FIGURE 2: TEM micrographs of PPO/PA66 nanocomposites: (a<sub>1</sub>) N-2; (a<sub>2</sub>) high magnification of (a<sub>1</sub>); (b<sub>1</sub>) N-4; (b<sub>2</sub>) high magnification of (b<sub>1</sub>); (c<sub>1</sub>) N-6; (c<sub>2</sub>) high magnification of (c<sub>1</sub>).

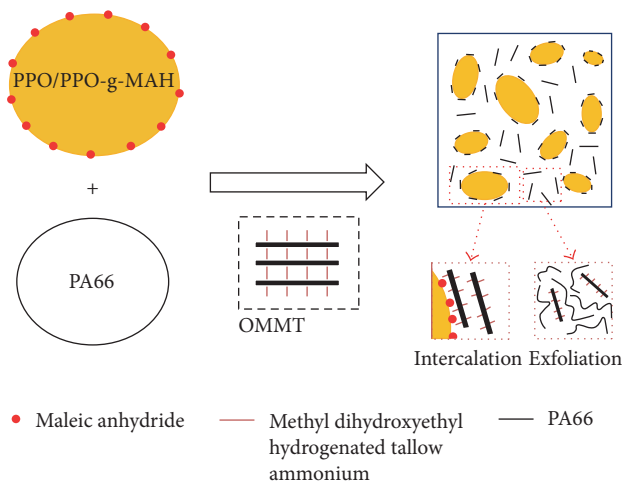


FIGURE 3: Schematic diagram for dispersion of OMMT in PPO/PA66 nanocomposite.

improved and then weakened dramatically with the increase of OMMT content. This phenomenon is attributed to the changes of OMMT morphology and droplet diameter, by

which the smaller particle size could significantly enhance the multiphase interaction and reduce the stress concentration in blends. Nevertheless, with the increase of OMMT loading (N-6), the appearance of OMMT stacks in the PA66 matrix aggravates the stress concentration which would accelerate the fracture in impact test.

As shown in Figure 6, both tensile strength and flexural strength are sharply improved with the addition of OMMT. This improvement is due to the exfoliated OMMT which increases the rigidity of the PA matrix. However, the tensile strength of nanocomposites decreased dramatically at high OMMT loading. The reason is that the presence of OMMT stacks in PA66 matrix would induce defects during tensile tests, resulting in the decrease of tensile strength. These phenomena illustrate that the dispersion of OMMT significantly affects the mechanical properties.

For modification of PPO/PA66 blends, it is difficult to keep a balance between the toughness and strength of the immiscible system. In this study, the impact strength, tensile strength, and flexural strength of PPO/PA66 composites are all significantly improved with an appropriate addition of OMMT. To further explore the effect of OMMT morphology on mechanical properties improvement, we observed the morphology of brittle-fractured surfaces of N-2 etched by

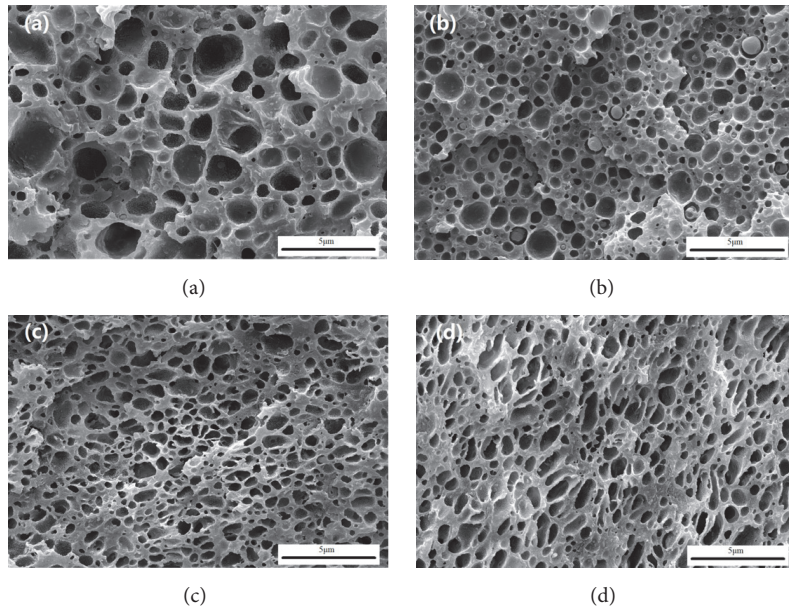


FIGURE 4: SEM micrographs of PPO/PA66 blends and nanocomposites: (a) T; (b) N-2; (c) N-4; (d) N-6.

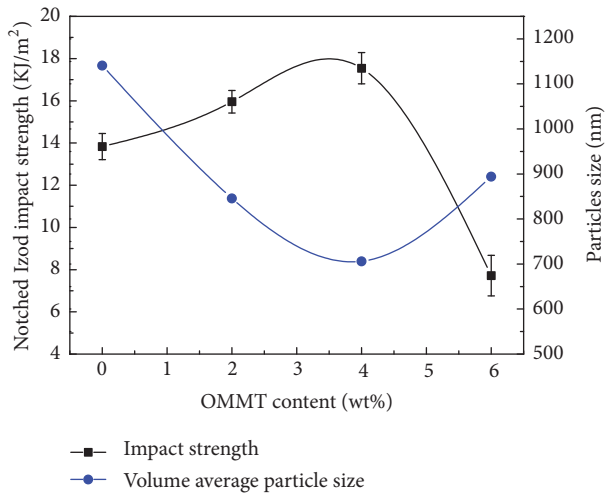


FIGURE 5: The relation of notched impact strengths and particle size for PPO/PA66 nanocomposites.

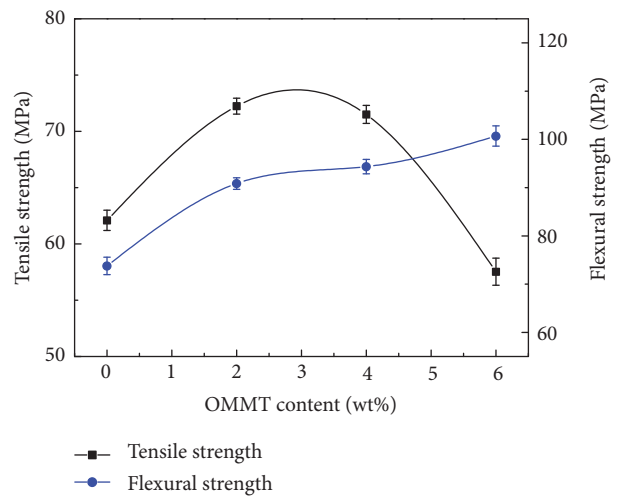


FIGURE 6: Tensile strengths and flexural strengths of PPO/PA66 nanocomposites with addition of OMMT.

n-hexane, which could selectively remove the SEBS phase. As shown in Figure 7, SEBS is mainly located in the PPO phase, which is ascribed to the high compatibility between PS block and PPO. According to a previous study, the PPO/SEBS (90/10) blend has excellent impact strength of 33.5 KJ/m<sup>2</sup>, which indicates that the dispersed domains act as toughened particles in toughening of PA66 matrix. Meanwhile, the polar OMMT is highly affinitive to both polar PA66 and the MA group in the PPO phase [7, 32]. Thus, the intercalated OMMT at the PPO-PA66 interface could enhance the interfacial adhesion and reduce the phase separation, thereby improving the impact strength. Furthermore, the exfoliated OMMT leads to a confinement effect to PA66 chains, which

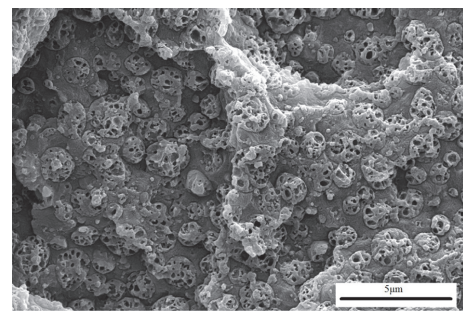


FIGURE 7: SEM micrographs of brittle-fractured surfaces of nanocomposite N-2 etched by n-hexane.

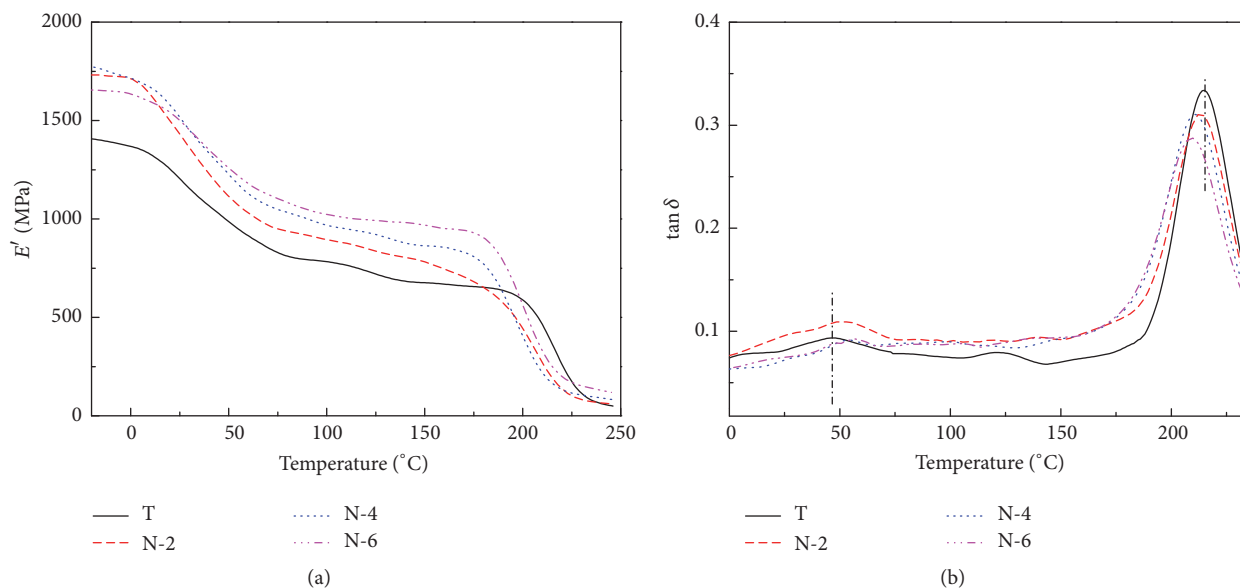


FIGURE 8: (a) Storage modulus ( $E'$ ) and (b) loss factor ( $\tan \delta$ ) patterns of DMTA for PPO/PA66 blends and nanocomposites.

TABLE 1: The data of DMTA for PPO/PA66 blend and nanocomposites.

Sample	$E'$ (Mpa, 0°C)	$E'$ (Mpa, 150°C)	$T_g$ (°C)	
			PA66	PPO
T	1368.6	675.8	48.4	222.8
N-2	1712.8	781.8	51.8	213.4
N-4	1714.7	863.9	53.6	210.6
N-6	1635.1	968.6	52.2	209.4

enhances the rigidity of PA matrix. Therefore, the synergistic effect between the intercalated structure and the exfoliated structure in nanocomposites could efficiently improve both toughness and strength.

**3.4. Thermal Properties.** The effect of OMMT on nanocomposite was investigated through dynamic mechanical thermal analysis (DMTA) and thermogravimetric analysis. Figure 8(a) illustrates the temperature dependence of storage modulus ( $E'$ ) for PPO/PA66 blends and nanocomposites. Two distinct decreases of  $E'$  occur with the temperature rise, corresponding to the chain segment relaxation of PA66 and PPO, respectively. The nanocomposites exhibit significantly higher  $E'$  than PPO/PA66 blends over the test temperature range ( $-20$  to  $+250^\circ\text{C}$ ) (Table 1). This result indicates that the addition of OMMT reinforces both PA66 and PPO phases, as the exfoliated and intercalated OMMT platelets impose a significant constraint on the mobility of the PA66 and PPO chain segments. However,  $E'$  of nanocomposite N-6 is lower than those of N-2 and N-4 in the low temperature region, indicating a decrease in rigidity of PA66 phase. It proves that the presence of OMMT agglomerates induces defects in PA66 matrix.

TABLE 2: Thermal data of PPO/PA66 blend and nanocomposites.

Sample	$T_{\text{onset (5\%)}}$ (°C)	$T_{\text{max}}$ (°C)	Residue at 600°C (wt%)
T	452.8	391.6	1.71
N-2	455.8	397.5	7.75
N-4	457.5	396.8	9.78
N-6	459.8	400.6	11.56

The loss factors ( $\tan \delta$ ) of PPO/PA66 blends and nanocomposites are shown in Figure 8(b). All samples have two major peaks corresponding to the glass transition temperatures ( $T_g$ ) of PA66 and PPO phases, respectively. The peaks shift towards each other with the increase of OMMT loading, which implies the improved compatibility between the two phases. It is indicated that the higher OMMT loadings of nanocomposites generate a higher volume of constrained polymers, despite the greater exfoliation in lower-OMMT samples.

The TGA data were analyzed to determine if the thermal stability and thermal degradation were influenced by the dispersion of OMMT. As shown in Figure 9, the addition of OMMT is favorable for thermal properties of PPO/PA66/OMMT nanocomposites. The presence of OMMT resists against the destructive effect of high temperature on macromolecular chains. Moreover, the thermal stability of nanocomposites is improved gradually with the increase of OMMT loading, which implies the type of dispersion has no significant effect on the thermal properties. Some representative TGA data are listed in Table 2.

**3.5. Rheological Properties.** The storage modulus ( $G'$ ) and complex viscosity ( $\eta^*$ ) of PPO/PA66 blend and its nanocomposites against the shear rate are shown in Figure 10. For

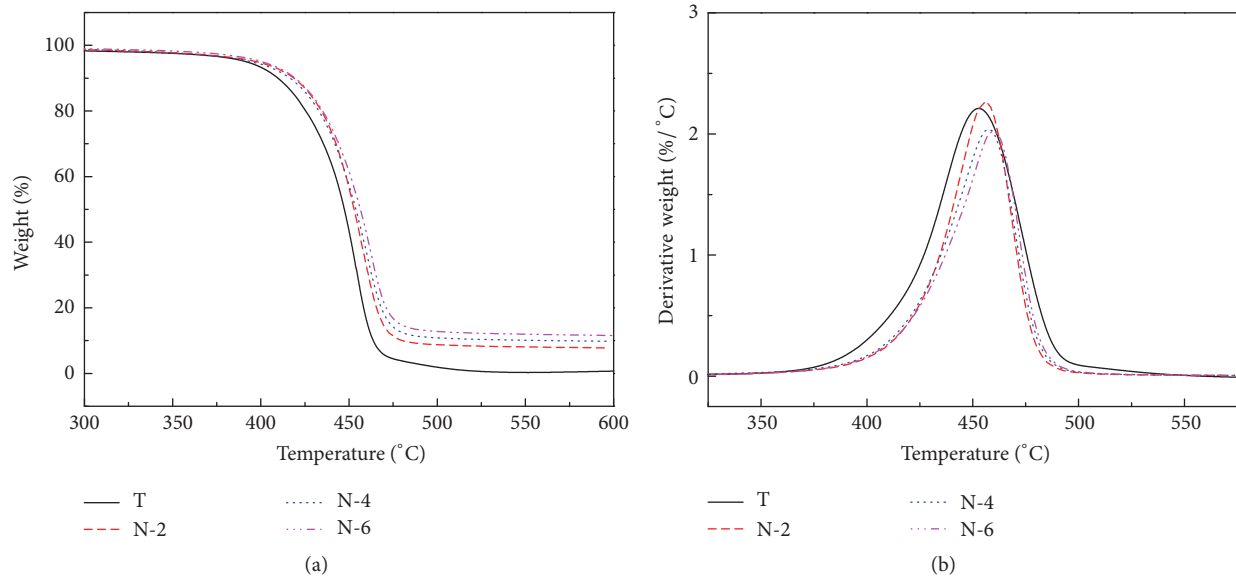


FIGURE 9: (a) TGA decomposition and (b) derivative TGA curves of PPO/PA66 blends and nanocomposites.

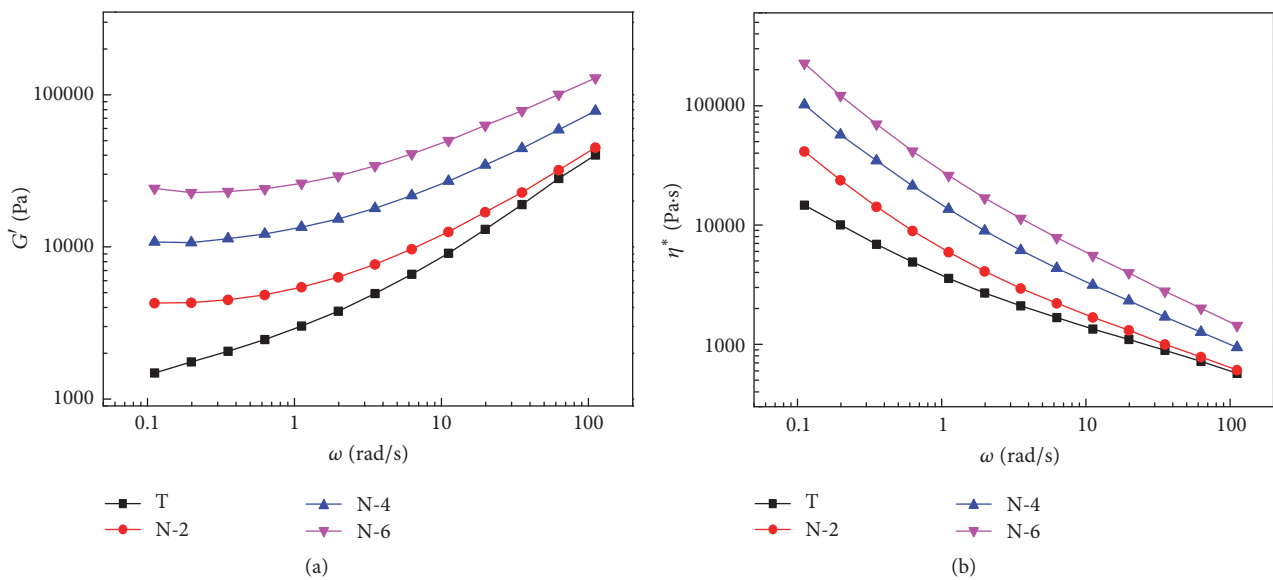


FIGURE 10: (a) Storage modulus ( $G'$ ) and (b) complex viscosity ( $\eta^*$ ) patterns of PPO/PA66 blends and nanocomposites.

PPO/PA66 blends,  $G'$  and  $\eta^*$  both are increased with the addition of OMMT, especially at low frequencies. Generally, the higher  $G'$  and  $\eta^*$  correspond to a slower relaxation of the macromolecular chains, which is consistent with the analysis of thermal mechanical properties. The exfoliation of OMMT platelets could change the microstructure of nanocomposites, leading to a sensitive response in the dynamic rheological behavior. Moreover, the viscosity of N-2 is nearly overlapped with that of the OMMT-free sample T at high shear rate, which could significantly improve the mechanical properties. It means that PPO/PA66 blends with the coexistence of exfoliated and intercalated OMMT could maintain both mechanical properties and processability.

#### 4. Conclusions

OMMT was introduced into PPO/PA66 blend to prepare nanocomposites with excellent mechanical properties by simple melt compounding. Under appropriate loading (2, 4 phr), OMMT shows an exfoliated structure in PA66 matrix and an intercalated structure at the PPO-PA66 interfaces with the presence of PPO-g-MA. This special microstructure lessens the dispersed particle diameter and improves the interfacial adhesion, thus significantly enhancing both toughness and strength. At high OMMT loading (6 phr), the presence of OMMT agglomerates limits the mechanical properties of PPO/PA66 composites. The addition of OMMT

also improves the thermal mechanical properties and thermal stability, thus expanding the engineering application of the nanocomposites. The homogeneous exfoliated or intercalated structure of OMMT significantly constrains the mobility of both PA66 and PPO chain segments, thus increasing the viscosity of nanocomposites. Overall, since the comprehensive properties of PPO/PA66/OMMT nanocomposites are significantly improved with the addition of OMMT, the optimum content of OMMT is 2 to 4 phr.

## Competing Interests

The authors declare that the received funding from National Natural Science Foundation of China leads to no conflict of interests regarding the publication of this paper.

## Acknowledgments

The authors gratefully acknowledge the support from the National Natural Science Foundation of China (Project no. 51273019).

## References

- [1] B. Han, G. Ji, S. Wu, and J. Shen, "Preparation and characterization of nylon 66/montmorillonite nanocomposites with co-treated montmorillonites," *European Polymer Journal*, vol. 39, no. 8, pp. 1641–1646, 2003.
- [2] R. Gallego, D. García-López, J. C. Merino, and J. M. Pastor, "The effect of montmorillonite and compatibilizer quantities on stiffness and toughness of polyamide nanoblends," *Polymer International*, vol. 59, no. 4, pp. 472–478, 2010.
- [3] Y. Wu, Y. Shi, L. Zhu, B. Shentu, and Z. Weng, "Joint effect of compatibilizer and organo-montmorillonite on compatibilization of polyamide-6/poly(phenylene oxide) blend: morphology and properties," *Polymer-Plastics Technology and Engineering*, vol. 54, no. 7, pp. 682–690, 2015.
- [4] Kusmono, Z. A. Mohd Ishak, W. S. Chow, T. Takeichi, and Rochmadi, "Compatibilizing effect of SEBS-g-MA on the mechanical properties of different types of OMMT filled polyamide 6/polypropylene nanocomposites," *Composites Part A: Applied Science and Manufacturing*, vol. 39, no. 12, pp. 1802–1814, 2008.
- [5] X. Gong, Y. Bao, C. Qiu, and C. Jiang, "Individual nanostructured materials: fabrication and surface-enhanced Raman scattering," *Chemical Communications*, vol. 48, no. 56, pp. 7003–7018, 2012.
- [6] M. Sabard, F. Gouanvé, E. Espuche et al., "Influence of montmorillonite and film processing conditions on the morphology of polyamide 6: effect on ethanol and toluene barrier properties," *Journal of Membrane Science*, vol. 450, pp. 487–498, 2014.
- [7] Y. Li and H. Shimizu, "Novel morphologies of poly(phenylene oxide) (PPO)/polyamide 6 (PA6) blend nanocomposites," *Polymer*, vol. 45, no. 22, pp. 7381–7388, 2004.
- [8] Y. Li and H. Shimizu, "Co-continuous polyamide 6 (PA6)/Acrylonitrile-Butadiene-Styrene (ABS) nanocomposites," *Macromolecular Rapid Communications*, vol. 26, no. 9, pp. 710–715, 2005.
- [9] A. Ranade, N. A. D'Souza, and B. Gnade, "Exfoliated and intercalated polyamide-imide nanocomposites with montmorillonite," *Polymer*, vol. 43, no. 13, pp. 3759–3766, 2002.
- [10] M. Motovilin, Z. Denchev, and N. Dencheva, "On the structure-properties relationship in montmorillonite-filled polyamide 6 nanocomposites," *Journal of Applied Polymer Science*, vol. 120, no. 6, pp. 3304–3315, 2011.
- [11] S. T. Knauert, J. F. Douglas, and F. W. Starr, "The effect of nanoparticle shape on polymer-nanocomposite rheology and tensile strength," *Journal of Polymer Science, Part B: Polymer Physics*, vol. 45, no. 14, pp. 1882–1897, 2007.
- [12] T. Xu and V. A. Davis, "Liquid crystalline phase behavior of silica nanorods in dimethyl sulfoxide and water," *Langmuir*, vol. 30, no. 16, pp. 4806–4813, 2014.
- [13] X. Kornmann, H. Lindberg, and L. A. Berglund, "Synthesis of epoxy-clay nanocomposites: influence of the nature of the clay on structure," *Polymer*, vol. 42, no. 4, pp. 1303–1310, 2001.
- [14] L. Zhang, X. Gong, Y. Bao et al., "Electrospun nanofibrous membranes surface-decorated with silver nanoparticles as flexible and active/sensitive substrates for surface-enhanced Raman scattering," *Langmuir*, vol. 28, no. 40, pp. 14433–14440, 2012.
- [15] Y. L. Li, T. X. Xie, and G. S. Yang, "Effects of polyphenylene oxide content on morphology, thermal, and mechanical properties of polyphenylene oxide/polyamide 6 blends," *Journal of Applied Polymer Science*, vol. 99, no. 5, pp. 2076–2081, 2006.
- [16] A. Liu, T. Xie, and G. Yang, "Effect of Na<sup>+</sup>-MMT platelets on monomer casting polyamide 6/polyphenylene oxide blends," *Macromolecular Chemistry and Physics*, vol. 207, no. 23, pp. 2180–2187, 2006.
- [17] J. E. Puskas, Y. Kwon, V. Altstädt, and M. Kontopoulou, "Blends of poly(2,6-dimethyl-1,4-phenylene oxide) (PPO) with polystyrene-based thermoplastic rubbers: a comparative study," *Polymer*, vol. 48, no. 2, pp. 590–597, 2007.
- [18] S. C. Jana, N. Patel, and D. Dharaiya, "Compatibilization of PBT-PPE blends using low molecular weight epoxy," *Polymer*, vol. 42, no. 21, pp. 8681–8693, 2001.
- [19] R. T. Tol, G. Groeninckx, I. Vinckier, P. Moldenaers, and J. Mewis, "Phase morphology and stability of co-continuous (PPE/PS)/PA6 and PS/PA6 blends: effect of rheology and reactive compatibilization," *Polymer*, vol. 45, no. 8, pp. 2587–2601, 2004.
- [20] Z. Safidine, S. Fellahi, and A. Frick, "Crystallization behavior of PP/PP-g-MAH/GFR PA66 blends: establishment of their continuous-cooling-transformation of relative crystallinity diagrams," *Journal of Applied Polymer Science*, vol. 104, no. 3, pp. 1620–1626, 2007.
- [21] C. Q. Li, Y. Zhang, and Y. X. Zhang, "Rheological and mechanical properties of PC/HDPE/glass fiber composites," *Polymers & Polymer Composites*, vol. 10, no. 8, pp. 619–626, 2002.
- [22] C.-R. Chiang and F.-C. Chang, "Polymer blends of polyamide-6 (PA6) and poly(phenylene oxide) (PPO) compatibilized by styrene-maleic anhydride (SMA) copolymer," *Polymer*, vol. 38, no. 19, pp. 4807–4817, 1997.
- [23] C.-R. Chiang and F.-C. Chang, "Polymer blends of polyamide-6 and poly(phenylene oxide) compatibilized by styrene-co-glycidyl methacrylate," *Journal of Applied Polymer Science*, vol. 61, no. 13, pp. 2411–2421, 1996.
- [24] D. Z. Wu, X. D. Wang, and R. G. Jin, "Toughening of poly(2,6-dimethyl-1,4-phenylene oxide)/nylon 6 alloys with functionalized elastomers via reactive compatibilization: morphology, mechanical properties, and rheology," *European Polymer Journal*, vol. 40, no. 6, pp. 1223–1232, 2004.

- [25] B. Li, C. Wan, Y. Zhang, and J. Ji, "Blends of poly(2,6-dimethyl-1,4-phenylene oxide)/polyamide 6 toughened by maleated polystyrene-based copolymers: mechanical properties, morphology, and rheology," *Journal of Applied Polymer Science*, vol. 115, no. 6, pp. 3385–3392, 2010.
- [26] B. Li, C. Wan, Y. Zhang, J. Ji, and Y. Su, "Reactive compatibilization and elastomer toughening of poly(2,6-dimethyl-1,4-phenylene oxide)/polyamide 6 blends," *Polymers & Polymer Composites*, vol. 18, no. 4, pp. 219–226, 2010.
- [27] Y. Son and S. Lee, "One step method for fabrication of PPO/PA-66/elastomer blends," *Polymer Bulletin*, vol. 56, no. 2-3, pp. 267–273, 2006.
- [28] K.-C. Chiou, S.-C. Wu, H.-D. Wu, and F.-C. Chang, "Compatibilization and elastomer toughening of polyamide-6 (PA6)/poly(phenylene ether) (PPE) blends," *Journal of Applied Polymer Science*, vol. 74, no. 1, pp. 23–32, 1999.
- [29] S. P. Jang and D. Kim, "Thermal, mechanical, and diffusional properties of nylon 6/ABS polymer blends: compatibilizer effect," *Polymer Engineering and Science*, vol. 40, no. 7, pp. 1635–1642, 2000.
- [30] D. García-López, S. López-Quintana, I. Gobernado-Mitre, J. C. Merino, and J. M. Pastor, "Study of melt compounding conditions and characterization of polyamide 6/metallocene ethylene-polypropylene-diene copolymer/maleated ethylene-polypropylene-diene copolymer blends reinforced with layered silicates," *Polymer Engineering & Science*, vol. 47, no. 7, pp. 1033–1039, 2007.
- [31] R. Gallego, D. García-López, S. López-Quintana, I. Gobernado-Mitre, J. C. Merino, and J. M. Pastor, "Influence of blending sequence on micro- and macrostructure of PA6/mEPDM/EPDMgMA blends reinforced with organoclay," *Journal of Applied Polymer Science*, vol. 109, no. 3, pp. 1556–1563, 2008.
- [32] J. Chen, J.-W. Chen, H.-M. Chen, J.-H. Yang, C. Chen, and Y. Wang, "Effect of compatibilizer and clay on morphology and fracture resistance of immiscible high density polyethylene/polyamide 6 blend," *Composites Part B: Engineering*, vol. 54, no. 1, pp. 422–430, 2013.
- [33] N. Hasegawa, H. Okamoto, M. Kawasumi, M. Kato, A. Tsukigase, and A. Usuki, "Polyolefin-clay hybrids based on modified polyolefins and organophilic clay," *Macromolecular Materials and Engineering*, vol. 280–281, pp. 76–79, 2000.
- [34] L. Jiang, J. W. Zhang, and M. P. Wolcott, "Comparison of polylactide/nano-sized calcium carbonate and polylactide/montmorillonite composites: reinforcing effects and toughening mechanisms," *Polymer*, vol. 48, no. 26, pp. 7632–7644, 2007.

## Research Article

# Phospholipid Adsorption Polymeric Materials for Detection of Xylazine and Metabolite in Blood and Urine

Xue Gao,<sup>1,2</sup> Hao Guo,<sup>3</sup> and Chaokang Gu<sup>4</sup>

<sup>1</sup>School of Environmental and Biological Engineering, Chongqing Technology and Business University, Chongqing 400067, China

<sup>2</sup>Chongqing Key Lab of Catalysis & Functional Organic Molecules, Chongqing Technology and Business University, Chongqing 400067, China

<sup>3</sup>Chongqing Institute of Forensic Science, Chongqing 400021, China

<sup>4</sup>Reel Solar Power Inc., San Jose, CA 95131, USA

Correspondence should be addressed to Hao Guo; hao.guo1982@hotmail.com

Received 3 July 2016; Accepted 16 August 2016

Academic Editor: Yiwen Li

Copyright © 2016 Xue Gao et al. This is an open access article distributed under the Creative Commons Attribution License, which permits unrestricted use, distribution, and reproduction in any medium, provided the original work is properly cited.

Polymers have been used in different areas. Recently, polymeric material is favored in analytical area due to its high performance and high consistency, which was used in sample pretreatment in this study. Xylazine poisoning is often seen in body fluid samples obtained from various accidents or suicides. However, the content of xylazine is difficult to detect precisely due to matrix effect in testing practices. In this paper, a method application for phospholipid adsorption polymeric materials to determine xylazine in blood and urine samples was proposed, developed, and validated. Compared with existing method, this method using polymeric pretreatment has a wider linear range of 2.0–2000.0 ng/mL for xylazine and its metabolite 2,6-dimethylaniline in both blood and urine and lower detection limits of 0.3 ng/mL for 2,6-dimethylaniline and xylazine in blood and 0.2 ng/mL for 2,6-dimethylaniline and xylazine in urine. Therefore, this method is suggested to be applied in testing practices by academic groups and commercial organizations.

## 1. Introduction

The variety of polymers gives different research area different opportunities to achieve different functions. In the recent decades, natural polymers have been modified through grafting to conquer their born defects, including the poor solubility and poor mechanical properties [1–4]. Meanwhile, synthetic polymers have been engineered so much to achieve new functions, such as long-term antimicrobial polymers [5]. More importantly, polymers have been regarded as the most important component in composite material towards stronger and smarter materials [6–9] and more precise and more sensitive extraction materials [10, 11]. Especially in the analytical field, polymers play an important role in separation and purification when dealing with novel materials [12, 13] and complicated biosamples [14]. Blood is a complex sample that contains plasma, proteins, and other trace interferents that can often cause matrix effect when using electrospray

ionization (ESI) technology. Therefore, the blood sample preparation is a very important step in the analysis process. In recent years, several new methods have been developed and applied to blood sample preparation, for example, protein and phospholipid removal plate; it has been used for the targeted removal of phospholipids from blood samples. The protocol can remove interferents in the blood as much as possible, especially proteins and phospholipids, resulting in lowered matrix effect and enhanced recovery. The operation of the protocol is simple and convenient, which only needs to conduct the protein precipitation inside the plate and then push samples to flow through the absorber. The resultant filtrate can be used directly in LC-MS detection.

Xylazine has been suggested to be used on various kinds of animals, including dogs, cats, horses, and deer, for antianxiety, sedative, and analgetic purposes [2]. The chemical structure of xylazine resembles that of phenothiazines, tricyclic antidepressants, and clonidine. Xylazine is a highly

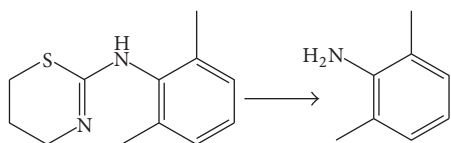


FIGURE 1: The structures of xylazine and DMA.

effective  $\alpha$ -2 adrenergic stimulant, which can stimulate  $\alpha$ -2 receptors at the central nervous system. When those  $\alpha$ -2 receptors are stimulated, the central nervous system reduces the release of norepinephrine and dopamine, resulting in the effects of tranquilizer, painkiller, and muscle relaxant. Xylazine can also affect the cholinergic neuronal system,  $\alpha$ -1 adrenergic receptor, and histamine system [15]. It has been reported that xylazine has been abused for its anesthetic effect either purposely or accidentally in intoxication and criminal cases [16, 17]. Human bodies will show symptoms such as depressed central nervous system, depressed respiratory system, bradycardia, or low blood pressure when intoxicated with xylazine. The main xylazine biotransformation pathway is most likely thiazine ring break-down, and the main product is most likely 2,6-dimethylaniline [15, 18]; the structure of xylazine and 2,6-dimethylaniline was showed in Figure 1. Due to the qualitative detection ability, chromatography-mass spectrometry has been widely used in biological samples [19–22]. The cleanup and target extraction of blood and urine samples have been achieved by different sample preparation methods, such as liquid-liquid extraction (LLE) and solid phase extraction (SPE) [11, 22, 23]. Currently, xylazine detection is usually chromatography or chromatography-mass spectrometry methods. The samples are usually animal-derived foods such as honey and milk [24, 25]. For human intoxications, the detection target is xylazine in blood [26, 27].

To validate this method and to create a reliable sample preparation method quantitatively to determine the xylazine and its metabolite in body fluids, in this paper, phospholipid removal technology was applied in the detection of xylazine and 2,6-dimethylaniline in body fluid sample. At the same time, the results were verified through a comparison with LLE and SPE.

## 2. Material and Methods

**2.1. Chemicals and Reagents.** Acetonitrile, methanol, diethyl ether, n-hexane, ethyl acetate, dichloromethane (LC/MS grade, Fisher Scientific, USA), and formic acid (chromatography grade, ROE, USA) were used as received. Water was purified using a Milli-Q water purification system (Millipore, Billerica, MA, USA), Oasis MCX<sup>®</sup> (30 mg/1 mL; Waters), Cleanert<sup>®</sup> SLE-AQ (30 mg/1 mL, Bonna-Agela Technologies, China), Ostro<sup>®</sup> 96 wells (30 mg/1 mL; Waters), xylazine (high purity, 98.0%, J&K Chemical, China), and 2,6-dimethylaniline (high purity, 98.0%, J&K Chemical, China) were used as received, blank blood was supplied by Chongqing city blood center, and blank urine was supplied by healthy laboratory researchers.

**2.2. Preparation of Standards and QC Samples.** 100 mg/L stock solutions of xylazine and 2,6-dimethylaniline were prepared by dissolving 1.0 mg chemicals in 10 mL acetonitrile. After preparation, stock solutions were stored at  $-20^{\circ}\text{C}$  until use. Working solution mixtures were prepared by serial dilution of the stock solutions with acetonitrile. Matrix-matched calibration standards and QC samples are done by spiking whole blood and urine with the appropriate volume of the mixed working solution. The concentrations of the matrix-matched calibration standards were 2, 5, 10, 50, 100, 500, and 2000 ng/mL and three QC samples at 5, 50, and 500 ng/mL were prepared for whole blood and urine.

**2.3. Instrumentation.** LC-MS/MS was performed using a Shimadzu 20A series liquid chromatograph (Shimadzu Corp., Japan) equipped with AB2000 triple quadrupole mass spectrometry (AB Sciex Pte. Ltd., USA). Chromatographic separation was achieved on a Waters Atlantis dC18 (150 mm  $\times$  3.9 mm, 5  $\mu\text{m}$ ) LC column; temperature:  $40^{\circ}\text{C}$ , sample size: 20  $\mu\text{L}$ , and flow rate: 0.5 mL/min. Mobile phase A is an aqueous solution containing 0.1% formic acid. Mobile phase B is acetonitrile solution containing 0.1% formic acid; the mobile phase is programmed to run in the following sequence: 0-1 min A content is 90%, 2-3 min A content is decreased from 90% to 5%, 3-6 min A content is 5%, 6-7 min A content is increased from 5% back to 90%, and 7-8 min A content is 90%.

The electrospray ionization (ESI) conditions for analyte were as follows: nitrogen was used as nebulizing gas (GS 1, 65 psi), turbo spray gas (GS 2, 65 psi), and curtain gas (20 psi). The collision-activated dissociation (CAD) was set to medium level, while the ion spray voltage was at 4000 V. The dwell time was set at 0.1 seconds, and the Mass Spectrum scanned in positive ion mode.

Simultaneous detection of all glycerophosphocholines (GPCho's) using Mass Spectrum detection was based on Little et al. [27]. The Mass Spectrum parameters for AB2000 triple quadrupole mass spectrometry have been optimized by employing a declustering potential, entrance potential, collision energy, and collision cell exit potential of 180, 10, 7, and 5 V, respectively. The mass transition of  $m/z$  184.2  $\rightarrow$  184.2 was monitored in the positive ion electrospray mode.

### 2.4. Sample Preparation

**2.4.1. SPE.** Solid phase extraction was described in the previous publications [11, 28]. A 100  $\mu\text{L}$  sample was mixed with 200  $\mu\text{L}$  of 2% formic acid and then was vortexed for 10 s and subjected to SPE. The sample mixture was extracted by Oasis MCX SPE cartridge. The cartridge was activated subsequently by 1 mL methanol and 1 mL 2% formic acid acidified water right before use. Cartridges were eluted with 2 mL of 2% ammonia in methanol and then dried under a stream of heated nitrogen at  $40^{\circ}\text{C}$ . Finally, the residues were reconstituted in 100  $\mu\text{L}$  initial mobile phase solution. A 20  $\mu\text{L}$  solution was injected into the LC-MS/MS system for analysis.

**2.4.2. SLE.** A 100  $\mu\text{L}$  sample was mixed with 200  $\mu\text{L}$  deionized water and then was loaded onto a Cleanert SLE-AQ

cartridge. A minimum positive pressure was applied to facilitate the sample absorption into the cartridge in less than 10 s. After the analytes were allowed to equilibrate with the sorbent for 10 min, the analytes were eluted with 1.5 mL of extraction solvent each time for three times. The extraction solvent was eluted by applying a slightly positive pressure from the top and then evaporated to dryness under a stream of heated nitrogen at 40°C. Finally, the residues were reconstituted in 100  $\mu\text{L}$  initial mobile phase solution. A 20  $\mu\text{L}$  solution was injected into the LC-MS/MS system for analysis.

**2.4.3. Protein and Phospholipid Removal Cartridge.** A volume of 300  $\mu\text{L}$  of acetonitrile was transferred to an Ostro 96-well cartridge and then 100  $\mu\text{L}$  plasma was added to the cartridge. The Ostro 96-well cartridge was then manually closed and vortexed. After short moderate mixing, the cartridge was applied to positive pressure and the filtrate was collected into a plastic tube (2 mL Axygen). At this point, the filtrate was ready for immediate LC-MS/MS analysis, but to make this method comparable with the other methods with higher sensitivity, it was concentrated by drying under a nitrogen stream at 40°C and reconstitution in 100  $\mu\text{L}$  of initial mobile phase solution. A 20  $\mu\text{L}$  solution was injected into the LC-MS/MS system for analysis.

**2.5. Method Validation.** Matrix-matched calibration curves were constructed by plotting the peak area ( $y$ ) versus the nominal concentration of the calibration standards ( $x$ ). The linearity of calibration curves was evaluated by fitting calibration curves by weighted least-squares linear regression with a weighting factor of  $1/x$ . Selectivity was investigated by averaging results from five blank samples. The limit of detection (LOD) was set at the lowest concentration yielding at least three signal-to-noise ( $S/N$ ) ratios with an acceptable chromatographic peak shape. The limit of quantification (LOQ) was the lowest concentration with an  $S/N$  ratio greater than 10.

The recovery and matrix effect were evaluated by repeating 6 analyses at 3 QC samples (5, 50, and 500 ng/mL). The recovery was calculated by dividing the average peak area of the analyte spiked before extraction by the average peak area of the analyte spiked after extraction. The matrix effect was estimated by dividing the average peak area of the analyte spiked after extraction by average peak area derived from the neat standards.

Inaccuracy was determined as the percentage deviation of the average of the results from the corresponding nominal value. Imprecision was expressed as the percent relative standard deviation (% RSD). Intraday precision assays were determined by analyzing QC samples (5, 50, and 500 ng/mL) on the same day ( $n = 6$ ).

### 3. Results and Discussion

**3.1. Optimization of SPE Method.** In current studies, three different extraction methods, SPE, SLE, and protein and phospholipid removal, were chosen for comparison. SPE with Oasis MCX polymeric sorbent cartridge, SLE with Cleanert SLE-AQ cartridge, and protein and phospholipid removal

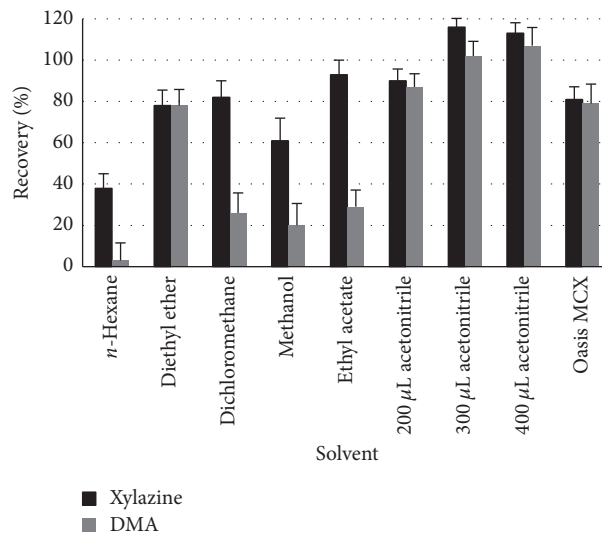


FIGURE 2: Effect of different SPE cartridges on the recoveries of xylazine and DMA.

cartridge with Ostro 96-well cartridge were investigated during the method development. The extraction efficiencies of these three different extraction methods were evaluated by extracting human blood with 100 ng/mL target addition. As shown in Figure 2, the extraction efficiencies for xylazine with SLE were improved significantly when using ethyl acetate as an eluting solution; the recovery increased from 20% to 95%. However, all five eluting solutions used were not able to extract 2,6-dimethylaniline effectively; the recovery was only from 7% to 75%. The extraction efficiencies for xylazine and 2,6-dimethylaniline with SPE according to the literature [17] were 81% and 75%. In contrast, the extraction efficiencies for xylazine and 2,6-dimethylaniline with Ostro 96-well cartridge are 106% and 103%, respectively. It is obvious to draw the conclusion that Ostro 96-well cartridge has the highest extraction efficiency based on the above comparison. Therefore, Ostro 96-well cartridge was employed to treat the sample. Ostro 96-well protein and phospholipid removal cartridge facilitated protein precipitation technology for the targeted removal of phospholipids from plasma and serum samples, which was fast, simple, and less time and sample consuming and could significantly reduce the matrix effect. According to the results obtained by Bruce et al. [29], acetonitrile has better protein removal efficiency than methanol in blood samples. The addition of 0.1% formic acid to acetonitrile is also beneficial for the protein removal. The parameters evaluated in method development need to be optimized for the volume ratio of acetonitrile to blood. Four different ratios of organic solvent to blood were tested: 1:1, 2:1, 3:1, and 4:1 (v/v). 100  $\mu\text{L}$  of blood was used as a blood sample. When the acetonitrile to blood ratio was 1:1, the sample solution is thickened, but there is no protein precipitation. When the ratio was increased to 2:1, the protein recoveries were 87% and 81% for xylazine and 2,6-dimethylaniline, respectively, suggesting the proteins were not precipitated completely. When the acetonitrile to blood ratio was further increased

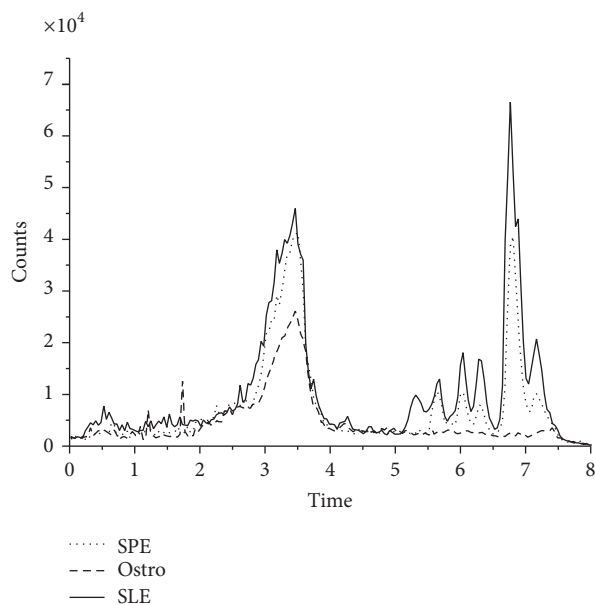


FIGURE 3: GPC's profiles of three different extraction methods.

to 3:1 or 4:1, the recoveries for both xylazine and 2,6-dimethylaniline were close to 100%. Taking the sensitivity into account, the dilution factor of samples should be as little as possible. Thus, a ratio of 3:1 was used.

Glycerophosphocholines (GPCh's) are known to cause liquid chromatography-mass spectrometry/mass spectrometry (LC-MS/MS) matrix ionization effects during the analysis of blood samples. To evaluate the phospholipid removal performance of three methods, in source collision, induced dissociation [30] was employed to monitor the major GPCh's causing matrix effect. Blood samples pretreated by the proposed three methods and their 184.2-184.2 ion couples were monitored by MRM method under the same LC condition. The resultant profile is shown in Figure 3. It is apparent that the phospholipid profiles after different pretreatments differ significantly. As indicated in retention time 2–4 min, phospholipids removal by Ostro cartridge is more efficient than the other two methods, although phospholipids are not completely removed. Also, there are no phospholipid peaks in the mass spectra in the 6.5–7.5 min range of blood sample pretreated by Ostro cartridge method. In contrast, blood samples pretreated by SPE and SLE methods show apparent phospholipid peaks. Thus, it can be concluded that the phospholipid removal efficiency is in the following order: Ostro cartridge > SPE > SLE. Ostro cartridge has the best phospholipid removal and lowest matrix effect, which significantly enhances the target recovery and accuracy. Also, it can provide other potential benefits such as longer LC column lifetime due to the lowered phospholipid content. Regarding pretreatment time, Ostro cartridge method requires the shortest time among the three since it only needs filtration, while SPE requires multiple step procedures to activate and rinse the extraction column and SLE requires a waiting time of 5–10 minutes to reach equilibrium. In other words, Ostro cartridge method is the best among the three for high-throughput sample processing.

**3.2. Optimization of Chromatographic Separation.** Mobile phase composition and addition would affect the targets separation and ionization efficiencies. Two organic solvents, methanol and acetonitrile, as mobile phases were investigated for the effect of mobile phases on the retention time and peak shapes. When methanol was used as mobile phase, the peak showed an apparent tail and its base had been widening. It had longer retention time too. In contrast, the peak shape improved, and retention time is shorter when acetonitrile was used as mobile phase, at the expense of baseline noise. The amine groups on xylazine and 2,6-dimethylaniline could facilitate ionization under acidic conditions. 0.05%, 0.10%, and 0.15% formic acid were added into mobile phase to study the sensitivity of target compounds at various acidities. The results (not shown) suggested the highest sensitivity at 0.10% formic acid. There was no significant improvement in sensitivity when increasing formic acid concentration from 0.10% to 0.15%. The addition of formic acid into acetonitrile mobile phase greatly improved the sensitivity of both xylazine and 2,6-dimethylaniline, which was more than enough to offset the baseline noise. Thus, the mobile phase composition was selected to be 0.10% formic acid in acetonitrile and water. Such mobile phase, with gradient elution, could be helpful to improve the peak shape and enhance ionization efficiencies.

**3.3. Optimization of MS Detection.** The amine functional groups on both target compounds could be easily protonated at lower pH environments, making the two target compounds suitable to be analyzed under positive ion mode. 2,6-Dimethylaniline and xylazine protonated molecules  $[M+H]^+$  were observed in the full spectra MS scan under positive mode at  $m/z$  122 and  $m/z$  221, respectively, when tuned with a single standard solution. After the affirmation of precursor ions, more than two products should be chosen when using LC-MS analysis.

Then MS/MS scan was performed to each precursor ion; the major fragments of 2,6-dimethylaniline were at  $m/z$  105 and  $m/z$  77, which were selected to construct MRM transitions with precursor ion at  $m/z$  122 (Figure 4(a)). Five major fragments of xylazine were observed at  $m/z$  164,  $m/z$  147,  $m/z$  121,  $m/z$  105, and  $m/z$  89 (Figure 4(b)) [25]. Last but not least, MRM transitions with  $m/z$  164 and  $m/z$  89 for  $m/z$  211 were selected to monitor in the determination of xylazine. The addition of formic acid into mobile phase could enhance ionization efficiencies, target responses, and sensitivities. The optimized parameters, including DP, CE, and CXP, were listed in Table 1.

**3.4. Method Validation.** In the MRM mode, the high selectivity for the determination of xylazine and 2,6-dimethylaniline in blood and urine samples was found. The typical MS/MS spectra of spiked blood and urine samples and the blank blood and urine samples are depicted in Figure 5. No additional peaks due to endogenous substances that could have interfered with the detection of xylazine and 2,6-dimethylaniline were observed. The LODs were 0.3 and 0.2 ng/mL for xylazine and 2,6-dimethylaniline in blood and urine. The LOQs were 1.0 and 0.6 ng/mL for xylazine and 2,6-dimethylaniline in blood and urine in Table 2. Standard

TABLE I: MS parameters of xylazine and DMA.

Compound	MW	Precursor/product	DP (eV)	CE (V)	CXP
Xylazine	220	221/164, 221/89*	40/40	35/34	8/5
DMA	121	122/105*, 122/77	30/30	23/31	6/6

\*The quantification production.

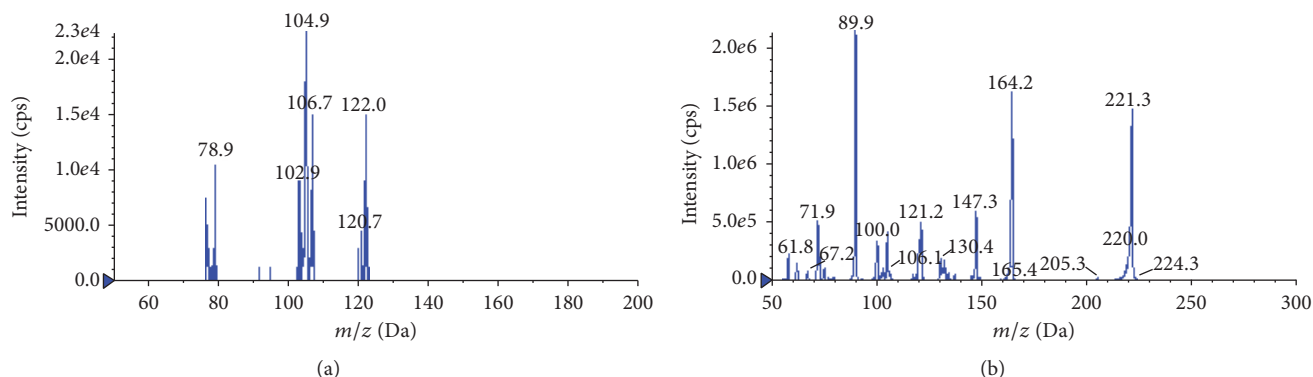


FIGURE 4: The MS scan spectrum of DMA (a) and xylazine (b).

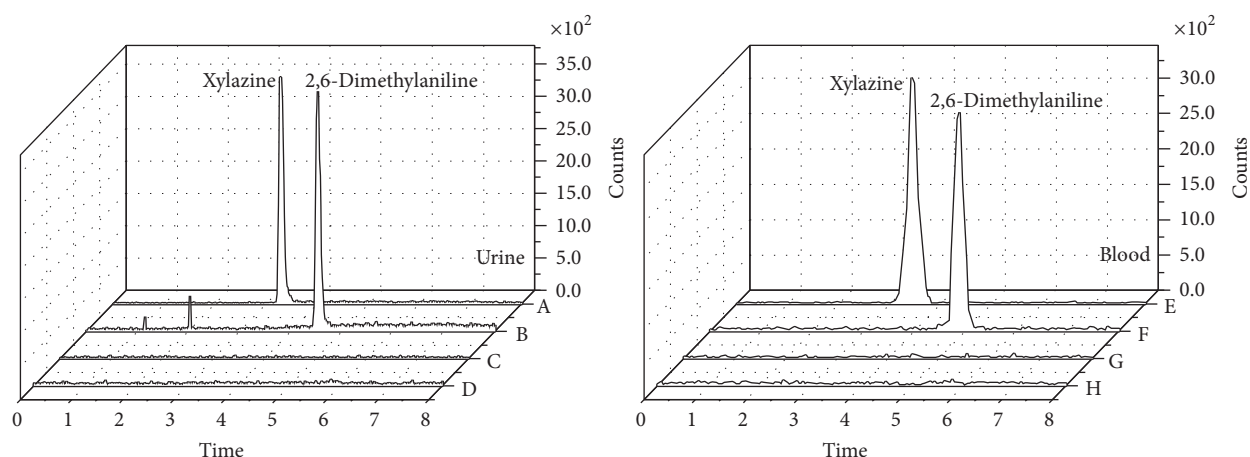


FIGURE 5: Representative MRM chromatograms: (A) blank urine spiked with xylazine (100 ng/mL); (B) blank urine spiked with DMA (100 ng/mL); (C) blank urine for xylazine; (D) blank urine for 2,6-dimethylaniline; (E) blank blood spiked with xylazine (100 ng/mL); (F) blank blood spiked with DMA (100 ng/mL); (G) blank blood for xylazine; (H) blank urine blood 2,6-dimethylaniline.

calibration curves were linear over the curve range between 2 and 2000 ng/mL in blood and urine for both xylazine and 2,6-dimethylaniline; the linear regression equations were in Table 2.

Recovery precision and matrix effect (ME) were repeating analysis for each QC sample 6 times. The QC samples were solutions containing 5, 50, and 500 ng/mL target compounds. The results are summarized in Table 2. The extraction recovery rates were consistent and greater than 93.8%, which indicated that protein and phospholipid removal cartridge was optimal for xylazine and 2,6-dimethylaniline. The precision, assessed by the relative standard deviation (RSD) for the replicate analysis, was typically less than 9%.

Since the selectivity of the HPLC-MS/MS method could be affected by matrix effects by the sample matrix and interferences from compound metabolites, matrix effects are

investigated to develop a more specific and reliable method. The matrix effect ranged from 101.1 to 108.2% for both analytes. This result suggested that ion suppression or enhancement from the blood and urine matrix was negligible under the current treatment method. With a low matrix effect and consistent and reproducible recovery, this assay has proved to be reliable for bioanalysis.

**3.5. Application to Actual Samples.** A 36-year-old woman ingested a certain amount of xylazine after a quarrel with her husband and became unconscious. She was immediately sent to the hospital when her family discovered and was found dead at the time of arriving at hospital. A heart blood sample was collected from the subject for toxicological analysis; xylazine and 2,6-dimethylaniline were confirmed and quantified at 267 ng/mL and 451 ng/mL in the whole blood sample.

TABLE 2: LODs, LOQs, and linear relationships of xylazine and DMA.

Matrix	Analyte	LODs (ng/mL)	LOQs (ng/mL)	Linear range (ng/mL)	Linear equation	Related coefficient ( $R^2$ )	Spiked con- centration (ng/mL)	Recovery (%)	RSD (%)	Matrix effect (%)
Blood	Xylazine	0.3	1.0	2/2000	$y = 2.37 \times 10^3 x + 3.15 \times 10^2$	0.9992	5, 50, 500	101.2, 107.4, 112.5	6.5, 6.1, 4.7	103.1, 105.3, 102.7
	DMA	0.3	1.0	2/2000	$y = 2.19 \times 10^3 x + 4.87 \times 10^2$	0.9981	5, 50, 500	95.1, 97.9, 102.7	8.6, 8.1, 7.2	105.7, 107.7, 104.2
Urine	Xylazine	0.2	0.6	2/2000	$y = 2.75 \times 10^3 x + 5.16 \times 10^2$	0.9993	5, 50, 500	96.9, 110.5, 117.4	6.2, 4.8, 4.3	105.9, 102.6, 101.1
	DMA	0.2	0.6	2/2000	$y = 2.24 \times 10^3 x + 4.17 \times 10^2$	0.9984	5, 50, 500	93.8, 96.7, 101.7	8.1, 7.1, 6.8	108.2, 107.3, 102.7

## 4. Conclusions

In this study, an HPLC-MS/MS method for the quantification of xylazine and 2,6-dimethylaniline in blood and urine samples was developed and validated. A rapid, sensitive, specific, selective, and reproducible assay was developed. Also, the assay required small sample size and simple protein and phospholipid removal cartridge extraction without additional procedures. The sensitive method was successfully applied for the detection of xylazine and 2,6-dimethylaniline in a blood sample for clinical diagnosis and forensic toxicology.

## Competing Interests

The authors declare that there is no conflict of interests regarding the publication of this paper.

## Acknowledgments

This work was supported by Open Foundation of Chongqing Technology and Business University.

## References

- [1] D. Zhu, H. Cheng, J. Li et al., "Enhanced water-solubility and antibacterial activity of novel chitosan derivatives modified with quaternary phosphonium salt," *Materials Science and Engineering C*, vol. 61, pp. 79–84, 2016.
- [2] Y. Chen, J. Li, Q. Li et al., "Enhanced water-solubility, antibacterial activity and biocompatibility upon introducing sulfobetaine and quaternary ammonium to chitosan," *Carbohydrate Polymers*, vol. 143, pp. 246–253, 2016.
- [3] Z. Bin, Z. Wenwen, and Z. Yiwen, "Study on the application of initiator producing graft modified starch size mixture," *Cotton Textile Technology*, vol. 5, pp. 19–22, 2008.
- [4] Q. Xu, J. Wei, J. Wang et al., "Facile synthesis of copper doped carbon dots and their application as a 'turn-off' fluorescent probe in the detection of Fe<sup>3+</sup> ions," *RSC Advances*, vol. 6, no. 34, pp. 28745–28750, 2016.
- [5] W. Zhang, N. R. Vinuesa, P. Datta, and S. Michielsen, "Functional dye as a comonomer in a water-soluble polymer," *Journal of Polymer Science, Part A: Polymer Chemistry*, vol. 53, no. 13, pp. 1594–1599, 2015.
- [6] L. Yao, M. Jiang, D. Zhou et al., "Fabrication and characterization of microstrip array antennas integrated in the three dimensional orthogonal woven composite," *Composites Part B: Engineering*, vol. 42, no. 4, pp. 885–890, 2011.
- [7] Y. Kuang, A. Yang, H. Luan et al., "Effects of structural parameters of textile substrates on the novel textile conformal half-wave dipole antenna," *Journal of Industrial Textiles*, 2016.
- [8] L. Yao and Y. Qiu, "Design and fabrication of microstrip antennas integrated in three dimensional orthogonal woven composites," *Composites Science and Technology*, vol. 69, no. 7-8, pp. 1004–1008, 2009.
- [9] D. Zhou, L. Yao, L. Fei, Z. Da, and M. Jiang, "Tensile and shear properties of three dimensional orthogonal woven basalt/kevlar hybrid composites," *Fiber Composites*, vol. 1, article 017, 2010.
- [10] X. Gong, "Controlling surface properties of polyelectrolyte multilayers by assembly pH," *Physical Chemistry Chemical Physics*, vol. 15, no. 25, pp. 10459–10465, 2013.
- [11] X. Gao, H. Guo, Y. Du, and C. Gu, "Simultaneous determination of xylazine and 2,6-xylidine in blood and urine by auto solid-phase extraction and ultra high performance liquid chromatography coupled with quadrupole-time of flight mass spectrometry," *Journal of Analytical Toxicology*, vol. 39, no. 6, pp. 444–450, 2015.
- [12] J. Wang, P. Jiang, L. Gao et al., "Unique self-assembly properties of a bridge-shaped protein dimer with quantum dots," *Journal of Nanoparticle Research*, vol. 15, no. 9, article 1914, 2013.
- [13] D. Ling, L. Gao, J. Wang et al., "A general strategy for site-directed enzyme immobilization by using NiO nanoparticle decorated mesoporous silica," *Chemistry*, vol. 20, no. 26, pp. 7916–7921, 2014.
- [14] T. Ribeiro, T. J. V. Prazeres, M. Moffitt, and J. P. S. Farinha, "Enhanced photoluminescence from micellar assemblies of cadmium sulfide quantum dots and gold nanoparticles," *The Journal of Physical Chemistry C*, vol. 117, no. 6, pp. 3122–3133, 2013.
- [15] L. I. Velez, G. Shepherd, L. D. Mills, and W. Rivera, "Systemic toxicity after an ocular exposure to xylazine hydrochloride," *Journal of Emergency Medicine*, vol. 30, no. 4, pp. 407–410, 2006.
- [16] U. Hoffmann, C. M. Meister, K. Golle, and M. Zschiesche, "Severe intoxication with the veterinary tranquilizer xylazine in humans," *Journal of Analytical Toxicology*, vol. 25, no. 4, pp. 245–249, 2001.
- [17] K. A. Moore, M. G. Ripple, S. Sakinedzad, B. Levine, and D. R. Fowler, "Tissue distribution of xylazine in a suicide by hanging," *Journal of Analytical Toxicology*, vol. 27, no. 2, pp. 110–112, 2003.
- [18] R. Garcia-Villar, P. L. Toutain, M. Alvinerie, and Y. Ruckebusch, "The pharmacokinetics of xylazine hydrochloride: an interspecific study," *Journal of Veterinary Pharmacology and Therapeutics*, vol. 4, no. 2, pp. 87–92, 1981.
- [19] H. Guo, P. Zhang, J. Wang, and J. Zheng, "Determination of amitraz and its metabolites in whole blood using solid-phase extraction and liquid chromatography-tandem mass spectrometry," *Journal of Chromatography B: Analytical Technologies in the Biomedical and Life Sciences*, vol. 951-952, no. 1, pp. 89–95, 2014.
- [20] Z. Yu, T. Kabashima, C. Tang et al., "Selective and facile assay of human immunodeficiency virus protease activity by a novel fluorogenic reaction," *Analytical Biochemistry*, vol. 397, no. 2, pp. 197–201, 2010.
- [21] I. J. Smallman, F. Wang, T. C. Steimle, M. R. Tarbutt, and E. A. Hinds, "Radiative branching ratios for excited states of 174YbF: application to laser cooling," *Journal of Molecular Spectroscopy*, vol. 300, pp. 3–6, 2014.
- [22] Q. Han, Z. Wang, J. Xia, X. Zhang, H. Wang, and M. Ding, "Application of graphene for the SPE clean-up of organophosphorus pesticides residues from apple juices," *Journal of Separation Science*, vol. 37, no. 1-2, pp. 99–105, 2014.
- [23] S. Kumar Pandey and K.-H. Kim, "Evaluation of the solid-phase extraction (SPE) cartridge method in combination with thermal desorption-gas chromatography-mass spectrometry (TD-GC-MS) for the analysis of different VOCs in liquid matrices in varying pH conditions," *Journal of Separation Science*, vol. 35, no. 15, pp. 1914–1921, 2012.
- [24] X. Zheng, X. Mi, S. Li, and G. Chen, "Determination of Xylazine and 2,6-Xylidine in animal tissues by liquid chromatography-tandem mass spectrometry," *Journal of Food Science*, vol. 78, no. 6, pp. T955–T959, 2013.
- [25] P. Delahaut, P.-Y. Brasseur, and M. Dubois, "Multiresidue method for the detection of tranquilisers, xylazine, and a

- $\beta$ -blocker in animal production by liquid chromatography-tandem mass spectrometry," *Journal of Chromatography A*, vol. 1054, no. 1-2, pp. 373-378, 2004.
- [26] K. Ruiz-Colón, C. Chavez-Arias, J. E. Díaz-Alcalá, and M. A. Martínez, "Xylazine intoxication in humans and its importance as an emerging adulterant in abused drugs: a comprehensive review of the literature," *Forensic Science International*, vol. 240, pp. 1-8, 2014.
- [27] J. L. Little, M. F. Wempe, and C. M. Buchanan, "Liquid chromatography-mass spectrometry/mass spectrometry method development for drug metabolism studies: examining lipid matrix ionization effects in plasma," *Journal of Chromatography B*, vol. 833, no. 2, pp. 219-230, 2006.
- [28] X. Gao, H. Guo, W. Zhang, and C. Gu, "Simultaneous determination of amitraz and its metabolites in blood by support liquid extraction using UPHLC-QTOF," *Journal of Analytical Toxicology*, vol. 40, no. 6, pp. 437-444, 2016.
- [29] S. J. Bruce, I. Tavazzi, V. Parisod, S. Rezzi, S. Kochhar, and P. A. Guy, "Investigation of human blood plasma sample preparation for performing metabolomics using ultrahigh performance liquid chromatography/mass spectrometry," *Analytical Chemistry*, vol. 81, no. 9, pp. 3285-3296, 2009.
- [30] G. M. J. Meyer and H. H. Maurer, "Qualitative metabolism assessment and toxicological detection of xylazine, a veterinary tranquilizer and drug of abuse, in rat and human urine using GC-MS, LC-MS n, and LC-HR-MS n," *Analytical and Bioanalytical Chemistry*, vol. 405, no. 30, pp. 9779-9789, 2013.

## Research Article

# Nanodeserts: A Conjecture in Nanotechnology to Enhance Quasi-Photosynthetic CO<sub>2</sub> Absorption

Wenfeng Wang,<sup>1</sup> Xi Chen,<sup>1</sup> Yifan Zhang,<sup>2</sup> Jianjun Yu,<sup>3</sup> Tianyi Ma,<sup>4</sup> Zhihan Lv,<sup>5</sup> Jing Zhang,<sup>6</sup> Fanyu Zeng,<sup>7</sup> and Hui Zou<sup>8</sup>

<sup>1</sup>State Key Laboratory of Desert and Oasis Ecology, Xinjiang Institute of Ecology and Geography, Chinese Academy of Sciences, Urumqi 830011, China

<sup>2</sup>Department of Chemistry, Inha University, 100 Inharo, Incheon 402-751, Republic of Korea

<sup>3</sup>Environmental Change Institute, University of Oxford, Oxford OX1 3QY, UK

<sup>4</sup>School of Chemical Engineering, University of Adelaide, Adelaide, SA 5005, Australia

<sup>5</sup>High Performance Computing Center, Shenzhen Institutes of Advanced Technology, Chinese Academy of Sciences, Shenzhen 518055, China

<sup>6</sup>College of Energy and Mechanical Engineering, Shanghai University of Electric Power, Shanghai 200090, China

<sup>7</sup>Center for Robotics, University of Electronic Science and Technology of China, Chengdu 610054, China

<sup>8</sup>Department of Computer Science and Technology, Huaqiao University, Xiamen 361021, China

Correspondence should be addressed to Xi Chen; [chenxi@ms.xjb.ac.cn](mailto:chenxi@ms.xjb.ac.cn) and Tianyi Ma; [matianyichem@gmail.com](mailto:matianyichem@gmail.com)

Received 27 April 2016; Revised 22 May 2016; Accepted 5 June 2016

Academic Editor: Yiwen Li

Copyright © 2016 Wenfeng Wang et al. This is an open access article distributed under the Creative Commons Attribution License, which permits unrestricted use, distribution, and reproduction in any medium, provided the original work is properly cited.

This paper advances “nanodeserts” as a conjecture on the possibility of developing the hierarchical structured polymeric nanomaterials for enhancing abiotic CO<sub>2</sub> fixation in the soil-groundwater system beneath deserts (termed as quasi-photosynthetic CO<sub>2</sub> absorption). Arid and semiarid deserts ecosystems approximately characterize one-third of the Earth’s land surface but play an unsung role in the carbon cycling, considering the huge potentials of such CO<sub>2</sub> absorption to expand insights to the long-sought missing CO<sub>2</sub> sink and the naturally unneglectable turbulence in temperature sensitivities of soil respiration it produced. “Nanodeserts” as a reconciled concept not only indicate a conjecture in nanotechnology to enhance quasi-photosynthetic CO<sub>2</sub> absorption, but also aim to present to the desert researchers a better understanding of the footprints of abiotic CO<sub>2</sub> transport, conversion, and assignment in the soil-groundwater system beneath deserts. Meanwhile, nanodeserts allow a stable temperature sensitivity of soil respiration in deserts by largely reducing the CO<sub>2</sub> release above the deserts surface and highlighting the abiotic CO<sub>2</sub> fixation beneath deserts. This may be no longer a novelty in the future.

## 1. Introduction

Attempts to account for the global atmospheric CO<sub>2</sub> fluxes by quantifying CO<sub>2</sub> sources and sinks have provided evidence of an unneglectable missing CO<sub>2</sub> sink [1–3]. There are numerous studies that claimed to find the “missing sink,” but none of those claims has been widely accepted [4, 5]. Recently, the reports of carbon uptake by arid and semiarid desert ecosystems revealed rates of carbon uptake in many forests (i.e., the CO<sub>2</sub> absorption rate is up to the photosynthetic absorption level) and focused research attention on arid and

semiarid deserts ecosystems as the location of the long-sought “missing CO<sub>2</sub> sink” [6–13], which was termed as quasi-photosynthetic CO<sub>2</sub> absorption [6]. There is strong evidence suggesting that absorbed CO<sub>2</sub> significantly contributes to the total soil CO<sub>2</sub> flux [7–10]. Arid and semiarid deserts ecosystems approximately characterize one-third of the Earth’s land surface and play unsung role in the carbon cycling [9]. But where the absorbed CO<sub>2</sub> has gone remains undetermined [11, 12]. A latest publication claimed that such absorption can be attributed to geochemical CO<sub>2</sub> dissolution in saline aquifers beneath deserts [9], but the intensity of

CO<sub>2</sub> dissolution and absorption and the extent to which it modulates the global C balance are still a matter of controversy [9, 13, 14].

Differential, difference, and dynamic equations are used for quantitative analysis in the engineering and natural sciences [15–18]. This suggests us trying to develop some differential equations to describe the dynamics of CO<sub>2</sub> dissolution and absorption beneath deserts. Since absorbed CO<sub>2</sub> is largely dissolved in saline aquifers [9, 10], the dynamic equations for groundwater dissolved in CO<sub>2</sub> (DIC) are representative for both dissolution and absorption. Before this modeling work, the possible difficulties and uncertainties must be theoretically analyzed. Particularly, the quasi-photosynthetic CO<sub>2</sub> absorption as a component of soil respiration in deserts is abound to produce turbulence in temperature sensitivities of soil respiration. The first estimate of the absorption intensity is very promising [12], but a subsequent challenge is how to reduce the CO<sub>2</sub> release above the deserts surface and enhance the abiotic CO<sub>2</sub> fixation beneath deserts. Otherwise, the abiotic CO<sub>2</sub> fixation cannot be utilized [19–22]. Hierarchical structured polymeric materials, benefitting from nanotechnology enhancement, exhibited superior adsorption selectivity, high adsorption capacity, water tolerance, and low energy consumption with respect to physisorption, holding great promise for CO<sub>2</sub> capture, and the capture can consequently, maybe, employed in the future utilization and enhancement of quasi-photosynthetic CO<sub>2</sub> absorption beneath deserts. Considering the rapid development of nanotechnology and the wide applications hierarchical structured polymeric materials [23, 24], it can be conjectured that there are opportunities for the innovative design of self-assembling polymeric materials for the separation of aboveground CO<sub>2</sub> release and underground CO<sub>2</sub> fixation.

This paper hypothesizes that in the future it is possible to develop some hierarchical structured polymeric materials to enhance quasi-photosynthetic CO<sub>2</sub> absorption in deserts and advance “nanodeserts” as a conjecture in nanotechnology for modulating abiotic CO<sub>2</sub> fixation in the soil-groundwater system. To illustrate the necessity for introducing this concept, the influences of quasi-photosynthetic CO<sub>2</sub> absorption on temperature sensitivities of soil respiration are explicitly analyzed. A perspective Riccati Equation for the quasi-photosynthetic CO<sub>2</sub> absorption in the soil-groundwater system is established, providing that the hierarchical structured polymeric materials physically reduce the soil surface CO<sub>2</sub> release and enhance the abiotic CO<sub>2</sub> fixation beneath nanodeserts and allow a stable temperature sensitivity of soil respiration in deserts and a reliable quantification of CO<sub>2</sub> absorption intensity on regional and global nanodeserts.

## 2. Materials and Methods

**2.1. Data Sources.** “Nanodeserts” are a conjecture on the possibility of developing hierarchical structured polymeric materials to enhance abiotic CO<sub>2</sub> fixation in the soil-groundwater system, where nanoporous materials are supposed to be able to largely reduce the CO<sub>2</sub> release from the surface of the soil-groundwater system and enhance the quasi-photosynthetic CO<sub>2</sub> absorption beneath nanodeserts.

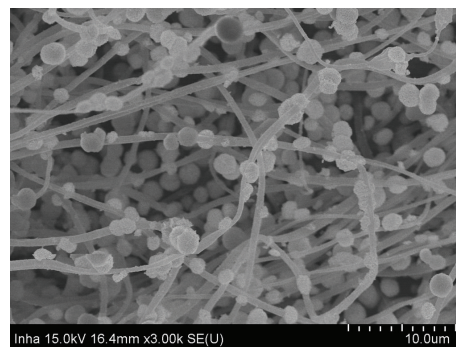


FIGURE 1: SEM image of polyethylenimine (PEI) nanofibers, loading with BiOCl nanoparticles.

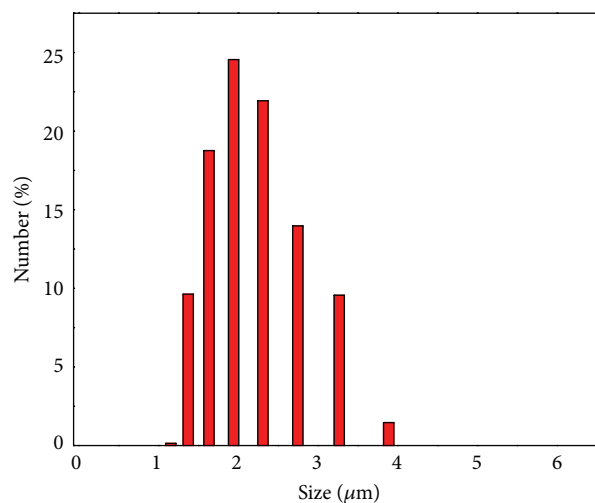


FIGURE 2: SEM image of polyethylenimine (PEI) nanofibers, loading with BiOCl nanoparticles.

As a particular example, the higher-resolution SEM images of polyethylenimine nanofibers (Figures 1, 2, and 3; loading with BiOCl nanoparticles) were collected. The morphology was evaluated via scanning electron microscopy (SEM, Model SU8010, Hitachi Co., Ltd.).

To highlight the necessity for this conjecture, the potential influences of the quasi-photosynthetic CO<sub>2</sub> absorption on the temperature sensitivities ( $Q_{10}$ ) of soil respiration ( $R_s$ ) are basically analyzed. This work is based on the  $R_s$  values (both positive and negative values) and the corresponding  $\theta_s$ ,  $T_a$ , and  $T_s$  values collected from some previous publications, with the analysis of  $Q_{10}$  of  $R_s$  to soil temperature at 5 cm depths ( $T_s$ ) and air temperatures at 10 cm above the soil surface ( $T_a$ ) at typical ecosystems along a gradient of soil alkalinity at 5 cm depths within the Manas River Basin [6, 12, 25].

The Manas River Basin is located at the southern periphery of the Gurbantunggut Desert and in the hinterland of the Eurasian continent. Soils in this inland river basin bear typical physical and chemical characteristics, which are resulting from the soil water and soil salt transport during regional hydrological processes [26]. Almost  $10 \times 10^6$  km<sup>2</sup> of the hinterland of the Eurasian continent is arid and

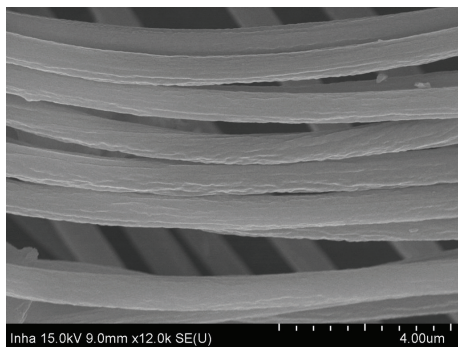


FIGURE 3: The SEM image of polyethylenimine (PEI) nanofibers.

semiarid deserts ecosystems. The inland rivers carried large quantities of salt into the Eurasian continent, resulting in strong, complicated ecological responses and forming the world largest desert-oasis compound system, which allows us to carry experiments at typical saline desert sites and typical cropped farmland sites, respectively.

**2.2. Calculation and Modeling.** The size of the nanoparticles was statistically analyzed utilizing the DLS measurement (Figure 2).  $Q_{10}$  values used in the analysis were calculated using the following formula (for consistence, the negative values of  $R_s$  were not included in calculations of  $Q_{10}$ ), using the simple model of  $R_s$  (the derivative of the exponential chemical reaction-temperature equation originally developed by Van't Hoff) [27]:

$$\frac{R_{sT}}{R_{sT_0}} = Q_{10}^{(T-T_0)/10}, \quad (1)$$

where  $R_{sT}$  and  $R_{sT_0}$  are the  $R_s$  rates ( $\mu\text{mol CO}_2 \text{ m}^{-2} \text{ s}^{-1}$ ) at  $T$  and  $T_0$ , respectively.

Developing hierarchical structured polymeric materials to enhance quasi-photosynthetic  $\text{CO}_2$  absorption beneath nanodeserts is very urgent and might draw much attention in the future. Hypothesizing that such nanoporous carbon materials were finally synthesized, the performance of  $\text{CO}_2$  absorption, conversion, and assignment beneath nanodeserts would be further studied. Therefore, it is also necessary to present a preliminary discussion of the coming modeling work when this interesting and innovative conjecture was demonstrated [28]. Riccati Equation is traditionally serving for the theory of transonic gas-dynamic flows and is hence employed in the present study to illustrate how to model  $\text{CO}_2$  footprints beneath nanodeserts.

### 3. The Major Results

**3.1. Necessity to Introduce "Nanodeserts".** The necessity to introduce "nanodeserts" depends on whether wide utilization of quasi-photosynthetic  $\text{CO}_2$  absorption is feasible and reliable quantification of its overall importance is possible. Since it has been demonstrated that the current soil-groundwater system in arid and semiarid deserts ecosystems contributes

both positive and negative  $\text{CO}_2$  fluxes and the magnitudes of these two fluxes components are almost the same [9–13], wide utilization of quasi-photosynthetic  $\text{CO}_2$  absorption is infeasible unless nanodeserts are introduced. Considering the rapid development of nanotechnology and its applications in  $\text{CO}_2$  capture and storage technology [29–36], nanodeserts as an emerging technology may be no longer a novelty in the future since deserts are attracting more and more interest in the increasingly urbanized world [37–40]. Because the wide range of nanomaterials and the particle sizes provides optional sizes of nanoparticles in the fabrication of nanomaterials (Figure 1), we can conjecture that there is an optimal size of nanoparticles to largely reduce  $\text{CO}_2$  release and meanwhile enhance the abiotic  $\text{CO}_2$  dissolution and fixation beneath nanodeserts.

The turbulence in  $Q_{10}$  values is evident. Quasi-photosynthetic  $\text{CO}_2$  absorption was demonstrated to have significant influences on temperature sensitivities ( $Q_{10}$ ) of soil respiration ( $R_s$ ), which highlight the necessity to introduce "nanodeserts." Using positive  $R_s$  values,  $Q_{10}$  was calculated by the relative change in  $R_s$  with each  $10^\circ\text{C}$  increase of  $T_s$  in the saline desert and cropped farmland largely fell into [1, 2] and [1, 3], respectively, while calculated  $Q_{10}$  by the relative change in  $R_s$  with  $10^\circ\text{C}$  increases of  $T_a$  largely fell into [3, 13] and [2, 4], respectively. The mean  $Q_{10}$  value of  $R_s$  to  $T_a$  ( $Q_{10} = 4.88$ ) was almost three times the mean  $Q_{10}$  value of  $R_s$  to  $T_s$  ( $Q_{10} = 1.66$ ), implying that  $R_s$  in the alkaline land was much more sensitive to  $T_a$  than to  $T_s$ . The mean  $Q_{10}$  value of  $R_s$  to  $T_a$  in the desert ( $Q_{10} = 6.83$ ) was more than the mean  $Q_{10}$  value of  $R_s$  to  $T_a$  in the farmland ( $Q_{10} = 2.95$ ), implying that  $R_s$  in the desert was more sensitive to  $T_a$  than  $R_s$  in the farmland. However,  $R_s$  in the desert was less sensitive to  $T_s$  (with the mean  $Q_{10} = 1.33$ ) than  $R_s$  in the farmland (with the mean  $Q_{10} = 1.98$ ). Although those negative  $R_s$  were excluded and only the positive values were used in the calculations of  $Q_{10}$ , their significant influences on the response of  $R_s$  to  $T_s$  still existed. Additionally, the calculated  $Q_{10}$  uniformly decreased with temperature ( $T = T_s$  or  $T_a$ ) at both sites. This indicated that the variations of  $Q_{10}$  with temperature in alkaline lands were not different from that in other terrestrial ecosystems (Figure 4).

Such turbulence in  $Q_{10}$  values majorly resulted from the alternatively appearing positive and negative  $R_s$ . It is therefore essentially necessary to introduce "nanodeserts" as a conjecture on the possibility of developing hierarchical structured polymeric materials to largely reduce the  $\text{CO}_2$  release from the surface of the soil-groundwater system and enhance the quasi-photosynthetic  $\text{CO}_2$  absorption beneath nanodeserts by nanoporous modulation of the abiotic  $\text{CO}_2$  fixation in the soil-groundwater system. A series of polymers are suitable for nanodeserts working in the future and the chemical structure of polymer specially used for illustration here. The chemisorption of  $\text{CO}_2$  via amine-based materials is an efficient approach to reduce the greenhouse gas emission. In particular, polyethylenimine (PEI) impregnated materials exhibit superior adsorption selectivity, high adsorption capacity, water tolerance, and low energy consumption with respect to physisorption, holding great promise for  $\text{CO}_2$  capture (Figure 5).

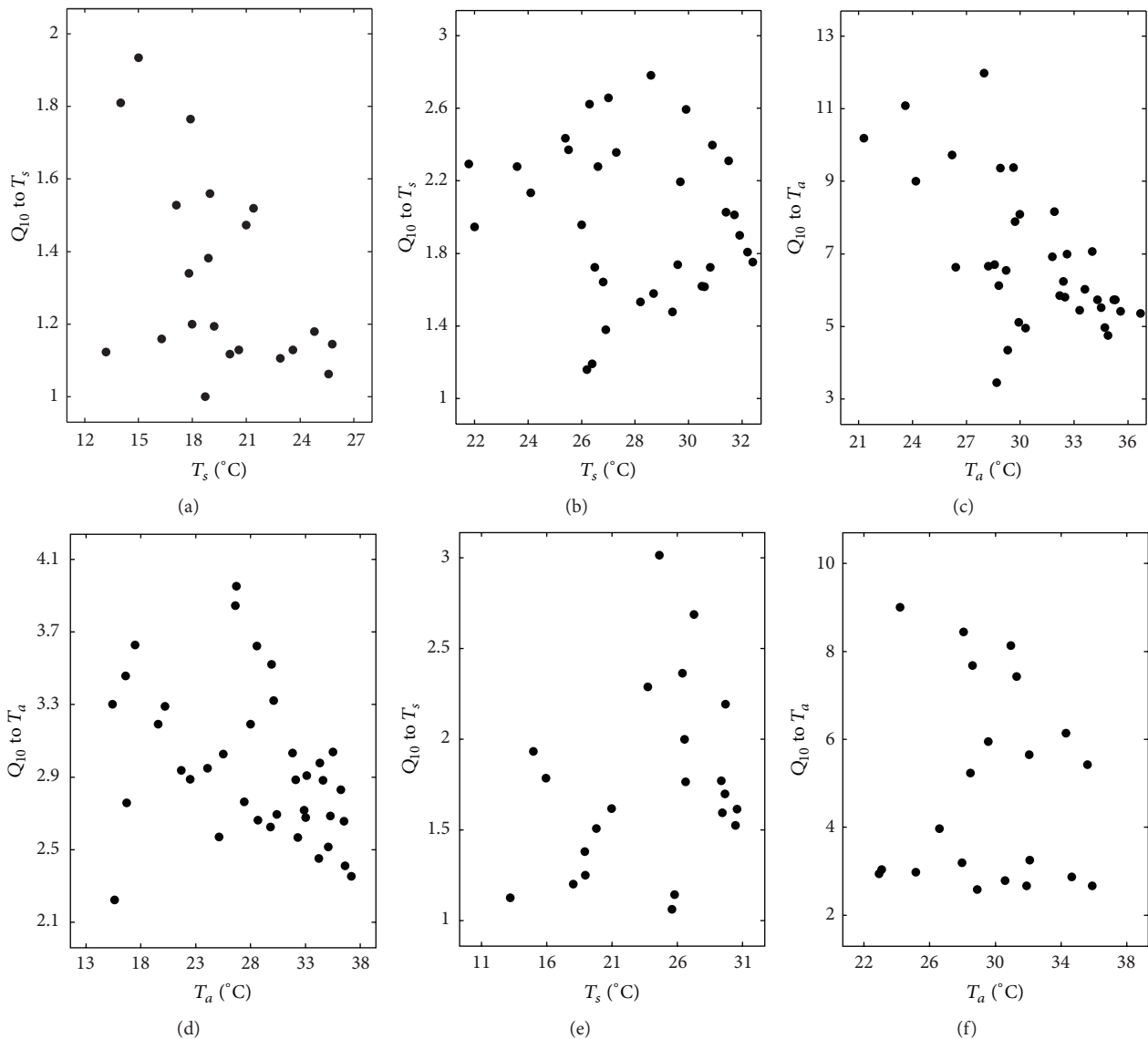


FIGURE 4: Responses of the temperature sensitivity ( $Q_{10}$ ) to soil temperature at 5 cm depth ( $T_s$ ) and air temperature 10 cm above the soil surface ( $T_a$ ) in saline desert (a, c) and cropped farmland (b, d) and the responses of  $Q_{10}$  to  $T_s$  and  $T_a$  when taking the saline desert and cropped farmland data together (e, f).

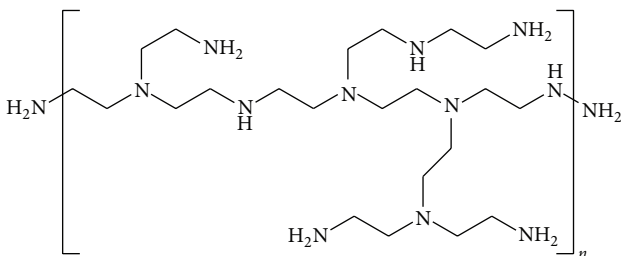


FIGURE 5: The chemical structure of polyethylenimine (PEI).

3.2. *CO<sub>2</sub> Footprints beneath Nanodeserts.* Nanodeserts equipped with hierarchical structured polymeric materials can largely reduce the CO<sub>2</sub> release from the surface of

the soil-groundwater system and enhance the quasi-photosynthetic CO<sub>2</sub> absorption beneath nanodeserts by nanoporous modulation of the abiotic CO<sub>2</sub> fixation in the soil-groundwater system, which not only allows a stable temperature sensitivity ( $Q_{10}$ ) beneath CO<sub>2</sub> absorption and dissolution in the soil-groundwater system, but also makes it easy for deserts researchers to predict the CO<sub>2</sub> footprints beneath nanodeserts. Despite the wide applications of hierarchical structured polymers [41–46], they are slightly associated to modulate the carbon cycle in deserts and so it is difficult to provide the quantification data of polymer used for CO<sub>2</sub> absorption and the efficiency of CO<sub>2</sub> fixation beneath deserts. This is really a challenge. At current stage, we can only present a first approach to quantification data of polymer used for CO<sub>2</sub> absorption and the efficiency of CO<sub>2</sub> fixation beneath deserts based on the parameter of CO<sub>2</sub>

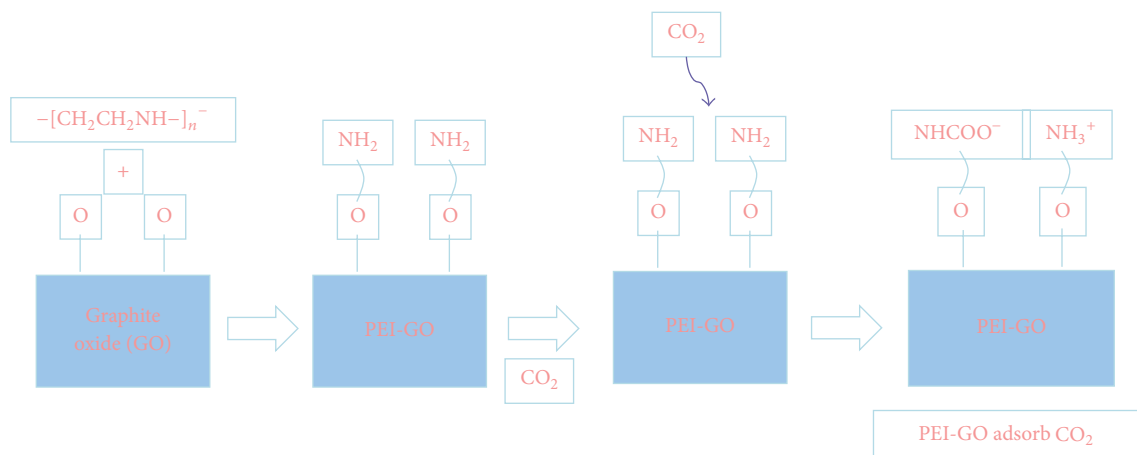


FIGURE 6: Effect of CO<sub>2</sub> capture of impregnated-graphite oxide by polyethylenimine.

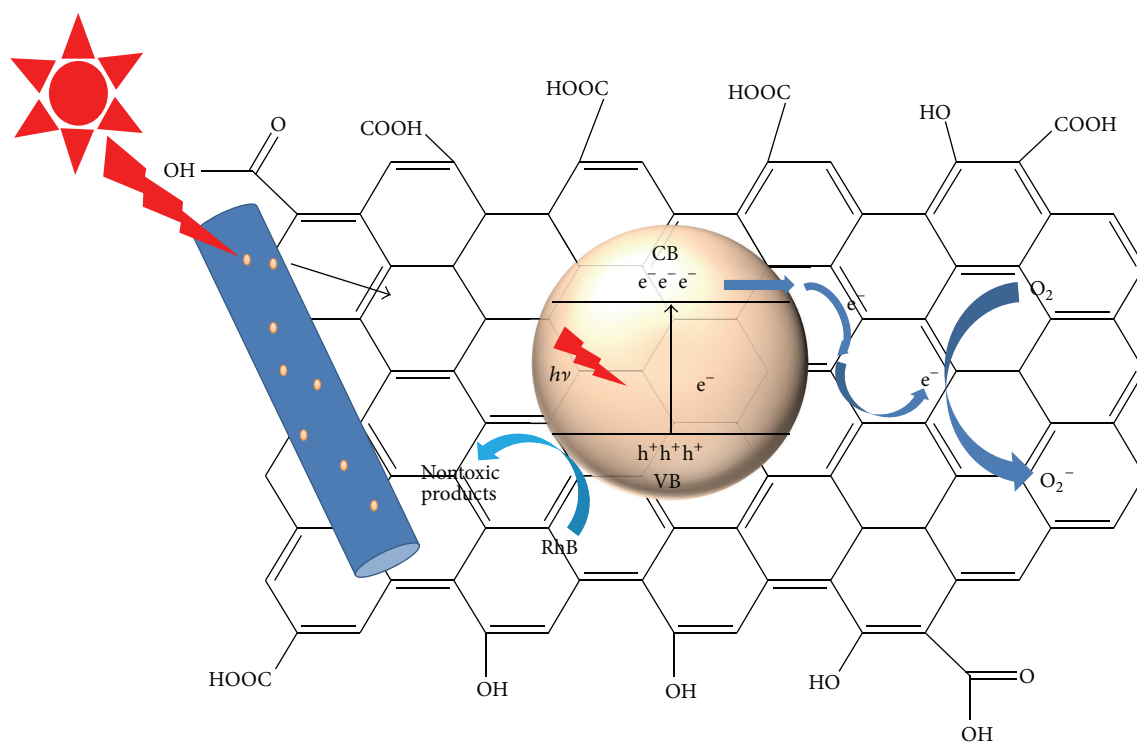


FIGURE 7: A conceptual mechanism about the graphene oxide/BiOCl heterostructured nanofibers (the specified example in this study) for visible-light photocatalytic enhancements of CO<sub>2</sub> fixation.

content, power of visible-light for photocatalysis they used for calculation and modeling. Here is a specific example to explain how to carry out and evaluate the CO<sub>2</sub> capture on polyethylenimine in future investigations. As an illustrating example, the CO<sub>2</sub> adsorption-desorption isotherms were measured at 298 K and 308 K at low pressure (1 bar) using a Model Belsorp Max instrument (BEL Japan, Inc.). A volumetric measurement method was used to obtain the CO<sub>2</sub> adsorption capacity. Before measurement, the samples were degassed for 10 h at 200°C until the residual pressure

fell below 0.01 kPa and then cooled to room temperature. Photocatalytic activities of the as-prepared samples were estimated by the degradation rate of RhB under a Solar Simulator (Sun 2000, ABET) with a 440 nm cutoff filter (Figures 6 and 7).

To predict CO<sub>2</sub> footprints beneath “nanodeserts,” first we establish a mathematical equation to describe the dynamics of CO<sub>2</sub> in the groundwater-soil system beneath hypothetically built “nanodeserts.” Suppose that CO<sub>2</sub> absorption per square-meter alkaline soils was finally dissolved in the groundwater

of volume  $V$ . Let  $D_0$  be the initial amount of DIC at  $t_0$  and the growth rate of DIC is  $r$ . Ignoring groundwater flows and the restricting effect of current DIC, it is straight that

$$\frac{dD_1(t)}{dt} = D_0 \cdot r(t - t_0), \quad (2)$$

where  $D_1(t)$  represents the one-dimension groundwater DIC dynamics.

Noting that  $D_1(0) = D_0$ , the analytic solution of (2) is  $D_1(t) = D_0 \cdot e^{r(t-t_0)}$ .

Now take into account groundwater flows. It is natural to provide that outflow = inflow, with volume  $Q$ . Because such flows are very slow, assume that groundwater flows out after the inflow is uniformly mixed with the groundwater unit  $V$ . The quality conversation law implies

$$D_2(t + \Delta t) - D_2(t) = Qp\Delta t + \int_t^{t+\Delta t} rD_2(t) - Q\frac{D_2(t)}{V+Q}dt, \quad (3)$$

where  $p$  is DIC proportion in the inflows (hypothesized as a constant).

Simplifying and taking the limit  $\Delta t \rightarrow 0$ , it implies

$$\frac{dD_2(t)}{dt} = Qp - \left(\frac{Q}{V+Q} - r\right)D_2(t). \quad (4)$$

Noting that  $D_2(0) = D_0$ , the analytic solution of (2) is

$$D_2(t) = \frac{Qp(V+Q)}{Q-r(V+Q)} - \left(D_0 - \frac{Qp(V+Q)}{Q-r(V+Q)}\right)e^{(r-Q/(V+Q))t}, \quad (5)$$

where  $D_2(t)$  represents the two-dimension groundwater DIC dynamics.

Finally take into account both the groundwater flows and the restricting effect of current DIC. The quality conversation law implies

$$D_3(t + \Delta t) - D_3(t) = Qp\Delta t + \int_t^{t+\Delta t} r(R - \lambda D_3(t))D_3(t) - Q\frac{D_3(t)}{V+Q}dt, \quad (6)$$

where  $R - \lambda D_3(t)$  determines the restricting effect of current DIC on  $r$ .

Simplifying and taking the limit  $\Delta t \rightarrow 0$ , it implies

$$\frac{dD_3(t)}{dt} = Qp + \frac{rR(V+Q) - Q}{V+Q}D_3(t) - \lambda rD_3(t)^2, \quad (7)$$

where  $D_3(t)$  represents the three-dimension groundwater DIC dynamics.

Equation (7) is the famous Riccati Equation, where the parameters  $p$ ,  $Q$ ,  $r$ ,  $R$ , and  $V$  are allowed to be changing with  $t$  [15–18]. Equations (2) and (4) are both simple forms

of (7) and hence are also special forms of the famous Riccati Equation. Generally the Riccati Equation has no analytic solutions unless some assumptions are imposed. And it is better to provide a specific example to prove analytic solutions in certain conditions, which help to understand the full story of CO<sub>2</sub> footprint and make chances for the subsequent quantitative analysis of quasi-photosynthetic CO<sub>2</sub> absorption and fixation beneath nanodeserts (Figure 8).

Suppose its analytic solutions by discussing that root of

$$Qp + \frac{rR(V+Q) - Q}{V+Q}D_3(t) - \lambda rD_3(t)^2 = 0 \quad (8)$$

is zero; that is,  $4\lambda rpQ^2 + (4\lambda rpV + rR - 1)Q + rRV$  is zero; then (8) has two same real roots, say  $d$ , and (7) is simplified as

$$\frac{dD_3(t)}{(D_3(t) - d)^2} = \lambda rdt, \quad (9)$$

where the analytic solution can be obtained by  $D_3(0) = D_0$  and

$$D_3(t) = d - \frac{\lambda r}{t+c}, \quad c \text{ is arbitrary constant.} \quad (10)$$

CO<sub>2</sub> footprints beneath nanodeserts can be therefore theoretically characterized. First, to note the auxiliary role of soil-groundwater metal ions in the CO<sub>2</sub> footprints beneath nanodeserts is significant, which prepare chemical condition for the quasi-photosynthetic CO<sub>2</sub> absorption beneath deserts (Figure 8). This is a key point of the whole story. Those metal ions come from the dissolution of soil salt during the discharge and recharge of groundwater. The percentages of those metal ions beneath deserts can be very different in different sites and the local extremes amount to 80 mg/L [47–56]. Second, the CO<sub>2</sub> movements in the soil-groundwater system beneath nanodeserts are usually accompanied by the movements and sequestration of these metal ions. Finally, such accompanied movements present advantageous conditions for geochemical processes and therefore reconstruct CO<sub>2</sub> footprints beneath nanodeserts. The above assumption and analytic solution (10) indicate that the quasi-photosynthetic CO<sub>2</sub> absorption beneath deserts significantly contributed to the dynamic of the soil-groundwater CO<sub>2</sub> concentration beneath deserts. In other words, the subterranean C pool and CO<sub>2</sub> footprints would be reconstructed in next centuries when/if the quasi-photosynthetic CO<sub>2</sub> absorption becoming the predominant processes was beneath “nanodeserts.”

#### 4. Discussion

In subsequent studies, the diverse kinds of hierarchical structured nanoporous materials should be synthesized as a set of microporous nanomaterials with small pore size and their CO<sub>2</sub> sorption performance should be mechanically analyzed. The performance of CO<sub>2</sub> absorption by the hierarchical structured polymeric nanomaterials needs to be systematically investigated to find the critical pore size to enhance the CO<sub>2</sub> uptake according to the arithmetic method

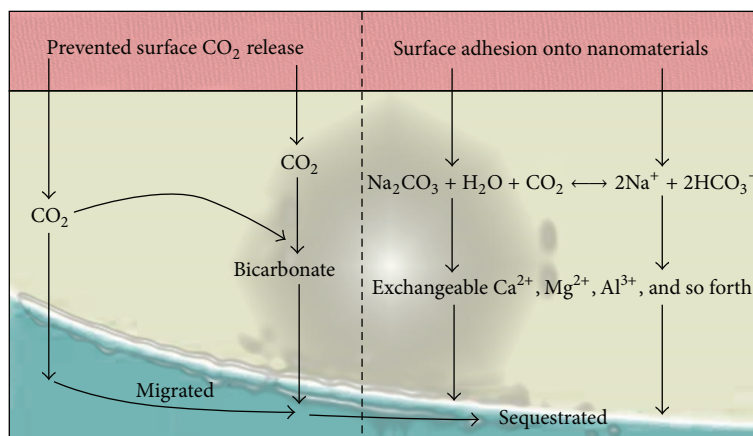


FIGURE 8: Hypothetical CO<sub>2</sub> footprints beneath nanodeserts and the C sink kinetics in CO<sub>2</sub> explosion.

proposed in subsequent studies. Moreover, the exact mechanisms about the heterostructured nanofibers for visible-light photocatalytic enhancements and full utilization of the solar thermal sources above nanodeserts are also worthy of further investigations [57–60].

In the present study it is indicated that it is the micropores with pore size smaller than a necessary pore size for soil CO<sub>2</sub> release that play a crucial role in such abiotic CO<sub>2</sub> adsorption. Such efforts are practical considering the wide applications of the hierarchical structured polymers and the nanomaterials. The pore structure and surface chemical properties of these prepared nanomaterials should be symmetrically studied by using different kinds of testing methods. Additionally, the DLS was used to measure the size of the nanoparticles in the present study since the size of the nanoparticles had been decorated on the PEI fibers. Considering the size of the particles is important for photocatalytic performance [61], it is very important to employ the DLS to measure the size distribution of the nanoparticles. Nevertheless, when measuring the diameter or the length of the PEI nanofiber, other suitable methods must be additionally employed since it is not appropriate to use DLS to measure such size of the fiber.

At the current stage it is impossible to obtain a reliable quantification of the CO<sub>2</sub> adsorption capacity, but a preliminary approach can be concluded from Figures 6 and 7. One can get detailed information from Figures 6 and 7, respectively. In Figure 6, it is highlighted that chemisorption of CO<sub>2</sub> via amine-based solid adsorbents is another efficient approach to reduce the greenhouse gas emission [62]. In particular, polyethylenimine (PEI) impregnated materials exhibit superior adsorption selectivity, high adsorption capacity, water tolerance, and low energy consumption with respect to physisorption, holding great promise for CO<sub>2</sub> capture [63]. Nevertheless, the low thermal conductivity of PEI coupled with high adsorption heat ( $\Delta H$ ) of chemisorption commonly generates overheating of these adsorbents during the CO<sub>2</sub> capture. This unavoidably leads to partial degradation of PEI, poor cycle stability, and even safety problems. Therefore, the development of a suitable material

with high CO<sub>2</sub> adsorption capacity, superior adsorption selectivity, and excellent cycle performance remains a major challenge. In Figure 6, the GO sheets can serve as an efficient carrier support for PEI via a nanocasting technology. Such features are favorable for the efficient diffusion and adsorption of CO<sub>2</sub> as well as the rapid thermal transfer. As for Figure 7, PEI nanofibers were prepared by electrospinning so that the graphene oxide/BiOCl heterostructured PEI nanofibers can be synthesized through in situ method. As well known, harmful chemical compounds have become the main cause of water pollution. For instance, organic dyes are often discharged with wastewater into the local environment without adequate treatment. Although the preparation of graphene-based composite hydrogels for photocatalyst has been previously reported [64, 65], recovering the photocatalyst after waste water purification has been a challenging issue. Thus, polymer-based photocatalyst nanocomposites have been attracting more interest due to their advantages for photocatalyst recovery. Exactly, the formation of graphene oxide/BiOCl heterostructured PEI nanofibers using an in situ reduction approach has been stated in the present study. Interestingly, this composite hydrogel matrix can be further utilized as highly efficient catalyst for wastewater treatment.

Furthermore, the Riccati Equation presented in the present studies demands further investigations by the mathematicians who are interested in this conjecture and are able to make contributions. Therefore, the analysis of qualitative properties of solutions to Riccati Equation is crucial for understanding the CO<sub>2</sub> absorption, offering some cautionary notes for interpretations based on first principles for CO<sub>2</sub> capture at ecosystem level and large-scale applications, which is also a future research priority.

## 5. Conclusion

“Nanodeserts” as a reconciled concept not only indicate a conjecture in nanotechnology to enhance quasi-photosynthetic CO<sub>2</sub> absorption, but also aim to present to desert researchers a better understanding of the footprints of abiotic CO<sub>2</sub> transport, conversion, and assignment in

the soil-groundwater system beneath deserts. Meanwhile, nanodeserts allow a stable temperature sensitivity of soil respiration in deserts by largely reducing the CO<sub>2</sub> release above the deserts surface and highlight the abiotic CO<sub>2</sub> fixation beneath deserts. When/if the dream is realized, it is not difficult then to widely utilize the quasi-photosynthetic CO<sub>2</sub> absorption in the soil-groundwater system and present further explicit modeling results towards a reliable quantification of the quasi-photosynthetic CO<sub>2</sub> absorption beneath nanodeserts. This may be no longer a novelty in the future since deserts are attracting more and more interest in the increasingly urbanized world.

## Competing Interests

The authors declared that there are no competing interests.

## Acknowledgments

This work was financially supported by the National Natural Science Foundation of China (41571299), the “Thousand Talents” Plan (Y474161), the CAS “Light of West China” Program (XBBS-2014-16), and the Shenzhen ICSTI Basic Research Project (JCYJ 20150630114942260). Essential geodata were collected from National Science & Technology Infrastructure Center-Data Sharing Infrastructure of Earth System Science (<http://www.geodata.cn/>).

## References

- [1] R. P. Detwiler and C. A. S. Hall, “Tropical forests and the global carbon cycle,” *Science*, vol. 239, no. 4835, pp. 42–47, 1988.
- [2] P. P. Tans, I. Y. Fung, and T. Takahashi, “Observational constraints on the global atmospheric CO<sub>2</sub> budget,” *Science*, vol. 247, no. 4949, pp. 1431–1438, 1990.
- [3] R. F. Keeling, S. C. Piper, and M. Heimann, “Global and hemispheric CO<sub>2</sub> sinks deduced from changes in atmospheric O<sub>2</sub> concentration,” *Nature*, vol. 381, no. 6579, pp. 218–221, 1996.
- [4] D. W. Schindler, “The mysterious missing sink,” *Nature*, vol. 398, no. 6723, pp. 105–107, 1999.
- [5] S. C. Wofsy, “Where has all the carbon gone?” *Science*, vol. 292, no. 5525, pp. 2261–2263, 2001.
- [6] W. Wang, X. Chen, H. Zhang, C. Jing, Y. Zhang, and B. Yan, “Highlighting photocatalytic H<sub>2</sub>-production from natural seawater and the utilization of quasi-photosynthetic absorption as two ultimate solutions for CO<sub>2</sub> mitigation,” *International Journal of Photoenergy*, vol. 2015, Article ID 481624, 11 pages, 2015.
- [7] J. X. Xie, Y. Li, C. X. Zhai, C. H. Li, and Z. D. Lan, “CO<sub>2</sub> absorption by alkaline soils and its implication to the global carbon cycle,” *Environmental Geology*, vol. 56, no. 5, pp. 953–961, 2009.
- [8] E. L. Yates, A. M. Detweiler, L. T. Iraci et al., “Assessing the role of alkaline soils on the carbon cycle at a playa site,” *Environmental Earth Sciences*, vol. 70, no. 3, pp. 1047–1056, 2013.
- [9] Y. Li, Y.-G. Wang, R. A. Houghton, and L.-S. Tang, “Hidden carbon sink beneath desert,” *Geophysical Research Letters*, vol. 42, no. 14, pp. 5880–5887, 2015.
- [10] J. Ma, Z.-Y. Wang, B. A. Stevenson, X.-J. Zheng, and Y. Li, “An inorganic CO<sub>2</sub> diffusion and dissolution process explains negative CO<sub>2</sub> fluxes in saline/alkaline soils,” *Scientific Reports*, vol. 3, article 2025, 2013.
- [11] X. Chen and W. F. Wang, “On the apparent CO<sub>2</sub> absorption by alkaline soils,” *Biogeosciences Discussions*, vol. 11, no. 2, pp. 2665–2683, 2014.
- [12] X. Chen, W. F. Wang, G. P. Luo, and H. Ye, “Can soil respiration estimate neglect the contribution of abiotic exchange?” *Journal of Arid Land*, vol. 6, no. 2, pp. 129–135, 2014.
- [13] X. Chen, W.-F. Wang, G.-P. Luo, L.-H. Li, and Y. Li, “Time lag between carbon dioxide influx to and efflux from bare saline-alkali soil detected by the explicit partitioning and reconciling of soil CO<sub>2</sub> flux,” *Stochastic Environmental Research and Risk Assessment*, vol. 27, no. 3, pp. 737–745, 2013.
- [14] W. H. Schlesinger, J. Belnap, and G. Marion, “On carbon sequestration in desert ecosystems,” *Global Change Biology*, vol. 15, no. 6, pp. 1488–1490, 2009.
- [15] B.-F. Kou and Q.-Z. Liu, “Wetting behavior of hydrophobic dust and dust-fall theory of fine droplets,” *Brazilian Journal of Physics*, vol. 45, no. 6, pp. 708–712, 2015.
- [16] C. Zhao, W. M. Ding, F. Chen, C. Cheng, and Q. J. Shao, “Effects of compositional changes of AFEX-treated and H-AFEX-treated corn stover on enzymatic digestibility,” *Biore-source Technology*, vol. 155, no. 3, pp. 34–40, 2014.
- [17] Q. Feng, S. Li, X. Han, and S. Wang, “Network simulation for formation impairment due to suspended particles in injected water,” *Journal of Petroleum Science and Engineering*, vol. 133, pp. 384–391, 2015.
- [18] J. Tan, S. Wang, J. Yang, and Y. Liu, “Coupled particulate and continuum model for nanoparticle targeted delivery,” *Computers and Structures*, vol. 122, pp. 128–134, 2013.
- [19] V. A. Laudicina, A. Novara, L. Gristina, and L. Badalucco, “Soil carbon dynamics as affected by long-term contrasting cropping systems and tillages under semiarid Mediterranean climate,” *Applied Soil Ecology*, vol. 73, pp. 140–147, 2014.
- [20] Y. G. Su, L. Wu, Z. B. Zhou, Y. B. Liu, and Y. M. Zhang, “Carbon flux in deserts depends on soil cover type: a case study in the Gurbantunggute desert, North China,” *Soil Biology & Biochemistry*, vol. 58, pp. 332–340, 2013.
- [21] Y. Wang, Z. Wang, and Y. Li, “Storage/turnover rate of inorganic carbon and its dissolvable part in the profile of saline/alkaline soils,” *PLoS ONE*, vol. 8, no. 11, article e82029, 2013.
- [22] J. Huang, Z. J. Gao, J. Chen, H. Zhang, and B. C. Xu, “Diurnal and seasonal variations of soil respiration rate under different row-spacing in a *Panicum virgatum* L. field on semi-arid Loess Plateau of China,” *Journal of Arid Land*, vol. 8, no. 3, pp. 341–349, 2016.
- [23] X. Gong, “Controlling surface properties of polyelectrolyte multilayers by assembly pH,” *Physical Chemistry Chemical Physics*, vol. 15, no. 25, pp. 10459–10465, 2013.
- [24] M. Zhang, F. Yang, S. Pasupuleti et al., “Preventing adhesion of *Escherichia coli* O157: H7 and *Salmonella* Typhimurium LT2 on tomato surfaces via ultrathin polyethylene glycol film,” *International Journal of Food Microbiology*, vol. 185, pp. 73–81, 2014.
- [25] W. F. Wang, X. Chen, G. P. Luo, and L. H. Li, “Modeling the contribution of abiotic exchange to CO<sub>2</sub> flux in alkaline soils of arid areas,” *Journal of Arid Land*, vol. 6, no. 1, pp. 27–36, 2014.
- [26] R. Stone, “Have desert researchers discovered a hidden loop in the carbon cycle?” *Science*, vol. 320, no. 5882, pp. 1409–1410, 2008.

- [27] J. Lloyd and J. A. Taylor, "On the temperature dependence of soil respiration," *Functional Ecology*, vol. 8, no. 3, pp. 315–323, 1994.
- [28] N. Y. Kapustin and K. B. Sabitov, "The role of the Riccati equation in the theory of transonic gas dynamic flows," *Matematicheskoe Modelirovanie*, vol. 2, no. 9, pp. 105–113, 1990.
- [29] B. Yan, P. S. Zhou, Q. Xu, X. F. Zhou, D. D. Xu, and J. H. Zhu, "Engineering disorder into exotic electronic 2D TiO<sub>2</sub> nanosheets for enhanced photocatalytic performance," *RSC Advances*, vol. 6, no. 8, pp. 6133–6137, 2016.
- [30] Y. L. Liu, Q. J. Guo, S. Q. Wang, and W. Hu, "Electrokinetic effects on detection time of nanowire biosensor," *Applied Physics Letters*, vol. 100, no. 15, Article ID 153502, 2012.
- [31] S. Wang, Y. Wan, and Y. Liu, "Effects of nanopillar array diameter and spacing on cancer cell capture and cell behaviors," *Nanoscale*, vol. 6, no. 21, pp. 12482–12489, 2014.
- [32] H. Dong, B. Lin, K. Gilmore, T. Hou, S.-T. Lee, and Y. Li, "B<sub>40</sub> fullerene: an efficient material for CO<sub>2</sub> capture, storage and separation," *Current Applied Physics*, vol. 15, no. 9, pp. 1084–1089, 2015.
- [33] N. N. A. H. Meis, J. H. Bitter, and K. P. D. Jong, "Support and size effects of activated hydrotalcites for precombustion CO<sub>2</sub> capture," *Industrial & Engineering Chemistry Research*, vol. 49, no. 3, pp. 1229–1235, 2010.
- [34] I. Ganesh, "Electrochemical conversion of carbon dioxide into renewable fuel chemicals—the role of nanomaterials and the commercialization," *Renewable and Sustainable Energy Reviews*, vol. 59, pp. 1269–1297, 2016.
- [35] F. Atalay, "Synthesis of NiO nanostructures using *Cladosporium cladosporioides* fungi for energy storage applications," *Nanomaterials and Nanotechnology*, vol. 6, no. 28, pp. 1–6, 2016.
- [36] L. K. Pan, "Editorial: functional semiconductor nanomaterials for renewable energy conversion and storage," *Current Nanoscience*, vol. 12, no. 3, pp. 316–316, 2016.
- [37] A. Mirzabaev, M. Ahmed, J. Werner, J. Pender, and M. Louhaichi, "Rangelands of Central Asia: challenges and opportunities," *Journal of Arid Land*, vol. 8, no. 1, pp. 93–108, 2016.
- [38] N. B. Grimm, S. H. Faeth, N. E. Golubiewski et al., "Global change and the ecology of cities," *Science*, vol. 319, no. 5864, pp. 756–760, 2008.
- [39] H. Wan, C. Huang, and J. Pang, "Major elements in the Holocene loess-paleosol sequence in the upper reaches of the Weihe River valley, China," *Journal of Arid Land*, vol. 8, no. 2, pp. 197–206, 2016.
- [40] H. Sohrabi, S. Bakhtiarvand-Bakhtiari, and K. Ahmadi, "Above- and below-ground biomass and carbon stocks of different tree plantations in central Iran," *Journal of Arid Land*, vol. 8, no. 1, pp. 138–145, 2016.
- [41] J. Ruokolainen, G. Ten Brinke, and O. Ikkala, "Supramolecular polymeric materials with hierarchical structure-within-structure morphologies," *Advanced Materials*, vol. 11, no. 9, pp. 777–780, 1999.
- [42] E. Baer, A. Hiltner, and H. D. Keith, "Hierarchical structure in polymeric materials," *Science*, vol. 235, no. 4792, pp. 1015–1022, 1987.
- [43] Y. Cui, A. T. Paxson, K. M. Smyth, and K. K. Varanasi, "Hierarchical polymeric textures via solvent-induced phase transformation: a single-step production of large-area superhydrophobic surfaces," *Colloids and Surfaces A: Physicochemical and Engineering Aspects*, vol. 394, pp. 8–13, 2012.
- [44] Y. Yoon, D. Kim, and J. B. Lee, "Hierarchical micro/nano structures for super-hydrophobic surfaces and super-lyophobic surface against liquid metal," *Micro & Nano Systems Letters*, vol. 2, no. 1, pp. 1–18, 2014.
- [45] J. W. Lee, C. Lee, S. Y. Choi, and S. H. Kim, "Block copolymer-surfactant complexes in thin films for multiple usages from hierarchical structure to nano-objects," *Macromolecules*, vol. 43, no. 1, pp. 442–447, 2010.
- [46] R. Akbarzadeh, J. A. Minton, C. S. Janney, T. A. Smith, P. F. James, and A.-M. Yousefi, "Hierarchical polymeric scaffolds support the growth of MC<sub>3</sub>T<sub>3</sub>-E<sub>1</sub> cells," *Journal of Materials Science: Materials in Medicine*, vol. 26, no. 2, pp. 1–12, 2015.
- [47] Y. Q. Cui, J. Y. Ma, and W. Sun, "Application of stable isotope techniques to the study of soil salinization," *Journal of Arid Land*, vol. 3, no. 4, pp. 285–291, 2011.
- [48] S. Danierhan, A. Shalamu, H. Tumaerbai, and D. Guan, "Effects of emitter discharge rates on soil salinity distribution and cotton (*Gossypium hirsutum* L.) yield under drip irrigation with plastic mulch in an arid region of Northwest China," *Journal of Arid Land*, vol. 5, no. 1, pp. 51–59, 2013.
- [49] L. T. Su, M. T. Yu, and Y. D. Song, "Effects of emitter discharge rate on soil salt dynamics in cotton field under drip irrigation with mulching condition in arid regions," *Arid Land Geography*, vol. 33, no. 6, pp. 889–895, 2010.
- [50] I. Bahçecı, R. Çakır, A. S. Nacar, and P. Bahçecı, "Estimating the effect of controlled drainage on soil salinity and irrigation efficiency in the Harran Plain using SaltMod," *Turkish Journal of Agriculture & Forestry*, vol. 32, no. 2, pp. 101–109, 2008.
- [51] A. El-Keblawy, S. Gairola, and A. Bhatt, "Maternal salinity environment affects salt tolerance during germination in *Anabasis setifera*: a facultative desert halophyte," *Journal of Arid Land*, vol. 8, no. 2, pp. 254–263, 2016.
- [52] X. Yang, A. Mamtimin, Q. He, X. Liu, and W. Huo, "Observation of saltation activity at Tazhong area in Taklimakan Desert, China," *Journal of Arid Land*, vol. 5, no. 1, pp. 32–41, 2013.
- [53] W. Z. Zeng, C. Xu, J. W. Wu, and J. S. Huang, "Soil salt leaching under different irrigation regimes: HYDRUS-1D modelling and analysis," *Journal of Arid Land*, vol. 6, no. 1, pp. 44–58, 2014.
- [54] L. J. Chen and Q. Feng, "Soil water and salt distribution under furrow irrigation of saline water with plastic mulch on ridge," *Journal of Arid Land*, vol. 5, no. 1, pp. 60–70, 2013.
- [55] X. Zhao, H. Xu, P. Zhang, and Y. Bai, "Distribution of soil moisture and salinity in shelterbelts and its relationship with groundwater level in extreme arid area, northwest of China," *Water and Environment Journal*, vol. 27, no. 4, pp. 453–461, 2013.
- [56] J. Abuduwaili, Y. Tang, M. Abulimiti, D. Liu, and L. Ma, "Spatial distribution of soil moisture, salinity and organic matter in Manas River watershed, Xinjiang, China," *Journal of Arid Land*, vol. 4, no. 4, pp. 441–449, 2012.
- [57] Y. Zhang, S. Liu, Z. Xiu, Q. Lu, H. Sun, and G. Liu, "TiO<sub>2</sub>/BiOI heterostructured nanofibers: electrospinning-solvothermal two-step synthesis and visible-light photocatalytic performance investigation," *Journal of Nanoparticle Research*, vol. 16, no. 5, article 2375, pp. 1–9, 2014.
- [58] L.-H. Xie and M. P. Suh, "High CO<sub>2</sub>-capture ability of a porous organic polymer bifunctionalized with carboxy and triazolo groups," *Chemistry*, vol. 19, no. 35, pp. 11590–11597, 2013.
- [59] H. Nakamoto and H. Tsutsumi, "Electrospun sulfur fibers as a template for micrometer-sized copper sulfide tubes," *Materials Letters*, vol. 136, no. 12, pp. 26–29, 2014.

- [60] L. Persano, A. Camposeo, and D. Pisignano, "Active polymer nanofibers for photonics, electronics, energy generation and micromechanics," *Progress in Polymer Science*, vol. 43, article 895, pp. 48–95, 2015.
- [61] C. Aprile, A. Corma, and H. Garcia, "Enhancement of the photocatalytic activity of TiO<sub>2</sub> through spatial structuring and particle size control: from subnanometric to submillimetric length scale," *Physical Chemistry Chemical Physics*, vol. 10, no. 6, pp. 769–783, 2008.
- [62] J. C. Hicks, J. H. Drese, D. J. Fauth, M. L. Gray, G. G. Qi, and C. W. Jones, "Designing adsorbents for CO<sub>2</sub> capture from flue gas-hyperbranched aminosilicas capable of capturing CO<sub>2</sub> reversibly," *Journal of the American Chemical Society*, vol. 130, no. 10, pp. 2902–2903, 2008.
- [63] X. L. Ma, X. X. Wang, and C. S. Song, "Molecular basket sorbents for separation of CO<sub>2</sub> and H<sub>2</sub>S from various gas streams," *Journal of the American Chemical Society*, vol. 131, no. 16, pp. 5777–5783, 2009.
- [64] W. J. Han, L. Ren, L. Gong et al., "Self-assembled three-dimensional graphene-based aerogel with embedded multifarious functional nanoparticles and its excellent photoelectrochemical activities," *ACS Sustainable Chemistry & Engineering*, vol. 2, no. 4, pp. 741–748, 2014.
- [65] Y.-E. Moon, G. Jung, J. Yun, and H.-I. Kim, "Poly(vinyl alcohol)/poly(acrylic acid)/TiO<sub>2</sub>/graphene oxide nanocomposite hydrogels for pH-sensitive photocatalytic degradation of organic pollutants," *Materials Science and Engineering B: Solid-State Materials for Advanced Technology*, vol. 178, no. 17, pp. 1097–1103, 2013.

## Research Article

# Attapulgite Nanofiber-Cellulose Nanocomposite with Core-Shell Structure for Dye Adsorption

**Xiaoyu Chen, Xiaoxue Song, and Yihe Sun**

*School of Material Engineering, Jinling Institute of Technology, Nanjing 211169, China*

Correspondence should be addressed to Xiaoyu Chen; [chxy@jit.edu.cn](mailto:chxy@jit.edu.cn)

Received 25 March 2016; Revised 22 May 2016; Accepted 31 May 2016

Academic Editor: Ming Zhang

Copyright © 2016 Xiaoyu Chen et al. This is an open access article distributed under the Creative Commons Attribution License, which permits unrestricted use, distribution, and reproduction in any medium, provided the original work is properly cited.

Nanocomposite particle used for adsorption has attracted continuous attention because of large specific surface area and adjustable properties from nanocomponent. Herein nanocomposite particle with cellulose core and attapulgite nanofibers shell was prepared. The size of cellulose core was about 2  $\mu\text{m}$  and the thickness of nanofibers shell is about 300  $\mu\text{m}$ . Adsorption capacity of nanocomposite particle to methylene blue can reach up to 11.07  $\text{mg L}^{-1}$  and the best adsorption effect occurs at pH = 8; pseudo-first-order equation and the Langmuir equation best describe the adsorption kinetic and isotherm, respectively; repeated adsorption-desorption experimental results show that 94.64% of the original adsorption capacity can be retained after being reused three times.

## 1. Introduction

Attapulgite nanofiber is a kind of hydrated octahedral layered magnesium aluminum silicate with diameter of 20 nm and length of several hundred nanometers to several micrometers [1, 2]. Theoretical formula of attapulgite nanofiber is  $(\text{Al}_2\text{Mg}_2)\text{Si}_8\text{O}_{20}(\text{OH})_2(\text{OH}_2)_4 \cdot 4\text{H}_2\text{O}$  [3]. Due to large specific surface area, attapulgite nanofiber has high sorption ability and is widely used in decoloring, drying, removing heavy metal ions or organic contaminants, and other fields [4, 5]. Attapulgite nanofiber possesses permanent negative charges and exchangeable cations [2]. Used as dye adsorbent, attapulgite nanofiber can remove cationic dye such as methylene blue from water. But when added to water, attapulgite nanofibers suspend in water and are difficult to be separated from water after adsorption. The suspended attapulgite will cause secondary pollution to the water and cannot be reused [6]. Therefore, finding an excellent carrier for attapulgite is important to avoid secondary pollution and to reuse attapulgite.

Polymer nanocomposites are composites of particle-filled polymers for which at least one dimension of the dispersed particles is in the nanometer range [7–9]. Polymer

nanocomposites containing attapulgite nanofiber have been prepared, in which polymer exists as hydrogel and attapulgite nanofibers are embedded in the hydrogel [10, 11]. This hydrogel can be used as super adsorbent and adsorbent for heavy metal ions [10, 11].

Adsorption usually occurred on the surface of adsorbent [12, 13]. Particle adsorbents have large surface area, which leads to high adsorption ability. Core-shell structure with adsorbent on the shell has low cost and is favorable for particle adsorbent to adsorb dye. Cellulose is one of the most abundant biopolymers in nature [14, 15]. Nanocomposite particle with cellulose core and attapulgite nanofiber shell has never been reported. But cellulose is difficult to dissolve in common solvent to form cellulose bead. NaOH/urea solution is a “green” and cheap method to dissolve cellulose with no pollution [16].

In this study, we combined attapulgite nanofiber and cellulose to prepare a low-cost adsorbent for water treatment. We prepared cellulose bead by dissolving cellulose in NaOH/urea solution as core to afford necessary strength. Attapulgite nanofibers were coated on cellulose bead as shell to adsorb dye. Coated attapulgite shell can prevent second pollution of attapulgite in water. The structure, adsorption

behaviors, and reusability of this nanocomposite were investigated.

## 2. Materials and Methods

**2.1. Materials.** NaOH, HCl, CaCl<sub>2</sub>, urea, acetic acid, methylene blue (methylthioninium chloride C<sub>16</sub>H<sub>18</sub>N<sub>3</sub>SCl), and other reagents used in the current work are all A.R. grade reagents. Attapulgit is provided by Jiangsu dianjinshi Au soil Mining Industry Co., Ltd. Distilled water is used in all experiments. Scoured cotton was used in this study as cellulose provided by Xuzhou weicai hygiene material factory Co., Ltd. Sodium alginate is provided by Shanghai Qingxi Chemical Technology Co., Ltd.

**2.2. Preparation of the Nanocomposite Particle.** Cellulose was dissolved in NaOH/urea solution using reported method [17]. Solution of NaOH (7 g), urea (12 g), and H<sub>2</sub>O (81 mL) was cooled to -12°C; then 2 g scoured cotton was immediately added to above solution; then scoured cotton was stirred vigorously for 2 min to obtain a transparent cellulose solution. The resulting solution was dropped into 20 wt% acetic acid solution to form cellulose bead; then the cellulose bead was immersed in water for three days to remove urea and NaOH in bead.

Attapulgit powder was dispersed in 2.5 wt% sodium alginate solutions with agitation and the mass ratios of sodium alginate/attapulgit are 1:0, 1:1, 0.83:1, and 0.5:1. Then cellulose bead was coated with above suspension and dipped in CaCl<sub>2</sub> solution to cross-link the sodium alginate. The coated bead was washed with deionized water and dried in an oven at 50°C for 48 h to get dried composite particle. Composite particles with alginate/attapulgit mass ratios of 1:0, 1:1, 0.83:1, and 0.5:1 were labeled as AC0, AC1, AC2, and AC3, respectively. In addition, attapulgit and cellulose solution mixture was dropped into 20 wt% acetic acid solution to form bead coded as AC4.

**2.3. Morphology and Structure of Composite Particle.** Surface morphology of composite bead was observed by scanning electron microscopy (SEM, SU8010, Hitachi). Microstructure of composite particles was observed by digital microscope (503+ Guangzhou Haote optical instrument company). Fourier-transform infrared (FTIR) spectra are recorded by Smart iTR accessory of FTIR spectrometer (Thermo Fisher Nicolet iS10). Wide-angle X-ray diffraction (XRD) measurement was carried out on an XRD diffractometer (D8-Advance, Bruker). The patterns with the Cu K $\alpha$  radiation at 40 kV and 30 mA were recorded in the region of 2 $\theta$  from 5° to 70°. TGA (STA 409 PC Luxx NETZSCH) was performed by heating samples to 700°C at 5°C/min under a nitrogen flow.

### 2.4. Adsorption Studies

**2.4.1. The Adsorption Ability Study.** 0.1 g adsorbent was immersed into 80 mL methylene blue solution of 12.016 mg L<sup>-1</sup>

at 25°C for 36 h with 120 r/min controlled by a full temperature incubator shaker. The adsorption capacity  $Q$  (mg g<sup>-1</sup>) was calculated using the following equation:

$$Q = \frac{(C_0 - C_e)V}{m}, \quad (1)$$

where  $C_0$  (mg L<sup>-1</sup>) is the initial dye concentrations of the solutions,  $C_e$  (mg L<sup>-1</sup>) is the equilibrium dye concentrations of the solutions,  $V$  (L) is the volume of the solution, and  $m$  (g) is the dried weight of the adsorbent [18]. Methylene blue concentration was measured at 664 nm using UV-Vis spectrophotometer (VARIAN Cary 50).

**2.4.2. pH Variation.** The initial pH of methylene blue solution (12.016 mg L<sup>-1</sup>) was adjusted by 0.1 mol L<sup>-1</sup> HCl or NaOH aqueous solutions to change between 2.06 and 9.93. 0.1 g AC2 was immersed into 80 mL of above solution for 36 h at 25°C. The adsorption capacity was calculated based on (1).

**2.4.3. Adsorption Kinetics.** The change of adsorption capacity with time was measured. 0.5 g adsorbents (AC1) were immersed into 200 mL methylene blue solution of 12.016 mg L<sup>-1</sup> at 25°C with continuous shaking at 120 r/min. At desired time intervals, 0.5 mL dyes solution was taken out to detect the current methylene blue concentration and 0.5 mL distilled water was added to the bulk solution to keep the volume constant. At time  $t_i$ , the adsorption capacity  $Q(t_i)$  (mg g<sup>-1</sup>) was calculated using the following equation [18]:

$$Q(t_i) = \frac{(C_0 - C_{t_i})V_0 - \sum_{i=1}^{i-1} C_{t_{i-1}}V_S}{m}, \quad (2)$$

where  $C_{t_i}$  (mg L<sup>-1</sup>) is the dye concentration at time  $t_i$ ;  $V_S$  is the volume of solution taken out each time for dye concentration analysis, and  $m$  (g) represents the mass of the adsorbent [18].

**2.4.4. Adsorption Equilibrium Study.** 0.1 g of AC2 was immersed into 80 mL methylene blue solution with concentration of 6.008 mg L<sup>-1</sup>, 9.012 mg L<sup>-1</sup>, 10.514 mg L<sup>-1</sup>, 12.016 mg L<sup>-1</sup>, and 15.02 mg L<sup>-1</sup>. Above five solutions were shook at 120 r/min at 25°C for 36 h. Then the adsorption capacity ( $Q_e$ ) of each solution was measured based on (1). The same procedure was conducted at 30°C, 35°C, 40°C, and 50°C. Then the curves of  $Q_e$ - $C_e$  were plotted.

**2.5. Reusability Property.** The methylene blue-loaded AC1 and AC2 were immersed into 0.1 mol L<sup>-1</sup> H<sub>2</sub>SO<sub>4</sub> aqueous solutions, washed with distilled water, and then reused in the next cycle of adsorption experiment. The adsorption-desorption experiments were conducted for four cycles. All experiments were performed at 25°C.

## 3. Results and Discussion

**3.1. Preparation of Composite Particles.** When used as adsorbent, attapulgit nanofiber usually suspends in solution,

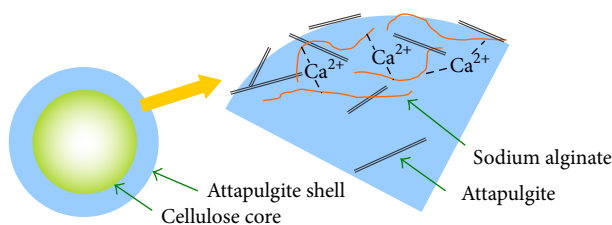


FIGURE 1: Schematic depiction of core-shell structure of cellulose-attapulgite composite particle.

which leads to second pollution to water and difficulty of regeneration. In this study, attapulgite is mixed with sodium alginate solution and is coated on the surface of cellulose bead. Sodium alginate, derived primarily from brown seaweed, is a linear polysaccharide copolymer that consists of two sterically different repeating units,  $\beta$ -D-mannuronic acid (M) and  $\alpha$ -L-guluronic acid (G), in varying proportions [19]. Sodium alginate can be cross-linked by  $\text{Ca}^{2+}$  to form hydrogel. Above mixture is cross-linked by  $\text{Ca}^{2+}$  to form a hydrogel layer above the cellulose bead. After drying, the hydrogel becomes an attapulgite shell on the surface of cellulose core, preventing the second pollution of attapulgite powder. The structure of nanocomposite particle is shown in Figure 1.

Cellulose is selected to prepare the core for its low cost and being nontoxic and biodegradable. But cellulose is difficult to dissolve in usual solvent. In this study, we use NaOH/urea solution in low temperature as solvent to dissolve cellulose and to prepare cellulose bead as the core.

**3.2. Morphology and Structure of Composite Particles.** Figure 2(a) shows microscope image of AC2 and particle has a diameter of about 2 mm and has a core-shell structure. Figures 2(b)–2(f) show the SEM image of cross section and surface of composite particle. Figure 2(b) shows that the shell is adhered closely to the cellulose core and no obvious boundary is found. Figure 2(c) shows the coarse shell with thickness of  $300\ \mu\text{m}$  (area between two white arrows). Figure 2(d) shows the aggregation area of attapulgite nanofibers (white arrow pointed). Aggregation areas of attapulgite indicate that the dispersion of attapulgite in shell is not well. The aggregation areas are enlarged in Figure 2(e), from which fibrous attapulgite is found. Figure 2(f) shows the pure sodium alginate area existing in the shell.

FTIR spectra of sodium alginate, attapulgite, and AC2 are shown in Figure 3. In the spectrum of AC2,  $1421\ \text{cm}^{-1}$  belongs to the symmetric stretch vibration of  $\text{C}=\text{O}$  of sodium alginate.  $3614\ \text{cm}^{-1}$  is attributed to the stretching modes of hydroxyls coordinated with the magnesium.  $3582\ \text{cm}^{-1}$  and  $3553\ \text{cm}^{-1}$  belong to the symmetric and antisymmetric stretching mode of molecular water coordinated with the magnesium at the edges of the channels [20].  $1027\ \text{cm}^{-1}$  belongs to Si-O-Si stretching vibration of attapulgite [21]. The results indicate that the shell is composed by sodium alginate and attapulgite. Smart iTR measures the surface structure of sample. So only the shell structure of composite particle can be detected.

Figure 4 shows the XRD peaks of attapulgite and attapulgite shell. Strong diffraction peak of  $8.48^\circ$  is a typical peak of attapulgite corresponding to basal spacing of about  $10.55\ \text{\AA}$  and is attributed to the primary diffraction of the (110) crystal face. Other diffraction peaks are attributed as d(110) ( $10.55\ \text{\AA}$ ), d(200) ( $6.43\ \text{\AA}$ ), d(130) ( $5.43\ \text{\AA}$ ), d(040) ( $4.48\ \text{\AA}$ ), d(121) ( $4.14\ \text{\AA}$ ), and d(061) ( $2.55\ \text{\AA}$ ) [22]. All belong to the character peaks of attapulgite. The diffraction peaks of  $26.54^\circ$  are attributed to intergrowth minerals of quartz in attapulgite. In attapulgite shell, no obvious shift of peak position indicates that the crystal structure of attapulgite has no change during mixing. Absence of diffraction peaks of sodium alginate revealed that sodium alginate exists as amorphous. XRD results confirmed that attapulgite is the main component of shell.

TG and DTG curves for the cellulose, attapulgite, and AC1 are presented in Figure 5. The weight loss rate of AC1 is between attapulgite and cellulose. For AC1, below  $100^\circ\text{C}$ , the weight loss was ascribed to the removal of water which included surface water and zeolitic water of attapulgite. Between  $200$  and  $300^\circ\text{C}$ , the rapid weight loss can be attributed to the decomposition of cellulose and sodium alginate. Above  $300^\circ\text{C}$ , the weight loss corresponds to the degradation of residual decomposition products and loss of coordinated water and structural hydroxyl water in attapulgite [23]. The high residue mass of AC1 compared to the cellulose indicates the existence of attapulgite.

**3.3. Adsorption Capacity.** Figure 6 shows the adsorption effect of AC1 (Figure 6(a), before adsorption; Figure 6(b), after adsorption). The slight color of Figure 6(b) reveals that the nanocomposite particles could effectively remove the methylene blue from water. The clear solution indicates that attapulgite nanocomposite prevents the second pollution of attapulgite nanofiber in water.

Figure 7 compares the adsorption capacities of nanocomposite particles (AC1, AC2, and AC3) with core-shell structure to contrast samples (cellulose bead, AC0, and AC4). Composite particles have better adsorption capacities compared to the adsorption capacities of cellulose bead, AC0, and AC4, which indicate that the shell of attapulgite nanofiber can effectively absorb methylene blue. The adsorption capacities of AC1, AC2, and AC3 are higher than AC0 which only has a shell of sodium alginate, indicating the adsorption mainly resulted from attapulgite nanofiber. AC3 has maximum adsorption capacity of  $9.1\ \text{mg}\cdot\text{g}^{-1}$ .

Attapulgite fiber is a kind of silicate with nanosized rod-like morphology and consists of two double chains of the pyroxene type  $(\text{SiO}_3)^{2-}$  like amphibole  $(\text{Si}_4\text{O}_{11})^{6-}$  running parallel to the fiber axis [24, 25]. Attapulgite fiber has high surface area and moderate cation exchange capacity, which is useful for attapulgite as adsorbents to remove dye in wastewater. In addition, attapulgite fiber has negatively charged sorption sites because of isomorphic substitutions in structure. So attapulgite nanofiber can absorb cationic dyes through electrostatic attraction. The higher adsorption capacity of AC3 resulted from the high content of attapulgite nanofiber. From Figure 8, we can see that AC1 has rare

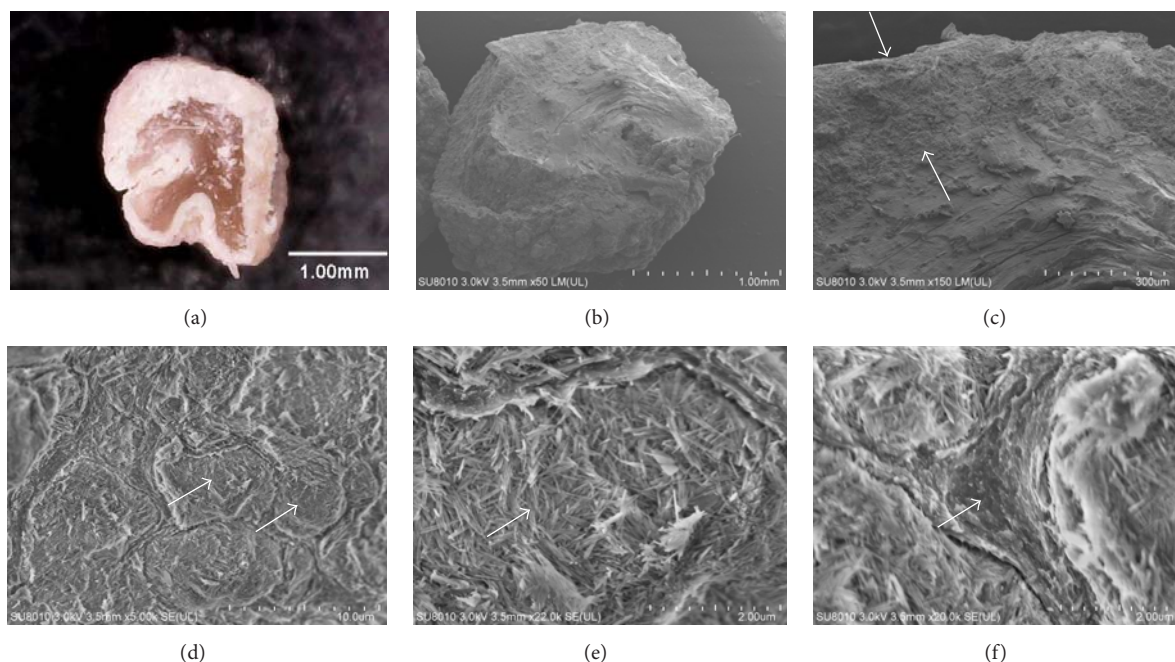


FIGURE 2: The morphology of the cellulose-attapulgite composite particles (AC2) ((a) cross section of particle by digital microscope; (b) cross section of particle by SEM; (c) shell structure of particle; (d) aggregation area of attapulgite; (e) amplified aggregation area of attapulgite; (f) area of sodium alginate).

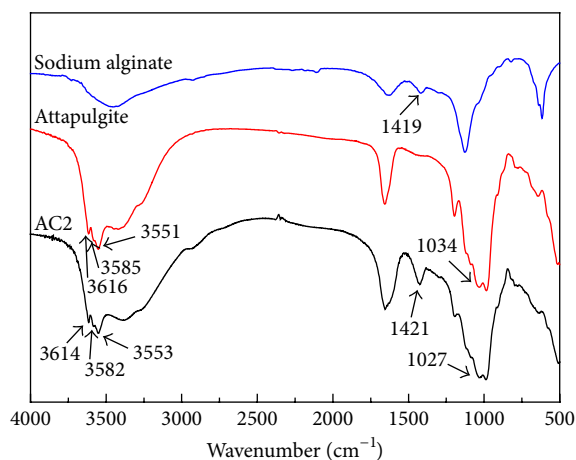


FIGURE 3: FTIR spectra of sodium alginate, attapulgite, and AC2.

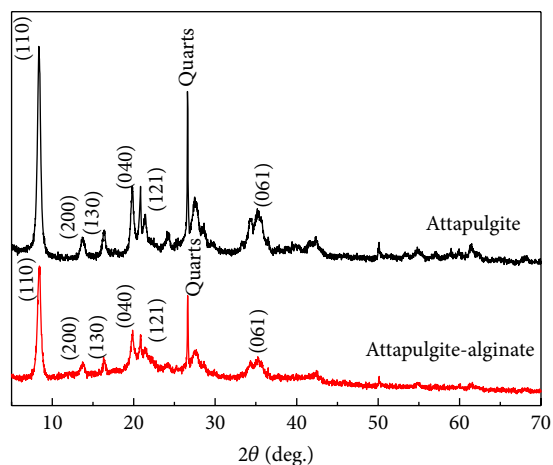


FIGURE 4: The powder X-ray diffraction pattern of the attapulgite and attapulgite shell.

dispersion of attapulgite nanofibers on the shell compared to AC2 and AC3, which leads to low adsorption capacity of AC1.

Other adsorption capacities for methylene blue have been reported, such as cross-linked porous starch ( $9.46 \text{ mg g}^{-1}$ ) [26], sugar extracted spent rice biomass ( $8.13 \text{ mg g}^{-1}$ ) [27], and attapulgite ( $51 \text{ mg g}^{-1}$ ) [28]. Compared to attapulgite, the relative lower capacity of nanocomposite particle may have resulted in the aggregation of attapulgite on the shell which was observed by SEM photo (Figure 2(d)). The aggregation decreased the specific surface area of attapulgite and then decreased adsorption ability [29].

**3.4. Effects of pH on the Adsorption.** Figure 9 shows the adsorption capacity of AC2 in the pH range of 2.06~9.93. As the pH increased from 2.06 to 7.97, adsorption capacity increased from  $7.70$  to  $8.88 \text{ mg g}^{-1}$ ; as the pH increased from 7.97 to 9.93, adsorption capacity decreased from  $8.88$  to  $8.43 \text{ mg g}^{-1}$ .

For attapulgite, some isomorphous substitutions in the tetrahedral layer, such as  $\text{Al}^{3+}$  for  $\text{Si}^{4+}$ , develop negatively charged sorption sites ( $\text{Si-O}^-$ ) on the surface of attapulgite [30].  $\text{Si-O}^-$  can absorb cation dye through electrostatic attraction [30]. But, at low pH, these negatively charged

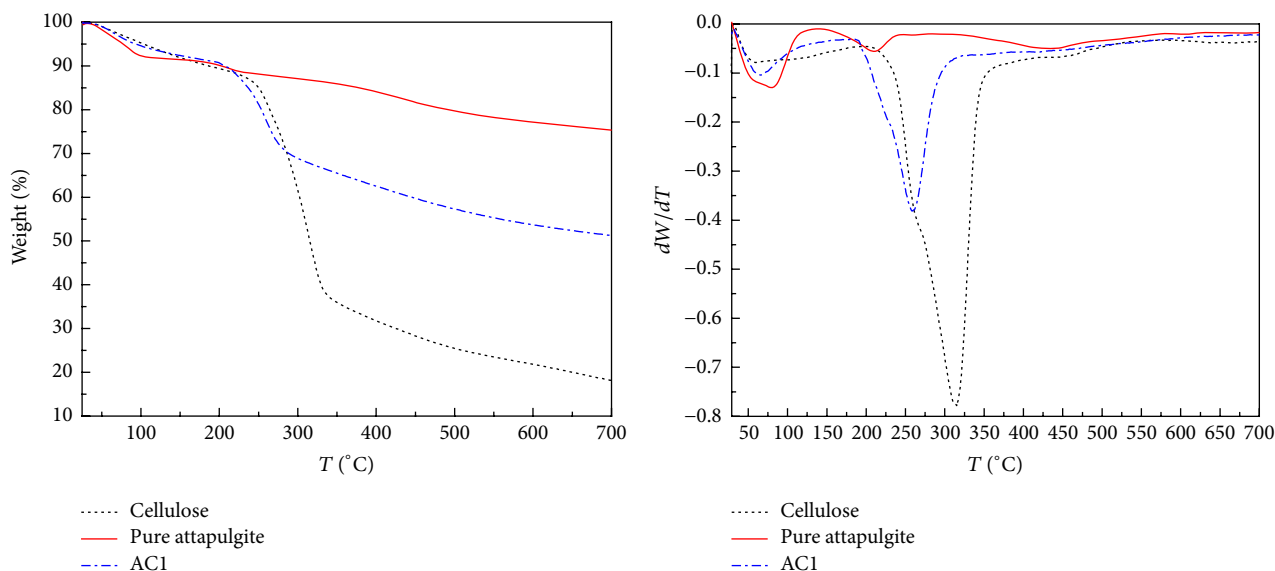


FIGURE 5: The TG and DTG of cellulose, attapulgite, and AC1.

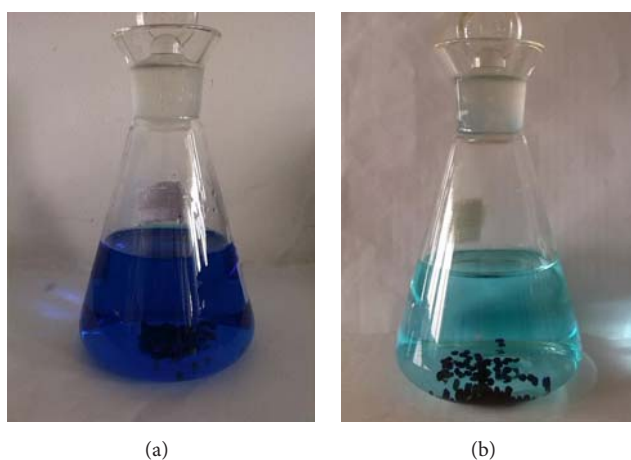


FIGURE 6: The methylene blue adsorption effect of 0.5 g AC1 in 200 mL  $12.016 \text{ mg L}^{-1}$  methylene blue solution for 48 h ((a) before adsorption and (b) after adsorption).

sorption sites are protonated to form  $\text{Si-OH}_2^+$  by  $\text{H}^+$ , which decrease the negative sites to attract methylene blue. As pH increases, protonated groups become less and negatively charged sites such as  $\text{Si-O}^-$  increase and favor the adsorption of cationic dye. In the alkaline pH range, the decreasing of adsorption capacity could be attributed to competition of  $\text{Na}^+$  ions for the negative adsorption sites [31].

**3.5. Adsorption Kinetics.** Time dependence of the adsorption capacity of AC1 for methylene blue was tested to study the adsorption kinetics. The initial concentration of methylene blue is  $12.016 \text{ mg L}^{-1}$ . The experimental results are shown in Figure 10. About 50% of methylene blue was adsorbed within 7 h. The adsorption equilibrium was achieved after 36 h. These results were similar to cross-linked porous starch

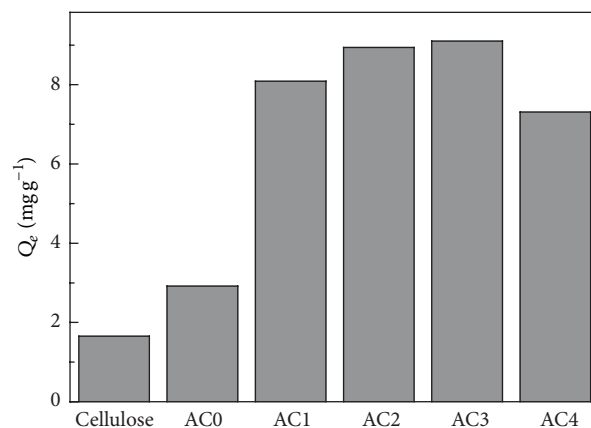


FIGURE 7: Adsorption capacity of six samples (cellulose bead, AC0, AC1, AC2, AC3, and AC4).

whose adsorption equilibrium was reached in about 30 h for methylene blue [26].

To further investigate the adsorption mechanisms, four common kinetic models were used to fit the data, namely, pseudo-first-order model [32], pseudo-second-order model [33], intraparticle diffusion models [34], and the Elovich equation [35]. Table 1 shows the equations of these models. In these models,  $k_1$  is the rate constant first-order absorption ( $\text{min}^{-1}$ ) [32];  $Q_{\text{eq}}$  ( $\text{mg g}^{-1}$ ) is the amount of dye adsorbed at equilibrium;  $Q_t$  ( $\text{mg g}^{-1}$ ) is the amount of dye adsorbed at any time  $t$  (min);  $k_2$  ( $\text{g mg}^{-1} \text{ min}^{-1}$ ) is the second-order rate constant [33];  $K_T$  ( $\text{mg g}^{-1} \cdot \text{min}^{1/2}$ ) is the diffusion rate constant [34];  $C$  is a constant related to the thickness of boundary layer [34];  $a$  ( $\text{mg g}^{-1} \text{ min}^{-1}$ ) is the initial sorption rate [35];  $b$  ( $\text{g mg}^{-1}$ ) is the desorption constant related to the extent of surface coverage and activation energy for chemisorption [35].

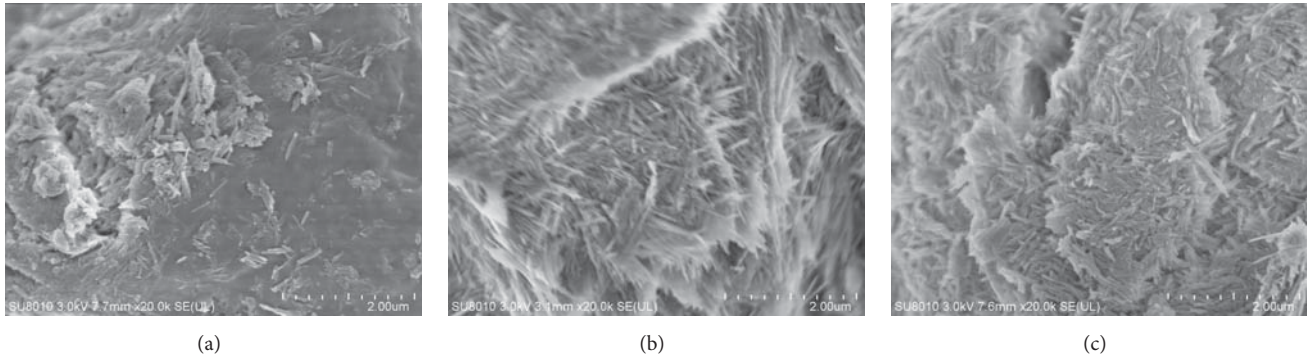


FIGURE 8: The surface morphology of the nanocomposite particles ((a) AC1; (b) AC2; (c) AC3).

TABLE 1: Kinetic models and their equations.

Kinetic model	Equation	Plot	Reference
Pseudo-first-order	$\log(Q_{\text{eq}} - Q_t) = \log Q_{\text{eq}} - k_1 t$	$\log(Q_{\text{eq}} - Q_t)$ versus $t$	[32]
Pseudo-second-order	$\frac{t}{Q_t} = \frac{1}{k_2 Q_{\text{eq}}^2} + \frac{1}{Q_{\text{eq}}} t$	$t/Q_t$ versus $t$	[33]
Intraparticle diffusion	$Q_t = K_T t^{1/2} + C$	$Q_t$ versus $t$	[34]
Elovich equation	$Q_t = \left(\frac{1}{b}\right) \ln(ab) + \frac{1}{b} \ln t$	$Q_t$ versus $\ln t$	[35]

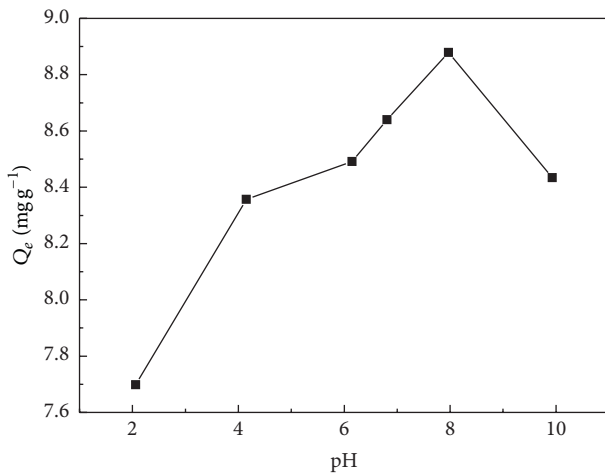


FIGURE 9: The influence of pH on the adsorption capacity of AC2 for methylene blue with concentration of  $12.016 \text{ mg L}^{-1}$  at  $25^\circ\text{C}$ .

The pseudo-second-order model assumes that the rate limiting step is chemical sorption [36]. Elovich model recently has been found to be valid to describe the sorption kinetics of ion exchange systems [18]. The fitted parameters of these kinetic models are listed in Table 2.  $R^2$  of the linear form for the various models suggests that the pseudo-first-order model is more suitable to describe the adsorption kinetic behavior. Using intraparticle diffusion model, plots of  $Q_t$  versus  $t^{1/2}$  do not pass through the origin indicating that the adsorption process is also controlled by film diffusion [36].

**3.6. Adsorption Equilibrium Study.** The equilibrium adsorption data is shown in Figure 11. At each temperature, adsorption capacity of AC2 for five different concentrations of

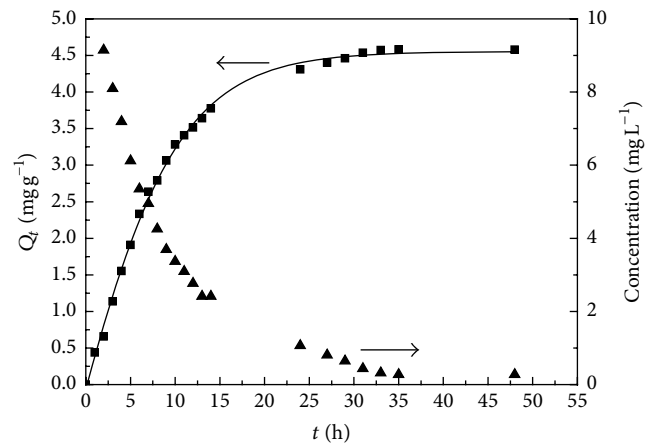


FIGURE 10: The adsorbed capacity of AC1 for methylene blue with concentration of  $12.016 \text{ mg L}^{-1}$  at  $25^\circ\text{C}$  and  $\text{pH} = 7.0$  as a function of time (■ represents experimental data; the full line represents fit of experimental data with a pseudo-first-order kinetic equation; ▲ represents concentration of methylene blue in solution).

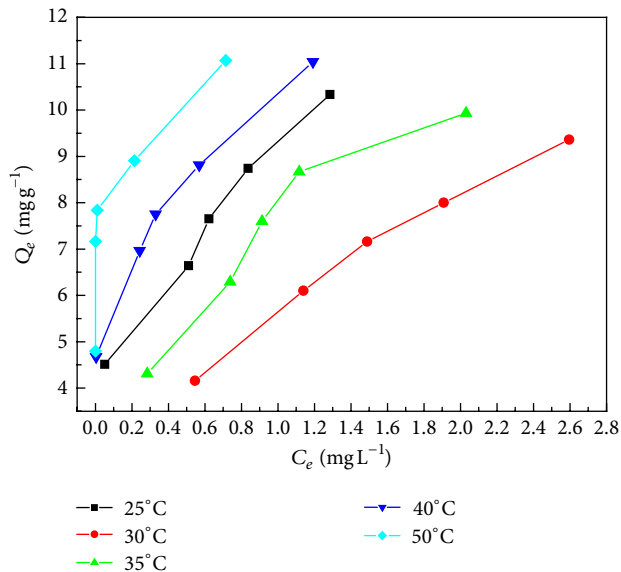
methylene blue was measured. The equilibrium adsorption data was correlated to four isotherm models: Langmuir [37], Freundlich [38], Sips [39], and Dubinin-Radushkevich [40]. Table 3 shows the equations of these models. In these models,  $Q_{\text{max}}$  is the maximum adsorption at monolayer coverage ( $\text{mg g}^{-1}$ ) [37];  $b$  is equilibrium constant ( $\text{mL mg}^{-1}$ ) in Langmuir adsorption [37] or Sips constant related to energy of adsorption in Sips model [39];  $K_F$  is the Freundlich characteristic constants [38];  $1/n$  is the Freundlich characteristic constants [38];  $n$  could be regarded as the Sips parameter characterizing the system heterogeneity;  $B$  is a constant

TABLE 2: The kinetic parameters for MB adsorption onto AC1.

T (°C)	Pseudo-first-order equation		Pseudo-second-order equation		Intraparticle diffusion models		Elovich equation		
	$k_1$ (min <sup>-1</sup> )	$R^2$	$k_2$ (g mg <sup>-1</sup> min <sup>-1</sup> )	$R^2$	$K_T$ (mg g <sup>-1</sup> min <sup>-1/2</sup> )	$R^2$	$a$ (mg g <sup>-1</sup> min <sup>-1</sup> )	$b$ (g mg <sup>-1</sup> )	$R^2$
25	0.11309	0.9952	0.01674	0.9779	0.7593	0.8746	1.3717	0.7705	0.9687

TABLE 3: Isotherm models and their equations.

Isotherm model	Equation	Plot	Reference
Langmuir	$\frac{1}{Q_{eq}} = \frac{1}{Q_{max}} + \frac{1}{Q_{max} b C_e}$	1/Q <sub>eq</sub> versus 1/C <sub>e</sub>	[37]
Freundlich	$\ln Q_{eq} = \frac{1}{n} \ln C_e + \ln K_F$	ln Q <sub>eq</sub> versus ln C <sub>e</sub>	[38]
Sips	$Q_{eq} = \frac{Q_m b C_e^{1/n}}{1 + b C_e^{1/n}}$	Q <sub>eq</sub> versus C <sub>e</sub>	[39]
Dubinin-Radushkevich	$\ln Q_{eq} = \ln Q_m - B \varepsilon^2$	ln Q <sub>eq</sub> versus $\varepsilon$	[40]

FIGURE 11: The curve of  $C_e$ - $Q_e$  of AC2 under different temperatures with duration time of 36 h.

related to the mean free energy of adsorption per mol of the adsorbate ( $\text{mol}^2 \text{J}^{-2}$ ) [40];  $Q_m$  is the theoretical saturation capacity ( $\text{mg g}^{-1}$ ) [40];  $\varepsilon$  is the Polanyi potential [40], which is equal to  $RT \ln(1 + 1/C_e)$ ;  $R$  ( $\text{J mol}^{-1} \text{K}^{-1}$ ) is the gas constant;  $T$  (K) is the absolute temperature.

The Langmuir isotherm model assumes the adsorption is monolayer adsorption [18]. A finite number of identical sites exist on a surface and all sites are energetically equivalent and there is no interaction between adsorbed molecules. Freundlich model is applied to describe that adsorption occurs on a heterogeneous surface. The fitting parameters of the above models are listed in Table 4. Most of the determination coefficients ( $R^2$ ) of the Langmuir model exceed 0.93 compared with those of the other models. This indicates that the Langmuir model is suitable to describe the adsorption

behavior of AC2. So it can be concluded that methylene blue molecule is absorbed on the surface with monolayer. From Figure 11, we can see that  $C_e$  is almost near zero at 25°C, 40°C, and 50°C, which indicates that the particle can remove dye in very dilute aqueous solutions.

**3.7. Regeneration Efficiency.** Reusability is very important for adsorbent in practical applications. In current work, the adsorption and desorption processes were repeated for three cycles to measure the regeneration efficiency. 0.1 mol L<sup>-1</sup> H<sub>2</sub>SO<sub>4</sub> aqueous solution was used to recover the methylene blue loaded composite particles. Table 5 shows the adsorption capacities and the regeneration efficiency in each cycle. After three cycles, AC2 gets 94.64% recovery, indicating a high regeneration efficiency. This also illuminates that the adsorbent is suitable for practical applications.

## 4. Conclusions

The attapulgite nanofibers were coated onto the surface of cellulose bead to form nanocomposite particles with core-shell structure. SEM, FTIR, XRD, and TG all revealed that attapulgite nanofiber exists in the shell of nanocomposite particles. Nanocomposite particles have higher adsorption capacity than cellulose bead. Adsorption capacity is changed with pH of dye solution and largest adsorption capacity occurs at pH = 8. The adsorption equilibrium and kinetics study of composite particles indicate that the adsorption behavior follows Langmuir model and pseudo-first-order equation. Dye-loaded nanocomposite could be regenerated easily and high adsorption ability is reserved. Simple preparation, low cost, being easy to regenerate make the core-shell structured nanocomposite a suitable carrier for attapulgite and an attractive adsorbent for removal of the organic dyes from water. This study also proposes a new approach to use the attapulgite and cellulose as adsorption material.

TABLE 4: The isotherms parameters for methylene blue adsorption onto AC2.

$T$ ( $^{\circ}\text{C}$ )	Langmuir model			Freundlich model			Dubinin-Radushkevich model			Sips model			
	$Q_{\max}$ ( $\text{mg g}^{-1}$ )	$b$ ( $\text{L mg}^{-1}$ )	$R^2$	$1/n$	$K_F$ ( $\text{mg g}^{-1}$ )	$R^2$	$Q_{\max}$ ( $\text{mg g}^{-1}$ )	$E$ ( $\text{kJ/mol}$ )	$R^2$	$Q_{\max}$ ( $\text{mg g}^{-1}$ )	$b$	$1/n$	$R^2$
25	11.2284	4.6800	0.9365	0.2410	8.8710	0.9282	8.7615	6.3976	0.8012	123.1803	0.0795	0.2963	0.9153
30	14.1965	0.7031	0.9875	0.5227	5.7221	0.9991	9.1354	2.0422	0.9360	51.6949	0.1252	0.5965	0.9992
35	13.1130	1.5313	0.9801	0.4446	7.6222	0.9677	9.6025	2.9773	0.9125	16.70934	0.8786	0.7696	0.9677
40	11.6023	8.7149	0.9721	0.1413	9.4353	0.9199	8.8507	12.1932	0.7702	151.0619	0.0699	0.1783	0.9006
50	11.3469	36.8745	0.9940	0.0741	10.7578	0.8544	10.2382	16.4501	0.7087	320.9413	0.0351	0.0818	0.8492

TABLE 5: Adsorption-desorption cycles of methylene blue.

Sample	Adsorption ability	First adsorption	Second adsorption	Third adsorption	Fourth adsorption
AC1	Adsorption capacity ( $\text{mg g}^{-1}$ )	8.6317	8.5228	7.9651	7.6254
	Recovery (%)	—	98.74	92.28	88.34
AC2	Adsorption capacity ( $\text{mg g}^{-1}$ )	8.7754	8.6317	8.5707	8.3050
	Recovery (%)	—	98.36	97.67	94.64

## Competing Interests

The authors declare that they have no competing interests.

## Acknowledgments

The authors would like to thank the Natural Science Foundation for Colleges and Universities of Jiangsu Province (Grant no. 12KJD150006) for the financial support of this research.

## References

- [1] Y. Liu, P. Liu, Z. Su, F. Li, and F. Wen, "Attapulgite- $\text{Fe}_3\text{O}_4$  magnetic nanoparticles via co-precipitation technique," *Applied Surface Science*, vol. 255, no. 5, pp. 2020–2025, 2008.
- [2] W. B. Wang and A. Q. Wang, "Nanocomposite of carboxymethyl cellulose and attapulgite as a novel pH-sensitive superabsorbent: synthesis, characterization and properties," *Carbohydrate Polymers*, vol. 82, no. 1, pp. 83–91, 2010.
- [3] B. Mu, Q. Wang, and A. Q. Wang, "Preparation of magnetic attapulgite nanocomposite for the adsorption of  $\text{Ag}^+$  and application for catalytic reduction of 4-nitrophenol," *Journal of Materials Chemistry A*, vol. 1, no. 24, pp. 7083–7090, 2013.
- [4] Y. Liu, W. B. Wang, Y. L. Jin, and A. Q. Wang, "Adsorption behavior of methylene blue from aqueous solution by the hydrogel composites based on attapulgite," *Separation Science and Technology*, vol. 46, no. 5, pp. 858–868, 2011.
- [5] L. Wang, J. P. Zhang, and A. Q. Wang, "Fast removal of methylene blue from aqueous solution by adsorption onto chitosan-g-poly (acrylic acid)/attapulgite composite," *Desalination*, vol. 266, no. 1–3, pp. 33–39, 2011.
- [6] Q.-H. Fan, P. Li, Y.-F. Chen, and W.-S. Wu, "Preparation and application of attapulgite/iron oxide magnetic composites for the removal of U(VI) from aqueous solution," *Journal of Hazardous Materials*, vol. 192, no. 3, pp. 1851–1859, 2011.
- [7] M. Alexandre and P. Dubois, "Polymer-layered silicate nanocomposites: preparation, properties and uses of a new class of materials," *Materials Science and Engineering R: Reports*, vol. 28, no. 1, pp. 1–63, 2000.
- [8] K. Kabiri, H. Omidian, M. J. Zohuriaan-Mehr, and S. Doroudiani, "Superabsorbent hydrogel composites and nanocomposites: a review," *Polymer Composites*, vol. 32, no. 2, pp. 277–289, 2011.
- [9] M. Shibayama, "Structure-mechanical property relationship of tough hydrogels," *Soft Matter*, vol. 8, no. 31, pp. 8030–8038, 2012.
- [10] H. X. Yang, W. B. Wang, and A. Q. Wang, "A pH-sensitive biopolymer-based superabsorbent nanocomposite from sodium alginate and attapulgite: synthesis, characterization, and swelling behaviors," *Journal of Dispersion Science and Technology*, vol. 33, no. 8, pp. 1154–1162, 2012.
- [11] P. Liu, L. P. Jiang, L. X. Zhu, and A. Q. Wang, "Attapulgite/poly(acrylic acid) nanocomposite (ATP/PAA) hydrogels with multifunctionalized attapulgite (org-ATP) nanorods as unique cross-linker: preparation optimization and selective adsorption of Pb(II) Ion," *ACS Sustainable Chemistry and Engineering*, vol. 2, no. 4, pp. 643–651, 2014.
- [12] M. Zhang, J. Soto-Rodríguez, I.-C. Chen, and M. Akbulut, "Adsorption and removal dynamics of polymeric micellar nanocarriers loaded with a therapeutic agent on silica surfaces," *Soft Matter*, vol. 9, no. 42, pp. 10155–10164, 2013.
- [13] I.-C. Chen, M. Zhang, B. Teipel, I. S. De Araujo, Y. Yegin, and M. Akbulut, "Transport of polymeric nanoparticulate drug delivery systems in the proximity of silica and sand," *Environmental Science and Technology*, vol. 49, no. 6, pp. 3575–3583, 2015.
- [14] S. Liu, D. Tao, T. Yu, H. Shu, R. Liu, and X. Liu, "Highly flexible, transparent cellulose composite films used in UV imprint lithography," *Cellulose*, vol. 20, no. 2, pp. 907–918, 2013.
- [15] M. Zhang and M. Akbulut, "Adsorption, desorption, and removal of polymeric nanomedicine on and from cellulose surfaces: effect of size," *Langmuir*, vol. 27, no. 20, pp. 12550–12559, 2011.
- [16] J. Zhou, C. Chang, R. Zhang, and L. Zhang, "Hydrogels prepared from unsubstituted cellulose in NaOH/urea aqueous solution," *Macromolecular Bioscience*, vol. 7, no. 6, pp. 804–809, 2007.
- [17] J. Cai, L. Zhang, J. Zhou et al., "Multifilament fibers based on dissolution of cellulose in NaOH/urea aqueous solution:

- structure and properties," *Advanced Materials*, vol. 19, no. 6, pp. 821–825, 2007.
- [18] W. X. Zhang, H. Yang, L. Dong et al., "Efficient removal of both cationic and anionic dyes from aqueous solutions using a novel amphoteric straw-based adsorbent," *Carbohydrate Polymers*, vol. 90, no. 2, pp. 887–893, 2012.
- [19] J. Han, Z. Zhou, R. Yin, D. Yang, and J. Nie, "Alginate-chitosan/hydroxyapatite polyelectrolyte complex porous scaffolds: preparation and characterization," *International Journal of Biological Macromolecules*, vol. 46, no. 2, pp. 199–205, 2010.
- [20] J.-H. Huang, Y.-F. Liu, Q.-Z. Jin, and X.-G. Wang, "Spectra study on the influence of drying process on palygorskite structure," *Spectroscopy and Spectral Analysis*, vol. 27, no. 2, pp. 408–410, 2007.
- [21] Z. Lei, Q. Yang, S. Wu, and X. Song, "Reinforcement of polyurethane/epoxy interpenetrating network nanocomposites with an organically modified palygorskite," *Journal of Applied Polymer Science*, vol. 111, no. 6, pp. 3150–3162, 2009.
- [22] C. Wang, Q. Wu, F. Liu et al., "Synthesis and characterization of soy polyol-based polyurethane nanocomposites reinforced with silylated palygorskite," *Applied Clay Science*, vol. 101, pp. 246–252, 2014.
- [23] W. Li, A. Adams, J. D. Wang, B. Blümich, and Y. G. Yang, "Polyethylene/palygorskite nanocomposites: preparation by in situ polymerization and their characterization," *Polymer*, vol. 51, no. 21, pp. 4686–4697, 2010.
- [24] Y. Zhang, W. Wang, J. Zhang, P. Liu, and A. Wang, "A comparative study about adsorption of natural palygorskite for methylene blue," *Chemical Engineering Journal*, vol. 262, pp. 390–398, 2015.
- [25] Y. Liu, W. Wang, and A. Wang, "Adsorption of lead ions from aqueous solution by using carboxymethyl cellulose-g-poly (acrylic acid)/attapulgite hydrogel composites," *Desalination*, vol. 259, no. 1–3, pp. 258–264, 2010.
- [26] L. Guo, G. Y. Li, J. S. Liu, Y. F. Meng, and Y. F. Tang, "Adsorptive decolorization of methylene blue by crosslinked porous starch," *Carbohydrate Polymers*, vol. 93, no. 2, pp. 374–379, 2013.
- [27] M. S. U. Rehman, I. Kim, and J.-I. Han, "Adsorption of methylene blue dye from aqueous solution by sugar extracted spent rice biomass," *Carbohydrate Polymers*, vol. 90, no. 3, pp. 1314–1322, 2012.
- [28] A. Al-Futaisi, A. Jamrah, A. Al-Rawas, and S. Al-Hanai, "Adsorption capacity and mineralogical and physico-chemical characteristics of Shuwaymiyah palygorskite (Oman)," *Environmental Geology*, vol. 51, no. 8, pp. 1317–1327, 2007.
- [29] G. Y. Tian, Y. R. Kang, B. Mu, and A. Q. Wang, "Attapulgite modified with silane coupling agent for phosphorus adsorption and deep bleaching of refined palm oil," *Adsorption Science & Technology*, vol. 32, no. 1, pp. 37–48, 2014.
- [30] H. Chen and J. Zhao, "Adsorption study for removal of Congo red anionic dye using organo-attapulgite," *Adsorption*, vol. 15, no. 4, pp. 381–389, 2009.
- [31] M. T. Yagub, T. K. Sen, and M. Ang, "Removal of cationic dye methylene blue (MB) from aqueous solution by ground raw and base modified pine cone powder," *Environmental Earth Sciences*, vol. 71, no. 4, pp. 1507–1519, 2014.
- [32] S. Lagergren, "About the theory of so-called adsorption of soluble substances," *Kungliga Svenska Vetenskapsakademiens Handlingar*, vol. 24, pp. 1–39, 1898.
- [33] Y. S. Ho and G. McKay, "Sorption of dye from aqueous solution by peat," *Chemical Engineering Journal*, vol. 70, no. 2, pp. 115–124, 1998.
- [34] Y. A. Yahaya, M. Mat Don, and S. Bhatia, "Biosorption of copper (II) onto immobilized cells of *Pycnoporus sanguineus* from aqueous solution: equilibrium and kinetic studies," *Journal of Hazardous Materials*, vol. 161, no. 1, pp. 189–195, 2009.
- [35] M. J. D. Low, "Kinetics of chemisorption of gases on solids," *Chemical Reviews*, vol. 60, no. 3, pp. 267–312, 1960.
- [36] C. Duran, D. Ozdes, A. Gundogdu, and H. B. Senturk, "Kinetics and isotherm analysis of basic dyes adsorption onto almond shell (*Prunus dulcis*) as a low cost adsorbent," *Journal of Chemical & Engineering Data*, vol. 56, no. 5, pp. 2136–2147, 2011.
- [37] I. Langmuir, "The adsorption of gases on plane surfaces of glass, mica and platinum," *The Journal of the American Chemical Society*, vol. 40, no. 9, pp. 1361–1403, 1918.
- [38] H. M. F. Freundlich, "Über die adsorption in lösungen," *Zeitschrift für Physikalische Chemie*, vol. 57, pp. 385–470, 1906.
- [39] R. Sips, "On the structure of a catalyst surface," *The Journal of Chemical Physics*, vol. 16, no. 5, pp. 490–495, 1948.
- [40] M. M. Dubinin, "Sorption and structure of active carbons: I. Adsorption of organic vapors," *Zhurnal Fizicheskoi Khimii*, vol. 21, pp. 1351–1362, 1947.